



Contents lists available at ScienceDirect

Materials Science & Engineering R

journal homepage: www.elsevier.com/locate/mser

Porous ceramics: Light in weight but heavy in energy and environment technologies

Yu Chen^{a,b}, Nannan Wang^{a,*}, Oluwafunmilola Ola^{b,1}, Yongde Xia^b, Yanqiu Zhu^{b,*}

^a GIFT (Guangxi Institute for Fullerene Technology), Key Laboratory of New Processing Technology for Nonferrous Metals and Materials, Ministry of Education, School of Resources, Environment and Materials, Guangxi University, Guangxi, 530004, China

^b College of Engineering, Mathematics and Physical Sciences, University of Exeter, Exeter, EX4 4SB, United Kingdom

ARTICLE INFO

Keywords:

Porous ceramics
Lightweight
Energy
Environment

ABSTRACT

Benefitting from the combined properties of intrinsic ceramic materials and advanced porous configuration, lightweight porous ceramics with porosity ranging from 2.3 to 99% and pore size distribution within 3 nm - 3 μm exhibit low density, large specific surface area, high toughness, strong thermal shock resistance, good thermal insulation capability, excellent high temperature stability, and low dielectric constant, which are barely offered by metal, polymer or even their dense counterpart. This unique set of features endow porous ceramics an indispensable role in the future development of sustainable energy and environmental applications. To be successfully applied in these applications, precise selection of the type of ceramics and creation of their detailed structural features of the pores are the most important stages that require intensive investigations and comprehensive understanding. For a given ceramic, the synthesis process is critical for achieving the desired pore configuration and geometry which eventually determines the final properties of the products, including both the usual mechanical properties and other advanced functionalities. In this review, we will first focus on the fabrication processes that determine the pore structures and geometries. Four mainstream fabrication methods: partial sintering, replica template, sacrificial template, and direct foaming will be discussed, in addition to the additive manufacturing technique which has emerged as a promising process for the direct fabrication of porous ceramics components. Each approach demonstrates its unique suitability for a specific range of materials, porosity, pore size, pore connectivity, and pore distribution. The principles and challenges of each synthesis strategies will be summarised and discussed, the progress that can be made to meet the requirement of advanced applications has been clarified. We then focus on the properties derived from different pore features. The superior damage tolerance and thermal insulation capability of porous ceramics, as compared with their dense counterpart, are presented. Thirdly, the great potentials of these interesting porous ceramics for the energy- and environmental-based applications, including filters, catalyst support, energy storage and conversion components, energy harvesting devices, and insulators are highlighted, in association with the criteria and demands for manufacturing processes. It is envisaged that this review will provide a guidance in the manufacture of advanced porous ceramics with desired pore structures and properties tailored for specific applications. Finally, we will demonstrate how these porous ceramics could contribute to the development of current and future energy and environment technologies.

1. Introduction

Ceramic materials exhibit high hardness and strength, excellent oxidation and corrosion resistance, low thermal expansion, and good stability and operational potential at high temperatures. These highly desired features enable them to outperform metal or polymer-based

materials in many applications, particularly under harsh working conditions such as at high temperature or in corrosive environments. However, the intrinsic brittleness of ceramics limits their mechanical damage tolerance and imposes a huge barrier for their wide engineering applications. To overcome this issue, pores are incorporated into the structure, as one solution. Surprisingly, their functionalities are

* Corresponding authors.

E-mail addresses: wangnannan@gxu.edu.cn (N. Wang), Y.Zhu@exeter.ac.uk (Y. Zhu).

¹ New address: Advanced Materials Group, Faculty of Engineering, The University of Nottingham, Nottingham, NG7 2RD, United Kingdom.

<https://doi.org/10.1016/j.mser.2020.100589>

Received 21 August 2020; Received in revised form 19 September 2020; Accepted 7 October 2020

Available online 28 November 2020

0927-796X/© 2020 The Author(s). Published by Elsevier B.V. This is an open access article under the CC BY license (<http://creativecommons.org/licenses/by/4.0/>).

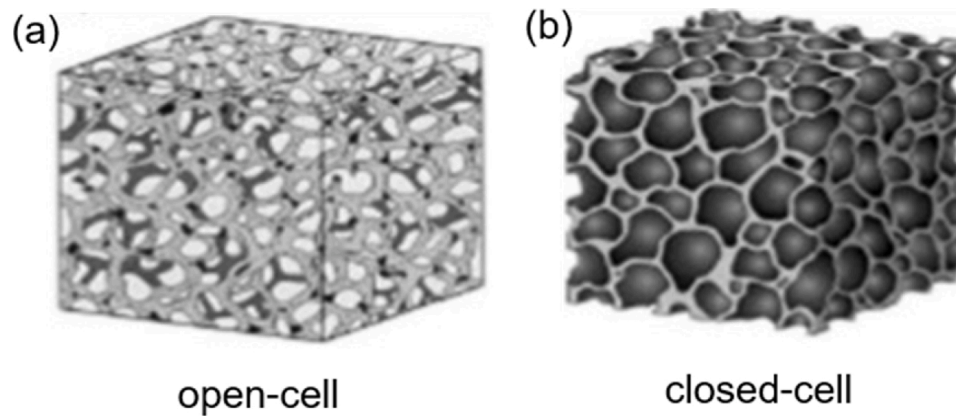


Fig. 1. Images of (a) open-cell, and (b) closed-cell foam. Open pores have solid edges and open faces, and fluid flow is possible to penetrate among them; whilst closed pores are connected via solid faces with no interconnectivity among them. Reproduced with permission [8]. Copyright 2016, IEEE.

significantly extended by doing so, since porous ceramics provide a unique set of properties. Some features such as low density, large specific surface area, high toughness, strong thermal shock resistance, good thermal insulation capability, and low dielectric constant, which are hardly offered by their dense counterparts, open a whole new gate to a diverse range of applications from abundant industrial processes to household products.

Specifically, increased research interests have emerged in the development of advanced porous ceramics, owing to their indispensable potentials as components in the ever-important energy- and environment-related fields. Example subject areas of interest include:

(1) Porous ceramics as efficient filtration components for collecting unwanted particulate matters in hot gas from industrial processes and diesel engines exhaust; (2) Porous ceramic-based filters for purification of drinking water by removing heavy metals, virus and contaminants; (3) Porous ceramics as a catalyst support for pollutants degradation, environmental remediation, phenol mineralisation, and hydrogen production; (4) Porous ceramics as energy storage components in concentrated solar power configurations and batteries; (5) Pores incorporated into ferroelectric ceramics for the development of advanced micro-mechanical systems (MEMS), which can be exploited to power small-scale electronic devices by scavenging energy from surrounding environment to ease off the shortcomings of batteries such as finite lifetime and high maintenance cost; (6) Their efficient electromagnetic interference (EMI) shielding effect offering great potentials for commercial wireless communication devices, automobile applications and modern aircrafts; (7) Benefiting from the porous configurations, the heat insulation and sound absorption capability of porous ceramics making them ideal construction materials.

These are very important subject areas directly related to different aspects of issues concerning energy and environments, therefore the development of porous ceramics for current and future technology applications is immensely essential. To exploit the full potentials of this special class of materials, a comprehensive and in-depth understanding of the key features of different porous ceramics is a necessary step, prior to materials selection, component design and performance realisation. Existing researches have mainly focused on answering one specific question or demonstrating one or two advantages of a porous ceramic. A few review papers had timely and neatly summarised the research progresses achieved over last decades, which had virtually illustrated the importance of this class of high performance and lightweight materials. These periodic summaries were primarily focused on the processing and properties of porous ceramics [1–3], and on the broad areas of applications, such as those by Galassi [4], and Hammel et al [5]. However, after another decade's developments, the relationship amongst the new fabrication approaches, the resulting properties, high level controlling of the pore configurations and the specific engineering

requirements in practical applications demands a critical update, which becomes the driving force of this review.

In this context, we intend to summarise the most recent developments in the synthesis method and a wide range of properties of porous ceramics, and systematically discuss the important features of each strategy in terms of their microstructural features and pore characteristics, as well as their implications in performance. Special emphasis will be placed on properties associated with applications in energy- and environment-related areas, such as in filters, catalyst support, energy conversion and storage media, energy harvesting systems, and advanced insulations.

1.1. The definition and classification of porous ceramics

Porous ceramics are traditionally classified into three main categories according to the pore size: macro-porosity ($d > 50$ nm), meso-porosity ($2 \text{ nm} < d < 50$ nm), and micro-porosity ($d < 2$ nm) [1]. A commonly used hierarchical pore structure, however, refers to the co-existence of a combination of differently sized pores in a single monolithic matrix. Porous ceramics are also categorised by their basic pore structure as open-cell (or reticulated) and closed-cell (Fig. 1a,b), and this feature plays a decisive role in determining the functionalities of various materials [6]. Owing to its gas and liquid permeability, the open-cell structure with connected pores is favourable for applications where the fluid transport is demanded. In contrast, pores isolated in a continuous ceramic matrix in the closed-cell structure, offer potential advantages for applications as insulation materials, since the fluid flow is required to be restricted [4,7]. Therefore, for a specific application, the proper selection of the right ceramic matrix with desired pore size and open or closed pore configuration is of great importance. These fundamental structural features effectively define the final mechanical properties and advanced functionalities of the porous ceramics.

1.2. Relationship among synthesis, properties, and suitability for energy- and environment-related applications

As the advantages of porous ceramics originate from the dedicated features of the pore, hence the creation and control of the desired pore features is the foremost aspect, prior to evaluating the property and utilising them in applications. In fact, numerous functionalities can be created without sacrificing the basic mechanical performance of the parent materials by carefully controlling the pore characteristics. To realise this, immense efforts have been dedicated to the synthesis processes, and various fabrication techniques have been developed. To date, four mainstream approaches are widely investigated:

(1) Partial sintering: the simplest method for the fabrication of porous ceramics, using lower temperature and shorter calcination time

than those required for obtaining their dense counterparts.

(2) Replica template: impregnating a porous polymeric sponge or a natural porous structure with a ceramic (pre-ceramic) suspension.

(3) Sacrificial template: mixing appropriate amount of sacrificial template as pore forming agents.

(4) Direct foaming: incorporating a gaseous phase into a ceramic suspension by either mechanical frothing, injection of a gas stream, or gas-releasing chemical reactions.

The latter three approaches are also followed with a setting/drying treatment for steadiness of the mixture and a calcination process where the removal of templates occurs.

Additionally, additive manufacturing (AM) as an emerging technology has demonstrated great potential for the preparation of porous ceramics, therefore the pore characteristics of this technique are also summarised in this review, as a promising alternative to conventional manufacturing procedures for the development of energy- and environmental-related applications, despite that the AM products so far are limited mainly in biomedical field.

As shown in Fig. 2, each fabrication method is best suited for producing a specific range of overall porosity and pore morphology, combined with pore size distribution and pore connectivity (commonly identified as open and closed porosity) [9]. Compared with their intrinsic properties, porosity and microstructure control are more essential for tailoring the properties of the resultant porous ceramics. These rich pore characteristics could lead to tremendously varying properties and applications.

Following the composition-structure-property loop in general materials research and adjusted specifically for the key pore features, we therefore will arrange the content of this review according to the synthesis strategies towards first the pore sizes then the pore configurations. Building on top of the various pore characteristics of specific ceramics, we will further discuss their abundant properties, and finally we attempt to establish links between these properties and applications, with special interests relating to the areas of energy and environment. A content flow of this review is illustrated in Fig. 3, for easy access.

2. Fabrication strategies

2.1. Partial sintering

As the most conventional and frequently employed approach for the fabrication of porous ceramics, partial sintering uses lower temperatures and shorter processing time on the powder compact—green body, than those required for obtaining their corresponding dense materials. The microstructure of porous ceramics is mainly controlled by the size and amount of the starting powders and the sintering conditions. The porosity and pore size of materials are strongly dependent on the green body densities and the use of additives. Sintering conditions (e.g. temperature, atmosphere, pressure, etc.) are of great importance since porosity decreases with increased forming pressure, sintering temperature, and time. Generally, the relatively low porosity (< 50 %), homogeneous macro-pores with diameter over 50 nm, and the bridging of particles promoted by the formation of thick and strong necks of the resultant porous ceramics lead to substantially higher strength compared with other conventional approaches [1]. Meanwhile, the extreme narrow size distribution, interconnected open porosity, and the easiness of dimensional control of the resulting structures are considered as the exceptional merit of this technique.

These microstructural features also endow porous ceramics the low effective thermal conductivity, since un-sintered powder compacts with point contacts are percolative and disrupted to some extent. As a result, the conductivity decreases very rapidly, but can be tailored in an equally wide range. Therefore, partial sintering is considered as a powerful technique for managing thermal properties of the final products [14]. To meet the ever-increasing demands, advanced sintering techniques such as partial hot-press or spark plasma sintering (SPS) have been developed to enhance the grain bonding for improved mechanical strengths. As shown in Table 1, porous ceramics fabricated by different techniques, together with their resulting microstructures are summarised. Detailed introduction of techniques that can be used for partial sintering will be presented in 2.1.2. Additionally, improved porosity can be obtained when it is combined with in-situ chemical reaction, which makes the

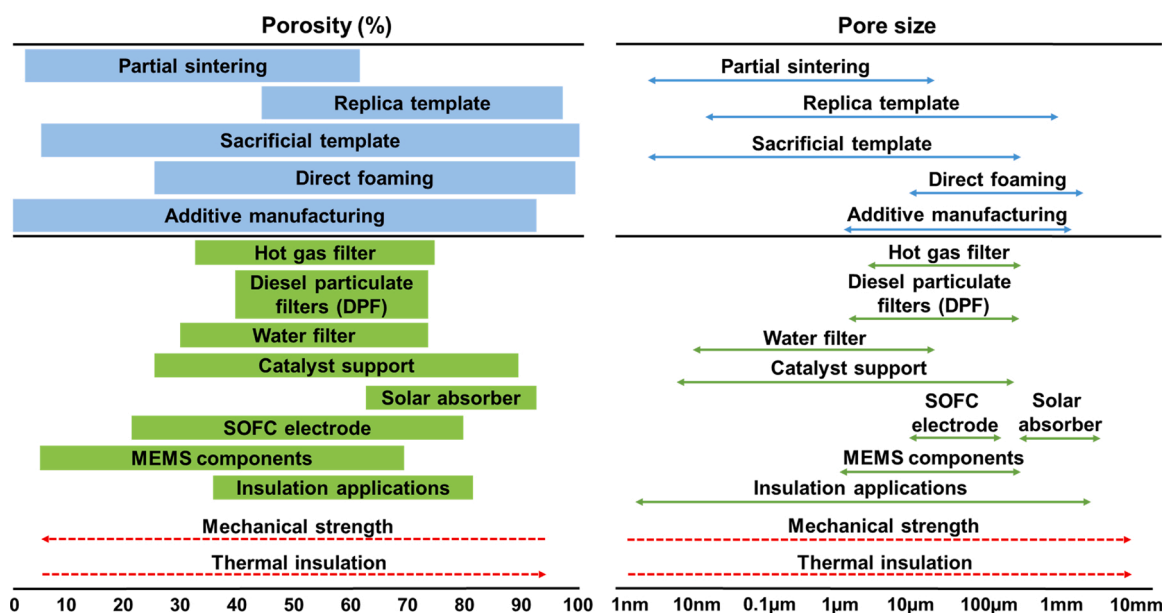


Fig. 2. The porosity and pore size distribution features of porous ceramics that can be created by techniques such as partial sintering, replica template, sacrificial template, and direct foaming.

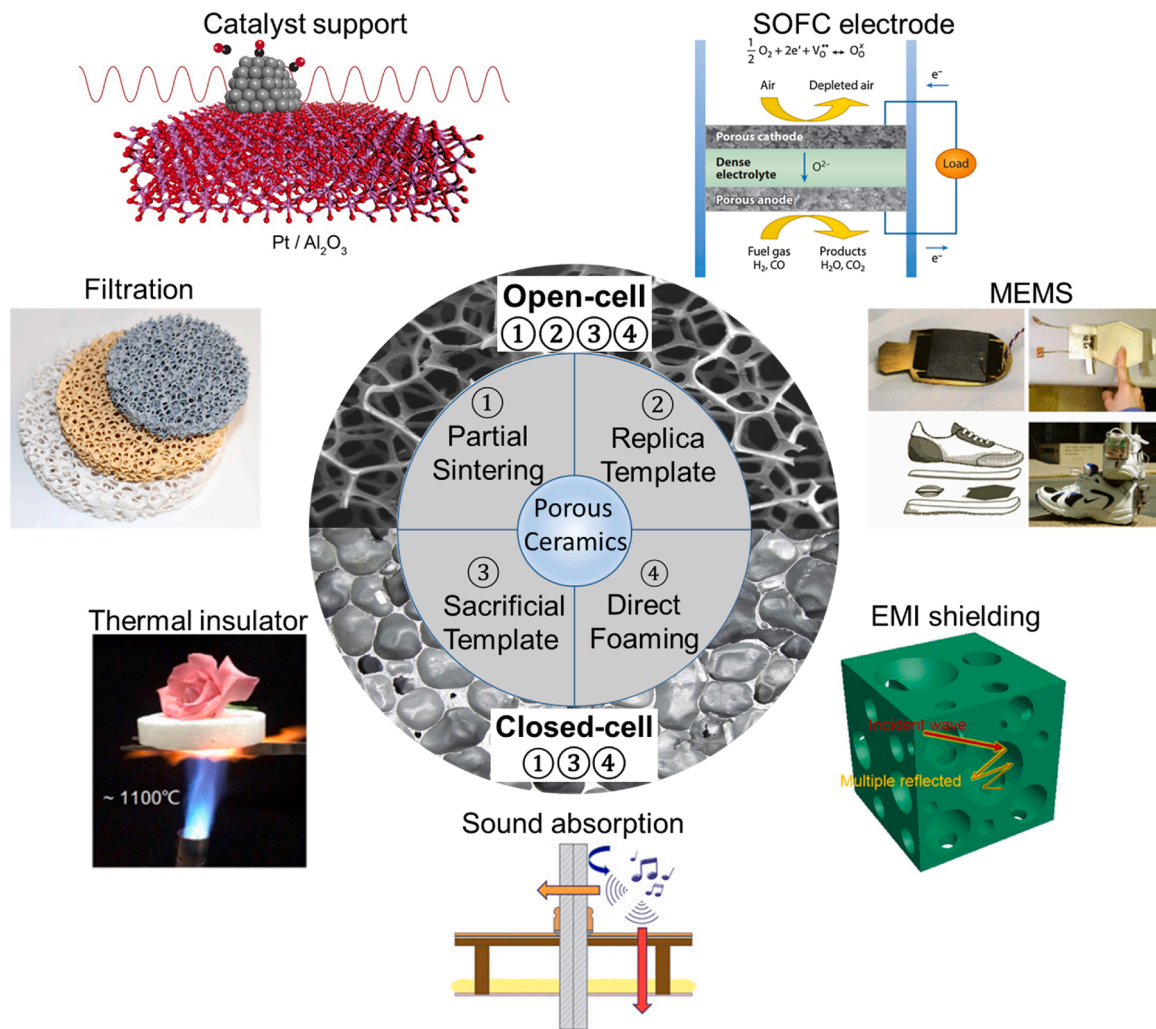


Fig. 3. The content of this review: the four fabrication strategies and their underlining applications in a wide range of energy- and environment-related areas. Image of the thermal insulator is reproduced with permission [10]. Copyright 2019, American Chemical Society. Image of the SOFC is reproduced with permission [11]. Copyright 2019, John Wiley & Sons. Image of the MEMS is reproduced with permission [12]. Copyright 2011, IntechOpen. Image of the EMI shielding is reproduced with permission [13]. Copyright 2017, American Chemical Society. Other images come from open sources from the internet.

Table 1

A summary of the microstructural features and potential applications of porous ceramics fabricated via different partial sintering.

Materials	Sintering method	Porosity (%)	Pore size (μm)	Target applications	Refs
Al ₂ O ₃	Pressureless sintering	20–40	–	–	[15]
Si ₃ N ₄	Pressureless sintering	2.3–35.9	2–5	–	[16]
β-Si ₃ N ₄	Pressureless sintering	54.1	–	High temperature applications	[17]
SiC	Pressureless sintering	34–42	0.03–0.7	–	[18]
SiO ₂ glass	Pressureless sintering	25 (average)	5.4 (average)	Filtration needs	[19]
YB ₄	Pressureless sintering	60–70	0.01–0.15/ 7–11 (bimodal)	Energy absorption	[20]
YbB ₆	Pressureless sintering	58.7–72.5	1.8–25.5	UHT applications	[21]
ZrO ₂	Pressureless sintering	18.3–46	0.025–0.060	Thermal insulator	[22]
ZrO ₂	Pressureless sintering	11.8–47.4	–	–	[23]
Si ₃ N ₄	Partial hot-press (isotropic)	16–54	–	–	[24]
	Partial hot-press (anisotropic)	0–40	–	–	
ZrB ₂ -SiC	Partial hot-press	12–29	1.7–1.9	–	[25]
ZrB ₂ -SiC	Partial hot-press	8.7–27.3	2.21–4.23	–	[26]
Diatomite	SPS	40–52	0.75–1.2	Water and beverage purification and waste-water treatment	[27]
Al ₂ O ₃ /Al ₂ TiO ₅	SPS	28.3	1–35	–	[28]
Al ₂ O ₃	SPS	52–58	–	Bioreactor, bone substitutes	[29]
Al ₂ O ₃	SPS	20–63	0.003–1	Micro/nano particle filters/structural components	[30]
Mg ₂ Si _{0.5} Sn _{0.5}	SPS	37	–	–	[31]
SiC	SPS	32–42	–	–	[32]
ZrB ₂	SPS	21–38	3 (average)	Ultrahigh temperature structural applications	[33]

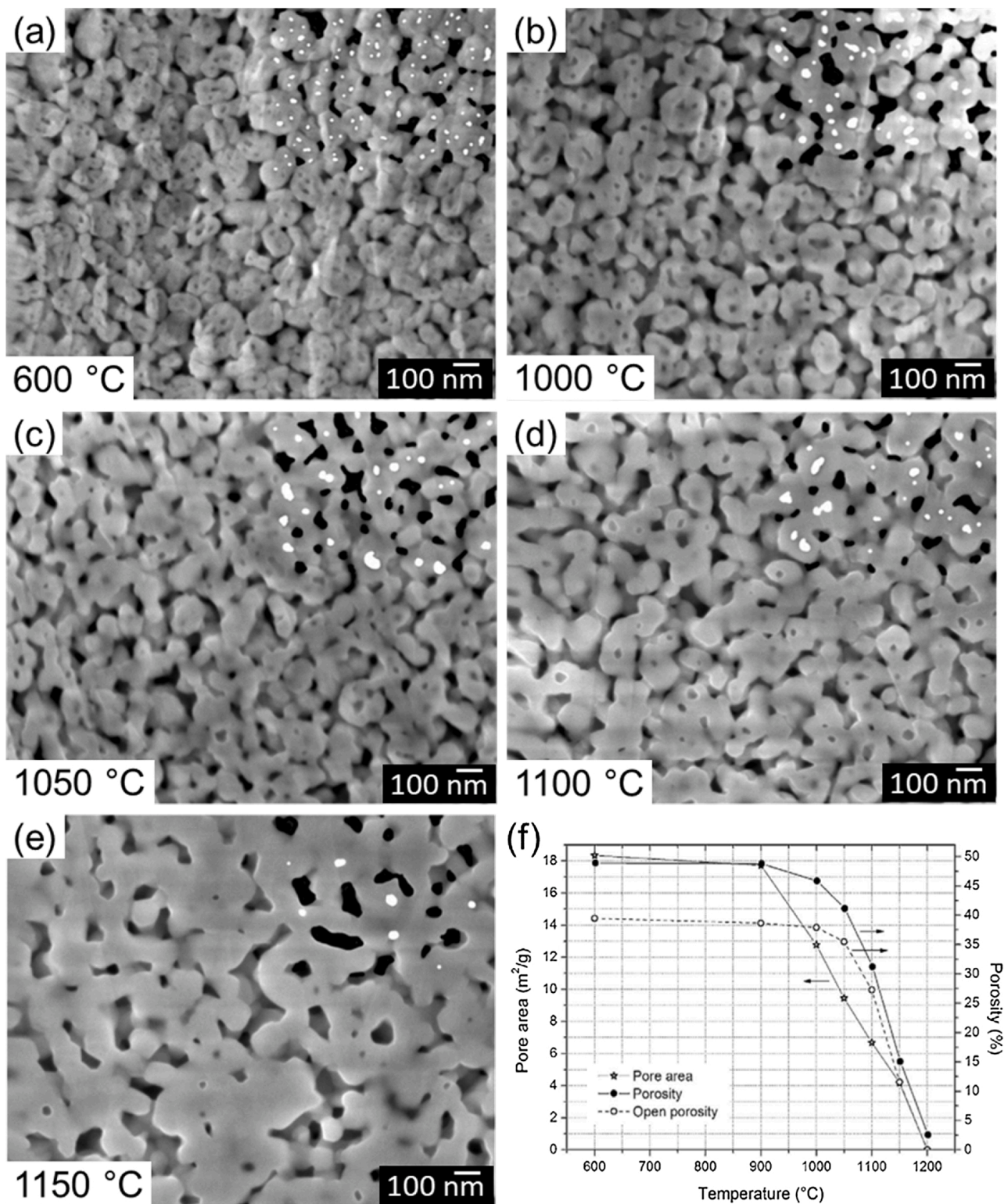


Fig. 4. SEM images of porous tetragonal zirconia (TZ) nanoceramics partially sintered for 2 h at: (a) 600 °C, (b) 1000 °C, (c) 1050 °C, (d) 1100 °C, and (e) 1150 °C. The intra-particle pores were coloured in white. Reproduced with permission. (f) Pore area and porosity as a function of sintering temperature for the yttria-stabilised tetragonal zirconia (Y-TZP) nanoceramics. Reproduced with permission [22]. Copyright 2013, Elsevier B.V.

products more desirable for filtration applications.

2.1.1. Microstructural evolution

In partial sintering, particles of powder compact are bonded by surface diffusion, evaporation-condensation, recrystallisation or solution-precipitation process, and a full densification would be retarded or

prohibited by the reduction of the sintering potential or sintering temperature, so that porous structures are created by a constrained network of coarse powders [1,7]. This sometimes leads to a hierarchical porous structure containing up to three levels of interconnected pores: (i) voids between agglomerates ($\geq 10 \mu\text{m}$); (ii) pores within the agglomerates ($\sim 100\text{--}1000 \text{ nm}$); and (iii) pores within the particles ($< 100 \text{ nm}$) [29]. The

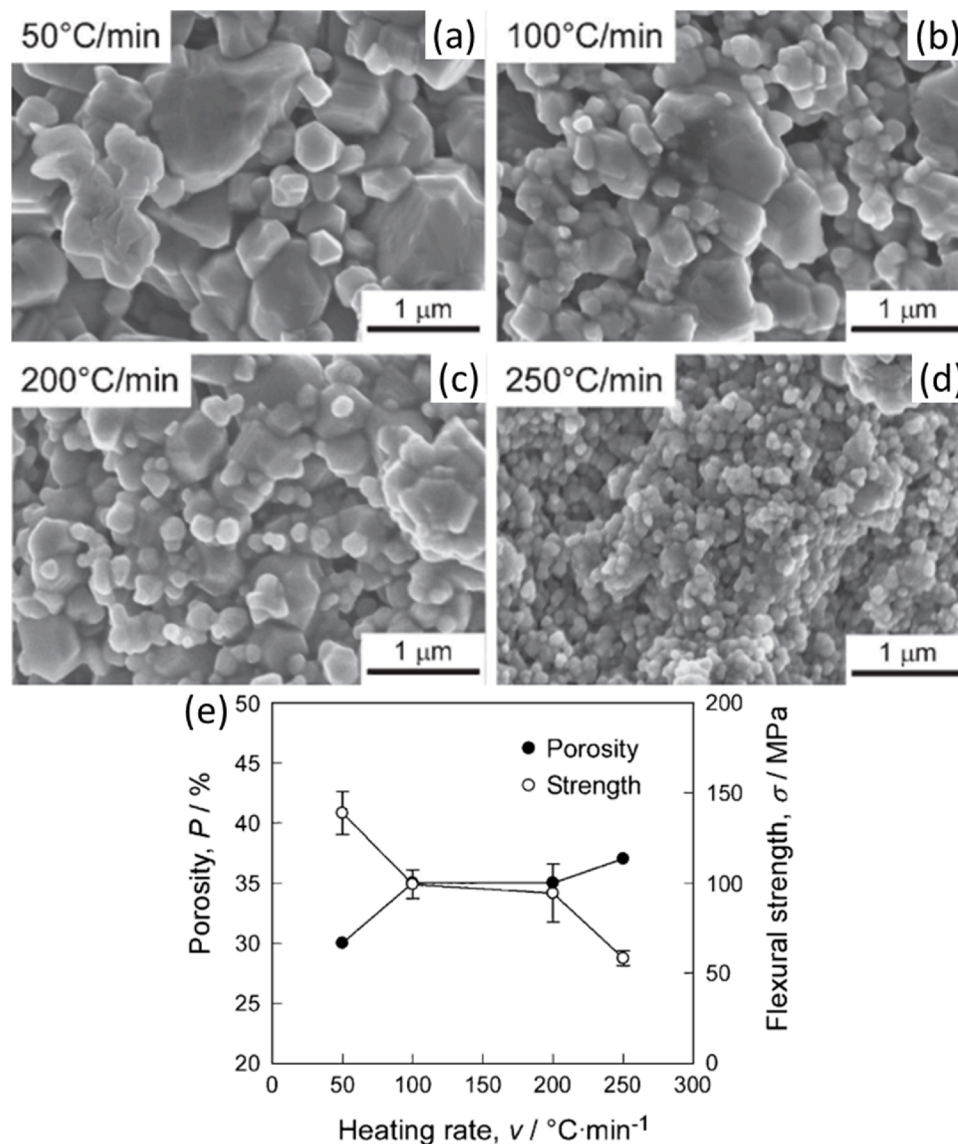


Fig. 5. (a-d) SEM micrographs of SiC ceramics prepared at heating rates from 50–250 °C/min. (e) Effect of heating rate on the porosity and flexural strength of porous SiC ceramics. Reproduced with permission [32]. Copyright 2012, The Ceramic Society of Japan.

strength of porous ceramics is provided by the limited contact points, i.e. the corresponding solid necks, among particles formed via mass transport that is thermodynamically driven by the minimisation of surface energy [3]. Overall, the mechanical properties of porous ceramics mainly depend on the porosity, pore size, degree of neck growth among grains or shielding effects (bridging and pull-out) of aligned fibrous grains [1,20].

Sintering temperature has a direct impact on the final ceramic

Table 2

List of sintering additives and their roles in the fabrication of porous SiC and Si₃N₄.

Materials	Sintering additives	Function of additives	Refs
SiC	MgO-Al ₂ O ₃ -SiO ₂ , Al ₂ O ₃ -Y ₂ O ₃	Grain growth accelerator: enhance densification via liquid-phase sintering, lower sintering temperature	[35, 36]
	α -Al ₂ O ₃ , AlN-Y ₂ O ₃ , AlN-Al ₂ O ₃	Grain growth inhibitor: interfere mass transfer	[18, 32]
	Al ₂ O ₃ -Y ₂ O ₃ , Y ₂ O ₃	Grain growth accelerator promotes densification, decrease the phase transformation temperature	[16, 17, 37]
Si ₃ N ₄	Yb ₂ O ₃ , Li ₂ O, Sm ₂ O ₃ -CaO		

structures. A. Kocjan and Z. Shen prepared porous yttria-stabilised tetragonal zirconia (Y-TZP) nanoceramics with hierarchical heterogeneities, using a partial sintering technique [22], and they illustrated the microstructural revolution of the partially sintered sample, as shown in Fig. 4(a–e). When the sample was pre-treated at 600 °C, intra- and inter-particles pores (intra-particles were coloured in white, and inter-particles were in black) formed originating from the dense and homogeneous packing of the loosely aggregated particles. An increased relative density and the formation of necking were obtained when the sintering temperature reached 1000 °C, where the pore size increased as pores were merged due to the surface-energy minimisation. Higher sintering temperatures up to 1100 °C and 1150 °C led to the annihilation of intra-particle pores and secondary growth of the particles. As a result, the pore area and porosity of the material were significantly decreased, accompanied with a pronounced densification. The relationship between sintering temperature and pore area and porosity are shown in Fig. 4f. The resulting materials sintered from 600 °C to 1150 °C exhibited a porosity from 46 % to 18.3 %. This leads to attractive properties, such as much reduced thermal conductivities of 0.63–1.88 Wm⁻¹ K⁻¹, increased bending strengths of 70–540 MPa, and lowered elastic moduli of 32–156 GPa [22].

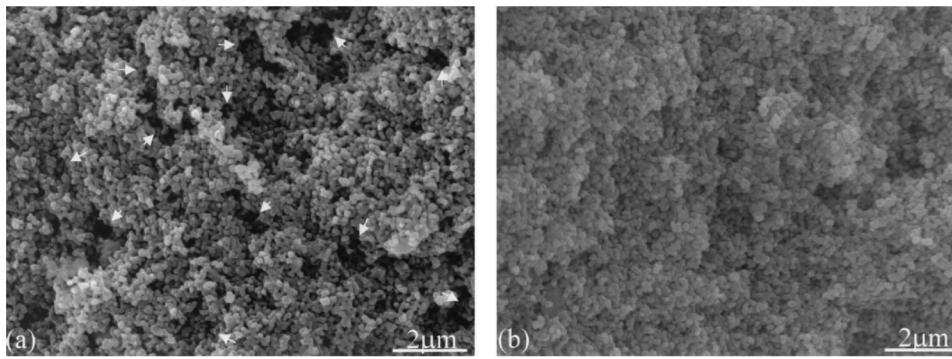


Fig. 6. SEM image of porous ZrO_2 sintered from (a) Z40 compact with a porosity of 47.4 % (prepared at pressure of 30 MPa), and (b) Z44 compact with a porosity of 44.5 % (prepared at the pressure of 75 MPa). Reproduced with permission [23]. Copyright 2002, John Wiley & Sons, Inc.

Heating rates also have a strong influence on the porosity, and a fixed or multiple heating rates could generate different microstructures for the ceramics. Hotta et al. investigated the effect of heating rate for sintering porous SiC using multiple heating rates [32]. As shown in Fig. 5a-d, with the increase of heating rate from 50 to 250 °C/min, the porosity increased from 30 to 38 %, while the grain size of SiC decreased. This is understandable, as higher heating rate is accompanied with reduced heating time, which allows for shorter diffusion and growth time for the grains, hence reduced grain size and increased porosity, and subsequently, lower mechanical performance (Fig. 5e).

As for ceramics systems with low sinterability, their densities show little dependency on the sintering temperature [34]. In this case, sintering additives are employed to accelerate and decelerate the grain growth, to precisely control the density and porosity of resulting materials. These have been intensively studied for the sintering of SiC and Si_3N_4 , as summarised in Table 2. Lei et al. prepared porous β - Si_3N_4 ceramics [17]. They first sintered them at 1600 °C in N_2 , using 0.66 wt% Li_2O and 0.33 wt% Y_2O_3 as sintering additives, followed with a vacuum heat treatment (VHT) at 1500 °C. It is believed that the addition of Li_2O enabled the formation of Li-Si-O-N liquid phase with low viscosity, which promoted the partial sintering and phase transformation at low temperature; whereas the Y_2O_3 facilitated the growth anisotropy of β - Si_3N_4 . Because β - Si_3N_4 has a high aspect ratio, it enhanced the flexural strength of the final treated ceramics. Fukushima et al. reported the preparation of macroporous SiC by employing α - Al_2O_3 as an sintering additive [18]. They considered that SiC particles were covered by a liquid SiO_2 - Al_2O_3 layer that formed during the sintering, this layer acted as a grain growth inhibitor by interfering the mass transfer from particle surface to neck area. Indeed, they have obtained submicrometer-sized pores in the range of 0.03–0.70 μm via such an additive modulation. Although the use of sintering additive for controlling the microstructure of SiC and Si_3N_4 has been widely documented, the utilisation of sintering additives for partially sintering other porous ceramics has rarely been reported.

2.1.2. Advanced sintering techniques for enhanced mechanical strengths

Partial hot-press technique is the first option that is applied to control the porosity of ceramics [26]. However, as powder compacts are sintered to an incomplete degree of densification, the premature termination of the diffusion/growth inevitably results in degraded strength and durability for porous ceramics [38]. In this regard, applying compaction pressures to the green body before sintering is thus beneficial for reducing particle agglomeration and increasing the interface bonding strength. A uniform microstructure is one of the fundamental requirements for better mechanical properties (Fig. 6a,b) [23]. The lengthy process of hot-press is not only time consuming but also involves high demand for energy. Its slow heating rates, non-uniform heating, and overall inability to control the diffusion and necking that determines the final pore size and shape of the ceramics, limit its high-level applications. However, as a conventional process, hot-press has its advantages of convenient and easily accessible.

To precisely control the porosity and create extensive and accelerated necking between grains, spark plasma sintering (SPS), which is also known as pulsed electric current sintering (PECS), has been utilised for the fabrication of hierarchical porous ceramics with well-defined macroscopic morphology, slightly lower porosity, and higher mechanical stability than those produced by hot-press [27,29]. Unlike hot-press that uses external heating source, the SPS provides current that passes through the die and the sample, which results in the ionisation of the gas around the powder particles [39]. The rapidly heated powders that are assembled into relatively strong porous bodies are subjected to constant pressures, therefore a preferential necking growth of the powders is induced by selective local heating among particles, making the sintering occurs more quickly [32,40]. This will help retain fine pores and provide good control over the microstructural development and densification. Oh et al. has compared the hot-press with SPS techniques for the fabrication of Al_2O_3 [41]. As shown in Fig. 7a,b, the Al_2O_3 prepared by SPS exhibits grain refinement and neck growth, which will benefit the fracture strength of the final products.

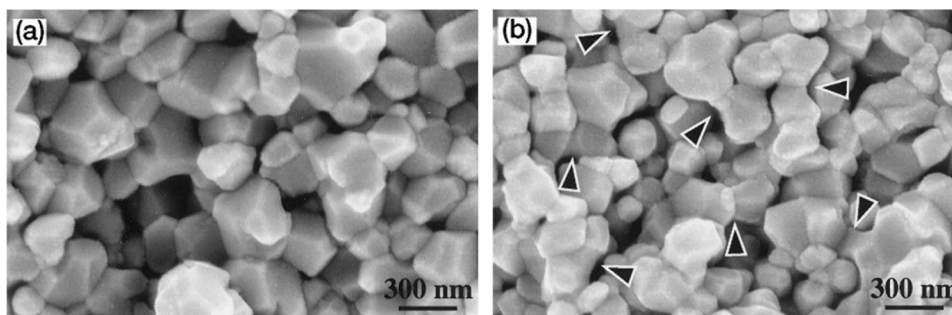


Fig. 7. SEM images of the fracture surfaces of monolithic Al_2O_3 with a relative density of 81 %, sintered via (a) hot-press at 1300 °C for 15 min, and (b) SPS at 950 °C for 15 min (necking growth in SPS is indicated by arrows). Reproduced with permission [41]. Copyright 2000, John Wiley & Sons, Inc.

Table 3

Sintering conditions, porosity, average grain size, bending strength, and surface area of SPS Al_2O_3 samples. Reproduced with permission [30]. Copyright 2009, Elsevier B.V.

Sintering temperature (°C)	Applied pressure (MPa)	Porosity (%)	Average grain size (μm)	Bending strength (MPa)	Surface area (m^2g^{-1})
1000	10	63.0 ± 3	–	3 ± 1	80 ± 5
1050	10	55.5 ± 3	–	10 ± 3	58 ± 5
1050	20	40.0 ± 4	0.05	50 ± 8	30 ± 3
1050	30	25.0 ± 4	0.15	250 ± 12	8 ± 2
1050	50	20.0 ± 3	0.2	400 ± 25	4 ± 1
1100	10	30.5 ± 5	0.1	150 ± 10	10 ± 2
1150	10	25.0 ± 3	0.15	250 ± 14	7 ± 1
1200	10	20.0 ± 5	0.2	375 ± 20	4 ± 1

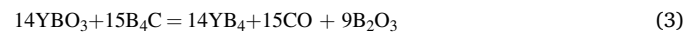
Chakravarty et al. fabricated porous Al_2O_3 via SPS [30], and they studied the effect of sintering temperature and applied pressure on the microstructural features and mechanical properties of the resulting materials. They have found that with the increases of the temperature and pressures, the pore size distribution became wider and the distribution peak shifted to higher values. As a result, the bending strength increases, due to the formation of necking among grains; and the grain size increases with the rise of temperature, due to accelerated grain growth. However, the surface area decreased due to the coalescence of the fine pores, as illustrated in Table 3. Therefore, a narrow pore size distribution and significantly increased fracture strength would result from the SPS partial sintering.

Using this technique, by applying uniaxial pulsed electric current during sintering could lead to highly oriented grains formed in one direction, which would generate anisotropic thermal and mechanical properties for the materials. Honda et al. realised such porous alumina sintered by utilising SPS, and achieved oriented grains and pores [42]. They reported that the bending strength and thermal conductivity of porous alumina were 404 MPa and $22.4 \text{ W} \cdot \text{m}^{-1} \text{K}^{-1}$, separately, parallel to the pressing direction, whilst these values changed to 217 MPa and $10.8 \text{ W} \cdot \text{m}^{-1} \text{K}^{-1}$ perpendicular to the pressing direction.

Although the rapid heating of SPS provides the possibility for obtaining porous ceramics with lower heating temperature and shorter dwell time, the original architecture of porous ceramics created from other pore forming strategies such as replica template and sacrificial template cannot be well-preserved by either pressure-less SPS or pressure-assisted SPS due to the inherent features of SPS [43], which limits the utilisation of SPS for pre-formed porous ceramics. Meanwhile, more quantitative investigations of the fundamentals of the electric current behaviour during SPS should offer more insights for revealing the relationship between current, plasma and particles, therefore achieving enhanced capacities for better manipulation of microstructures of the products.

2.1.3. In-situ reaction for improved porosity

Partial sintering can be combined with in-situ chemical reaction to generate porosities greater than 50 %, by taking advantages of the gas emitted during the reaction and applying it as the pore-forming agent. Using an in-situ borothermal reaction (Fig. 8), Guo et al. reported the preparation of porous YB_4 ceramics [20]. Y_2O_3 and B_4C were used as the starting materials, after sintering at 1650 °C and 1780 °C respectively for 2 h under vacuum, YB_4 was formed. They also suggested a multi-step reaction mechanism, as follow:



During the reaction, pores are produced by the release of B_2O_3 and CO gases, thus leading to a relatively high porosity of 60–70%, as well as very narrow pore size distribution. Similarly, Wang et al. prepared porous YbB_6 ceramics from in-situ reaction between Yb_2O_3 and B_4C under partial sintering conditions [21], and they obtained porous YbB_6 with high compressive strength of 21.34 MPa with a porosity of 58.7 %.

The combination of partial sintering and in-situ reaction process offers several merits, including: (1) Higher porosities without the use of separate pore-forming agent; (2) Simple process without residue of by-products; (3) Controllable porosity and volume shrinkage by tuning the ratio of reaction precursors and adjusting the pressure applied when preparing the green body for desired densities; (4) Homogeneous pore structure and narrow pore size distribution. However, this technique is only applicable for the fabrication of porous ceramics that involves gaseous reactions.

Partial sintering is believed to be a facile and cost-effective way for the fabrication of porous ceramics by simply adjusting the sintering conditions and sintering aids. However, partial sintering has several essential drawbacks: low porosity, limited sinterability of coarse powder, and uncontrolled pore morphology [29,37], which have limited its wide range of application. To overcome these issues, sacrificial pore formers such as corn starch [44], and potato starch [45,46], can be added to escalate the porosity, which is classified as the sacrificial template method.

2.2. Replica template

The replica method is a common and effective technique for the fabrication of open-celled porous ceramics with interconnected pores and large surface areas [47]. This method is based on the impregnation of open-celled porous polymeric foams functioning as a template in a ceramic slurry, followed with a thermal treatment [48]. During heating stage, the organic polymeric substances are decomposed while the ceramic remains [49]. As a result, porous ceramics that duplicate the morphology and structures of the parental polymer template are

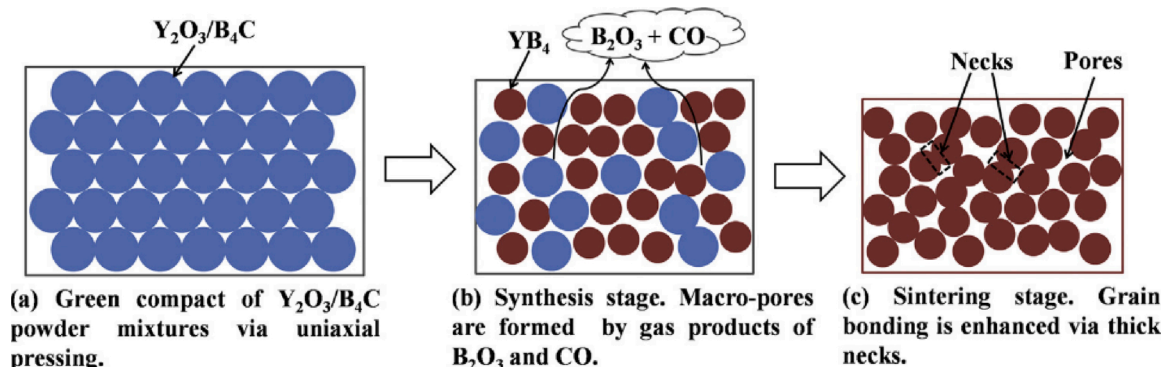


Fig. 8. Schematic of the pore evolving process during the preparation of porous YB_4 ceramics. Reproduced with permission [20]. Copyright 2015, Elsevier B.V.

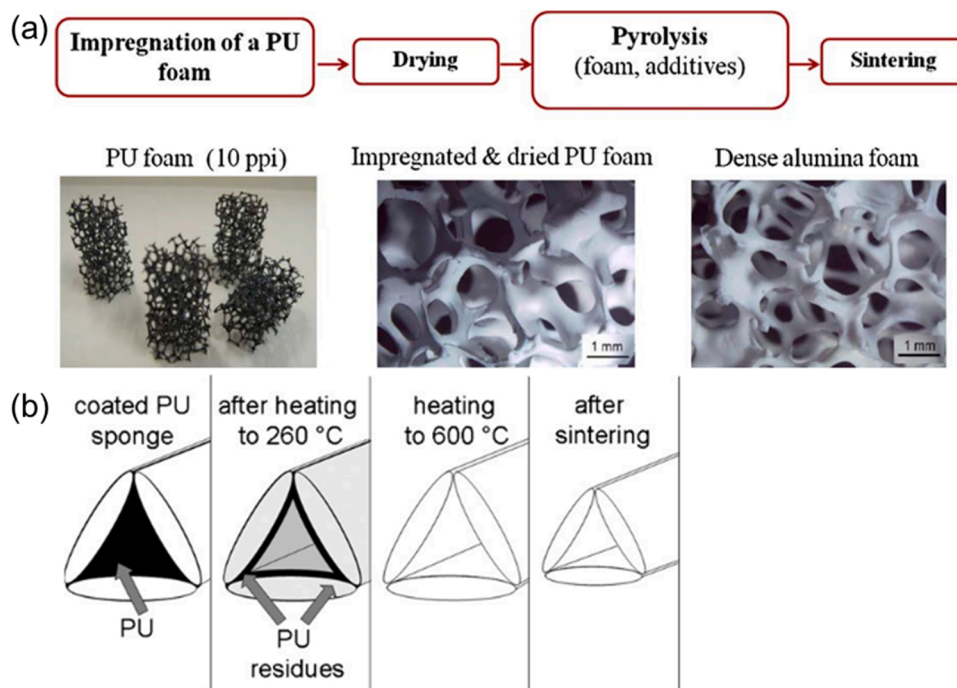


Fig. 9. (a) Process flow for the preparation of alumina foams using a PU replica template. Reproduced with permission [64]. Copyright 2010, Elsevier B.V. (b) An illustration of various stages occurred during heating: the coated sponge, PU burnt out, pore formation, and ceramic shrinkage. Reproduced with permission [66]. Copyright 2009, Elsevier B.V.

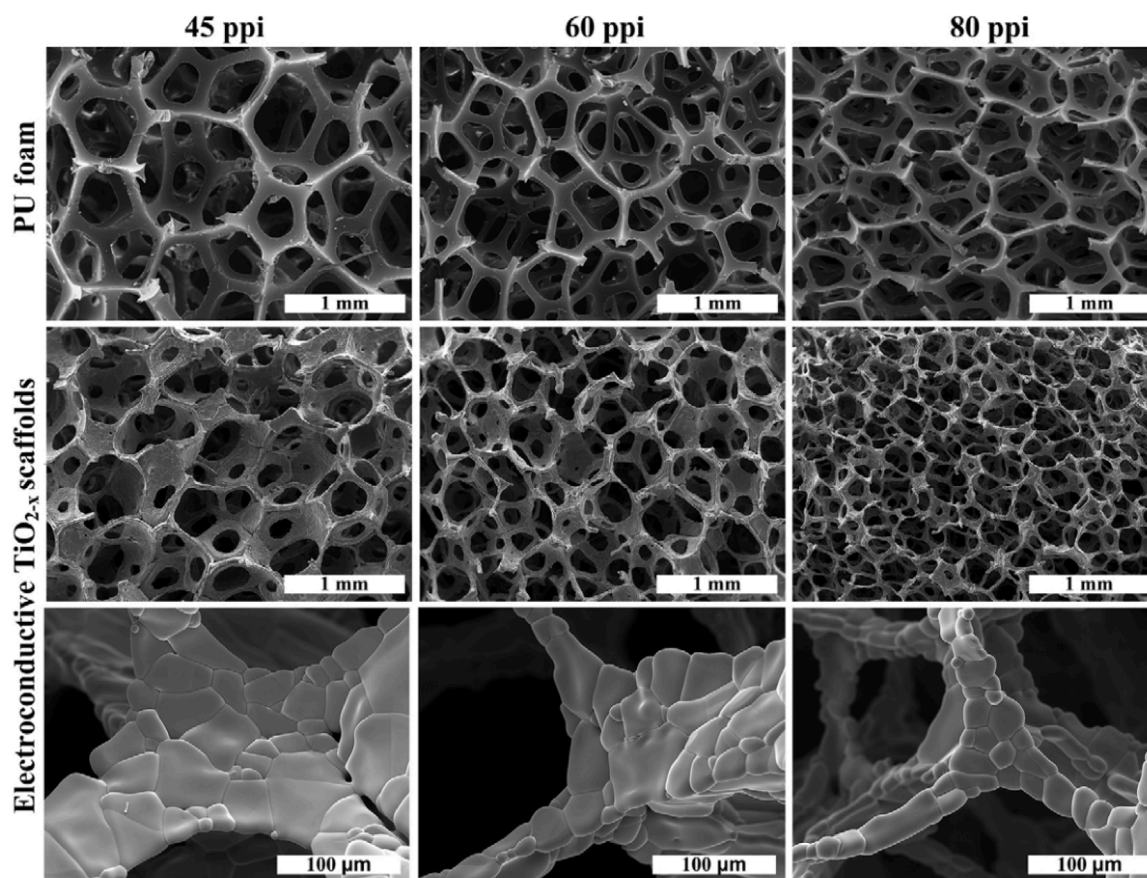


Fig. 10. SEM micrographs of different PU foam templates and their corresponding electroconductive TiO_{2-x} scaffolds resulted. Reproduced with permission [69]. Copyright 2016, Elsevier B.V.

obtained [50]. The replica technique provides a good control over the key morphological and microstructural characteristics of the final products [51]. Solid foam sponges, both polymeric sponge such as polyurethane and natural sources such as woods, cellulose, and marine sponge can be used as templates to achieve open porosities over 70 % [52]. In addition, the selection of templates and slurry media plays a decisive role in determining the porosity and mechanical properties of the final porous ceramics [53]. The reticulated porous ceramics fabricated via the replica method are typically used as gas exhaust catalyst devices [54], burners [55], scaffolds for bone tissue engineering [56–59], catalysts support [60], and in nanoreactor applications [61].

To begin this process, a reticulated foam is coated with a ceramic slurry mixture by dipping it into the slurry and squeezing the foam to get rid of the excessive slurries after each impregnation. The squeezing procedure can be used as an approach to control the solid loading, which is inversely proportional to the applied strain. More than one impregnation sometimes is required to increase the solid loading and fill out the voids in the sponge [62]. The dried template is burnt out during the next sintering procedure, leaving behind a sintered ceramic with pores virtually equivalent to the volume of the polymer template (Fig. 9a,b). However, the burning of the organics will generate gases, hence the resulting ceramic hollow struts unavoidably contain triangular voids and longitudinal defects [63]. Faure et al. fabricated alumina foams via the impregnation of polyurethane (PU) foams with pore size of 10 ppi (pores per inch), 20 ppi, and 30 ppi, respectively [64]. Their immersion and drying processes were repeated for several times to ensure that the template was fully coated with the alumina slurry. The calcination consisted of two stages, corresponding to the pyrolysis of template and the sintering of alumina. Using this technique, they reported their

alumina foam containing a high porosity, ranging from 80 to 95 %, which is obviously higher than the previously reported partial sintering techniques in section 2.1. A novel bioactive TiO₂ scaffolds was created by Loca et al. via the replica method [65]. They demonstrated that all resulting TiO₂ scaffolds exhibited a fully open and interconnected pore structure, with a high porosity of 92 ± 2% and pore sizes in the range from 300 to 700 μm, which is very impressive.

2.2.1. Selection of template

The main advantages of the replica method is the easy control of the pore geometries and pore size, which can be realised by selecting suitable original sponge templates [67,68]. The exact features of the initial polymeric templates, including the pore size and porosities, can be transferred to the final products, thus this technique is attractive for a wide range of industrial applications. For example, Narkevica et al. prepared porous TiO_{2-x} ceramic scaffolds from PU foams of different pore size (45 ppi, 60 ppi, 80 ppi) [69], and electrically active materials with a porosity over 95 % were obtained (Fig. 10). The pore sizes of the scaffold are highly related to those of the original PU foams (100–700 μm for PU with 45 ppi, 80–520 μm for PU with 60 ppi, and 70–350 μm for PU with 80 ppi). Commonly used templates, as well as their microstructural features, suitable for the replica method are summarised in Table 4.

Although the most widely used templates are PU foams, natural sources with anisotropic features have also been utilised for obtaining biomorphic porous ceramics with highly orientated structures. Boccardi et al. used natural marine sponges as a replication template and successfully fabricated the bioglass based foams [86]. These foams have much lower porosity of merely ~18–20%, better mechanical strength

Table 4
Suitable replica templates and their corresponding porous ceramics resulted.

Materials	Template	Porosity (%)	Pore size (μm)	Applications	Refs
Al ₂ O ₃	PU	71–90	–	–	[9]
Al ₂ O ₃	PU	80–95	–	Catalyst support for industrial steam reforming processes	[64]
Al ₂ O ₃	PU	80.4–83.3	–	–	[70]
BCP (biphasic calcium phosphate)/ZrO ₂	PU	68	220	Bone substitutes	[47]
Bio-silicate	PU	95	200–500	Bone tissue engineering	[56]
Boron-containing glass	PU	85–90	200–400	Bone tissue engineering	[71]
Ca ₂ MgSi ₂ O ₇	PU	88 ± 2	200–400	Dental tissue engineering	[72]
Mg-containing silicate	PU	>90	300–600	Bio-scaffold	[73]
Si ₃ N ₄	PU	67.15–88.91	–	Liquid metal infiltration	[74]
SiC	PU	77	–	–	[75]
Si ₃ N ₄	PU	65–75	300–1000	Bone substitute	[57]
Si-SiC	PU	>80	–	–	[48]
Ti ₃ AlC ₂	PU	80	710 ± 50	Gas exhaust catalyst devices	[54]
TiO ₂	PU	86–92	200–500	Scaffold application	[76]
TiO ₂	PU	>90	300–700	Bio-scaffolds	[65]
TiO ₂	PU	>95	70–700	Bio-scaffolds	[69]
ZTA (zirconia toughened alumina)	PU	>90	–	–	[77]
Al ₂ O ₃	Polymeric sponge	88.9	–	–	[78]
HA	Polymeric sponge	79–91	>300	Bone scaffolds	[79]
HA	Polymeric sponge	60	50–125	Bio-scaffolds	[59]
SiC	Polymeric (melamine) sponge	84	135	Oil/water separation	[80]
Bioactive glass	Mediterranean Sea marine sponge SL/ Indian-Pacific Ocean marine sponge (SA)	76.42 ± 2/ 68 ± 0.2	265 ± 20 215 ± 2.7	Bone tissue engineering	[81]
SiC	Carbon preform from wood	45–72	15.7–19.2 (radial)/ 32–58 (axial)	Hot-gas filtering applications	[68]
SiC	Porous glass	~50	0.01–0.05	Filter, membrane, catalyst support	[82]
SiC	Wood: Danish beech wood/ Indian pine/ Indian mango/ silk cotton tree	–	5–25	–	[83]
Si-SiC	Tannins-derived natural resins	96	<200	–	[84]
YSi ₂	Luffa cylindrica	–	–	Burner	[55]
Y ₂ O ₃	Cotton-nylon netting	–	–	Burner	[85]
ZrB ₂	PU/ Clot sponge/ Natural sponge/ Cellulosic sponge	>85/ 71/ 71/ 70	–	Lightweight ultrahigh temperature ceramic (UHTC) devices	[52]

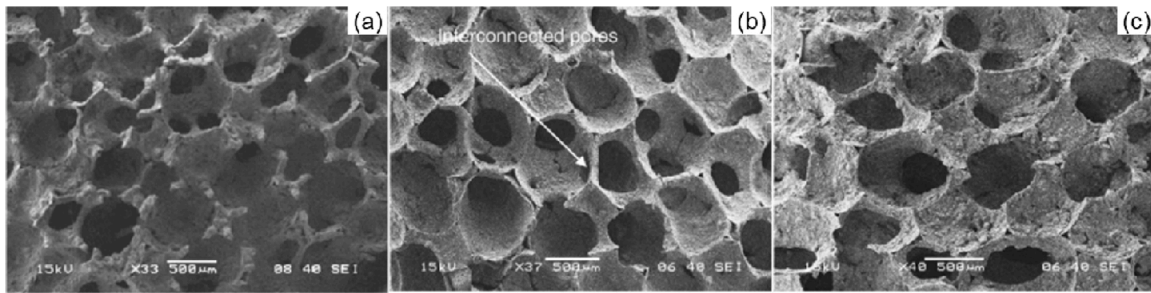


Fig. 11. SEM images of sintered HA scaffolds with varying solid loadings. (a) 30 %, (b) 40 %, (c) 50 %. Reproduced with permission [59]. Copyright 2011, Elsevier B.V.

up to 4.0 MPa, compared with foams obtained by using PU templates (< 0.05 MPa), without sacrificing the pore interconnectivity (> 99 %). This result opened the possibility of using natural sponges as alternatives to PU templates for applications where high mechanical strengths are essential. However, ceramic foams from natural marine sponge templates exhibited high shrinkages around 50 % after sintering, due to the dehydration of the biogenic sponge skeleton. The shrinkage of cellulose-based sponges can be controlled by lowering the heating rate, but lamellar struts and irregular-shaped pores are still unavoidable [52].

Using wood as templates was also investigated, since activated carbon preforms are easily obtained by pyrolytic decomposition of wood. Followed by infiltration, pyrolysis, and reaction at high temperatures, porous ceramics can be produced. However, it is noteworthy that porous ceramics with biomorphic microstructures derived from replicating of woods have similar drawbacks, which refer to the low porosity, poor mechanical strength, requirements of multiple steps of processing, and difficulty for scaling up [87]. These results suggest that the synthetic polymeric templates better off natural resources in terms of the reliability and structural integrity. High quality polymeric templates with good control of pore shape, pore size and strut geometry could lead to the desired porous ceramics. However, to develop new techniques based on sustainable templates for specific applications is still an interesting area for future research, particularly wood and other natural materials offer a huge diversity to suit for different purposes. Obviously, the processing parameters in each step need to be thoroughly investigated and optimised.

2.2.2. The role of ceramic suspensions

Complex structures of a material can be well-preserved during the thermal treatment by carefully controlling the heating rate and temperature slope. However, the influences of the rheological properties, level of shear thinning, and viscosity of the coating materials should be taken into consideration, first. To achieve an efficient infiltration process with scaffolds uniformly impregnated, the slurries are generally required to exhibit a pseudo-plastic or shear-thinning (Non-Newtonian) behaviour [88]. On one hand, the viscosity of the slurries must be low when a high shear rate is applied during the compression-expansion steps, enabling an easy coating on the substrate. On the other hand, the viscosity should be high when the shear rate declines at the end of the impregnation process, allowing sufficient slurry to cling onto the substrate [62,85]. Gomez et al. investigated the relationship between the rheological behaviour and the final structures of ceramic foams [49], they found that the optimised viscosity of ceramic suspension leads to an increased thickness of the ceramic coating, which assists smoothing the struts of the ceramic foam, decreases the defects at the corners of struts, and enables the final ceramic foams to achieve good mechanical strength.

It is worth mentioning that the major disadvantage of this method is the defects and cracking of porous bodies created during thermal decomposition of the polymeric sponge, which resulted in a reduction of their final mechanical strength [67,70]. In this regard, the solid content

Table 5

Porosity, density, and appearance of sample as a result of different bentonite solid content (wt%). Reproduced with permission [74]. Copyright 2013, Springer Nature Switzerland AG.

Bentonite rate (wt.%)	Porosity (%)	Density (g cm^{-3})	Appearance
5	88.91	0.35	Highly open porous
10	86.37	0.44	Highly open porous
15	83.13	0.54	Highly open porous
20	78.12	0.70	Highly open porous
25	76.13	0.76	Some closed pores
30	71.14	0.92	Mostly closed pores
35	67.15	1.05	Closed porosity

of the slurry precursor, which affects the viscosity of the slurry and decides the density of the resultant materials should be controlled, in order to obtain a moderate porosity, high pore interconnectivity and improved mechanical behaviour for the final products. Swain et al. reported the preparation of porous scaffold from hydroxyapatite (HA) [59]. The optimum pore morphology, distribution, interconnectivity and compressive strength were recorded for samples with 40 wt.% solid loading in the slurry (Fig. 11 a-c). In another case, TiO_2 scaffolds of high mechanical properties were obtained from slurries having 70 wt.% solids content [76]. Therefore, optimal contents of slurries need to be investigated for different ceramic systems aiming to specific properties.

Furthermore, to increase the reliability of replica template method, additives including binder, dispersant, and thickener can be selectively used to improve the rheological behaviour of suspensions, and in turn the mechanical properties of both the green body and the sintered product. Binders are used to improve the rheological behaviour of the slurries and the adhesion of slurry on the template. Caliskan et al.

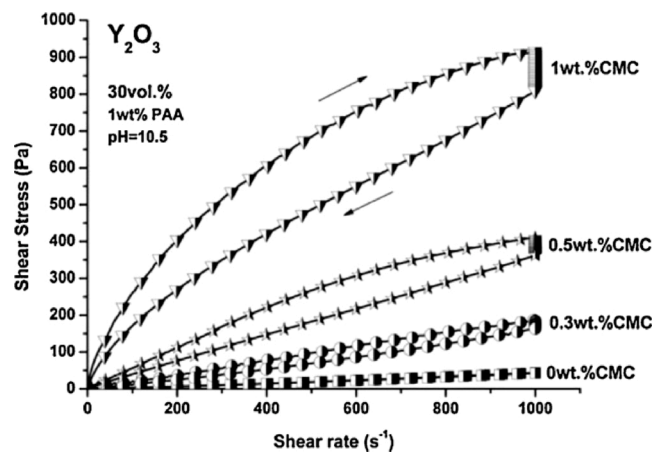


Fig. 12. Control rate (CR) flow curves of Y_2O_3 suspensions with 30 vol% solid content as a function of carboxymethyl cellulose (CMC) concentration from 0 to 1 wt.%. Reproduced with permission [85]. Copyright 2014, Elsevier B.V.

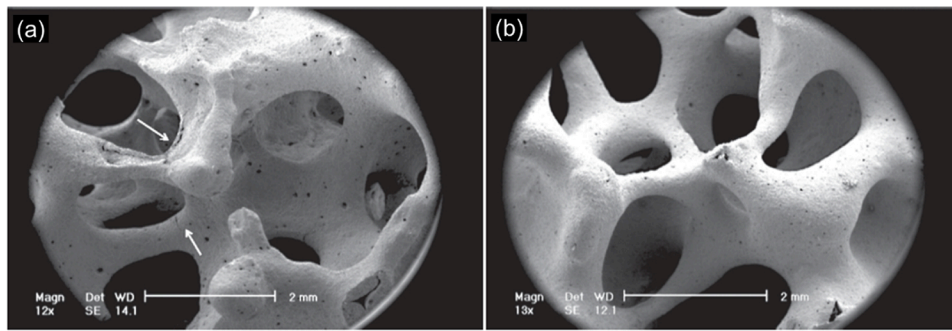


Fig. 13. SEM photographs of an Al_2O_3 foam prepared using: (a) 60 wt.% solid content slurry and (b) 66 wt.% solid content slurry. Defects such as cracks and micropores are eliminated by increasing the solid content of slurry. Reproduced with permission [70]. Copyright 2015, Institute of Rock Structure and Mechanics of the CAS & University of Chemistry and Technology, Prague.

developed Si_3N_4 preforms and investigated the influence of bentonite as a binder on the porosity, density, and appearance of preforms [74]. As shown in Table 5, the level of porosity, density and pore structures can be controlled by the content of bentonite. It was found that open pores started to close when the bentonite rate was up to 20 wt.%. For this reason, 15 wt.% was believed to be the optimum bentonite rate, which facilitated the protection of sponge morphology and allowed to produce near-net-shape ceramic foams. As shown in Fig. 12, Santos et al. used 0.3–1 wt % carboxymethyl cellulose as an additive to prepare the Yttria suspension, and they found that the flow behaviour changed from linear to shear-thinning in the slurry [85]. A combined effort to consider the different additives and the precursor template is required to achieve near-net-shape ceramic foams.

Opposite to binders, the adsorption of dispersants onto particle surfaces hinders the agglomeration and sedimentation of the ceramic suspension by electro-steric mechanism, which gives rise to optimum fluidity, promotes stability of suspensions, and improves the efficiency of powder packing. These effects will endow the ceramic foams a smooth stress concentration and high strengths [49,76]. Hadi et al. documented the creation of open-cell Al_2O_3 foams with a desirable mechanical strength by adding Tiron as the dispersant [70]. When Tiron was adsorbed onto the particles, due to the electrostatic and hydrogen bond interactions, the particle surfaces were then charged, which led to a highly repulsive potential between particles and therefore a decreased slurry viscosity. At an optimum Tiron concentration of 0.8 wt.%, the solid content in the slurry can be increased from 60 to 66 wt.%, and defects in the Al_2O_3 foam were considerably reduced (Fig. 13a,b). As a result, an increase in mechanical strength from 1.33 to 3.24 MPa was recorded [70].

It has been found that the rheological properties of slurries,

especially the viscosity and thixotropy are prominently improved with the addition of a thickener. The thickener will bring in a notable shear-thinning behaviour to the slurry (Fig. 14a,b), leading to good coatings [88]. Many works have confirmed that a proper selection of different sintering additives is essential to produce near-net-shape components with highly densified struts. Examples of porous ceramics prepared via replica template with an optimum amount of additives are summarised in Table 6, as a guidance on the selection of additives.

2.2.3. Additional process for enhancing mechanical properties

The high porosity of materials exhibits low mechanical strength, which limits their wide applications in many fields including the energy and environment sectors [75]. To overcome this issue, various techniques such as re-infiltration [89], additional coating [73], and template surface pre-treatment [78], etc. have been adopted to enhance the thickness and homogeneity of slurry impregnated ceramics.

The microstructures of the resulting foams are closely associated with the slurry coating times. Chen et al. used different PPI (pores per inch) values and coating times on polymer sponge templates to investigate these effects for the synthesis of SiC foams [75], and they found a linear relationship between the strut diameter and coating times (Fig. 15a). After the fifth coating, the strut diameter was doubled, however the porosity declined with increased coating times, but still above 70 % for all samples (Fig. 15b). Vogt et al. investigated the re-infiltration impacts on the strut thickness [89], and by filling up the hollow struts an increased mechanical strength of the porous ceramics was observed, as shown in Fig. 16. The geometrical density and strength of obtained foams increase linearly with the coating cycles.

Additional infiltration of a second phase has also been attempted to further increase the mechanical stability and eliminating microcracking.

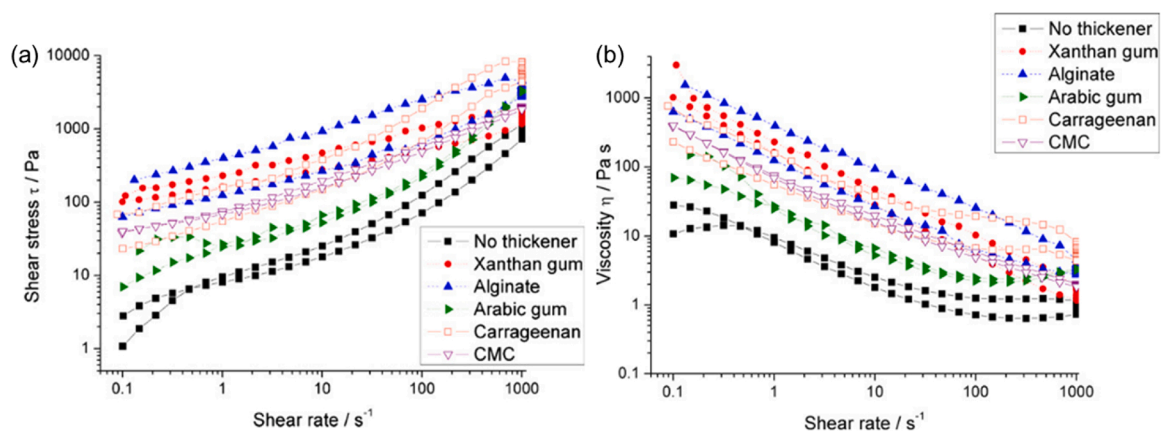


Fig. 14. (a) Shear stress and (b) viscosity of slurries as a function of the shear rate with different thickeners. Reproduced with permission [88]. Copyright 2015, John Wiley & Sons, Inc.

Table 6

Examples of porous ceramics prepared via replica template with an optimum amount of additives.

Slurries	Binder	Dispersant (deflocculant)	Thickener	Others	Refs
Al ₂ O ₃	Colloidal silica (Syton 30X) (10.6 wt%)/ albumin (22.6 wt%)	–	–	–	[67]
Al ₂ O ₃	polyvinylacetates	Ammonium polymethacrylate	–	Wetting agents: octan-1-ol, docan-1-ol Antifoaming agents: polyether siloxane	[64]
Al ₂ O ₃	Polyvinyl alcohol (PVA)	Tiron (0.8 wt. %)	–	–	[70]
Al ₂ O ₃	Optapix AC 170	Dolapix CE 64	Xanthan gum (0.5 wt. %)/ Aodium alginate (0.5 wt. %)/ Arabic gum (0.5 wt. %)/ Carrageen (0.5 wt. %)/ Carboxymethyl cellulose (CMC) (0.5 wt. %)	Wetting agent: Polypropylene glycol P400	[88]
Al ₂ O ₃	Egg white protein (10 wt. %)	Darvan 821A	–	Defoamer: 1-octanol	[9]
Al ₂ O ₃ / (ZTA)	Polyvinylalcohol (PVA) (1.5 wt%)	Dolapix CE 64 (0.84 wt. %)	–	Anti-foaming agent: Constraspum KWE	[77]
BCP/ ZrO ₂	Polyvinyl butyral (PVB)	–	–	–	[47]
CaP	–	Hypermer KD-4 (4 wt%)	–	–	[58]
HA	PVA (3 wt%)	–	–	–	[59]
HA	PVA (2 wt. %)	Dolapix	–	–	[79]
Mullite	bentonite	Dolapix CE-64	Sodium carboxymethyl-cellulose (CMC)	–	[62]
SiC	Silicone resin/ methylbenzene (C ₆ H ₅ CH ₃)	–	–	–	[75]
SiC	PVB	–	–	–	[89]
SiC	Ammonium lignosulfonate	Polycarboxylate	–	–	[90]
SiC	Silica sol (26.2 wt%)	–	Sodium carboxymethylcellulose (CMC)	–	[91]
SiC	Ammonium lignosulfonate (1.5 wt. %)	Polycarboxylate (0.3 wt. %)	Sodium carboxymethyl-cellulose (CMC) (0.3 wt%)	–	[63]
SiC	–	–	Sodium carboxymethyl-cellulose	–	[92]
Si ₃ N ₄	Bentonite	–	–	–	[74]
Ti ₃ AlC ₂	Silica sol (2 wt%)	Polyacrylic acid (PAA) (2 dwb%) Polyacrylic acid (PAA) (1 wt%)/ Tetraethy- lammonium hydroxide (TMAH)	–	–	[54]
Y ₂ O ₃	Carboxymethyl cellulose (CMC) (0.3 wt%)	–	–	–	[85]
Y ₂ Si ₂ O ₇	Carboxymethyl-cellulose (CMC) (0.4 wt%)	–	Polyacrylic ammonium acid (PAA) (2 wt. %)/ Tetraethy- lammonium hydroxide (TMAH)	–	[55]
ZrB ₂ -SiC	–	Dolapix PC33 (1.5 wt.%)	–	–	[52]

Kim et al. introduced a subsequent dipping process for the sintered ZrO₂ scaffold [47]. As shown in Fig. 17a, a functionally gradient layered structure (FG BCP/ZrO₂) is created by the formation of a BCP-ZrO₂ intermediate layer and a BCP outer layer with a thickness of around 3–5 μm and 2–3 μm, respectively. Interestingly, the interconnected pore features are well preserved. Consequently, the compressive strength increased from 4.3 to 7.2 MPa (Fig. 17b).

Desimone et al. introduced a gelatine coating to the as-sintered biosilicate scaffold (Fig. 18a,b), and found that the compressive strength of the scaffold was significantly improved from 0.06 ± 0.01 MPa to 0.80 ± 0.05 MPa, whilst the interconnectivity of the pores remained unchanged [56].

Therefore, second phase coating appears to be a very effective strategy for achieving high mechanical properties while retaining the interconnectivities, which is of importance for bioceramic scaffold. A fine tune of the second or even third phase materials with adequate concentration and coating cycle would lead to the desired porosities with high strengths. Investigations in this area seem to be understudied, possibly due to the extra steps involved during processing. Furthermore, possible reactions between the different phases during heating would complicate the purity of the porous products. This area of research has yet to be fully addressed.

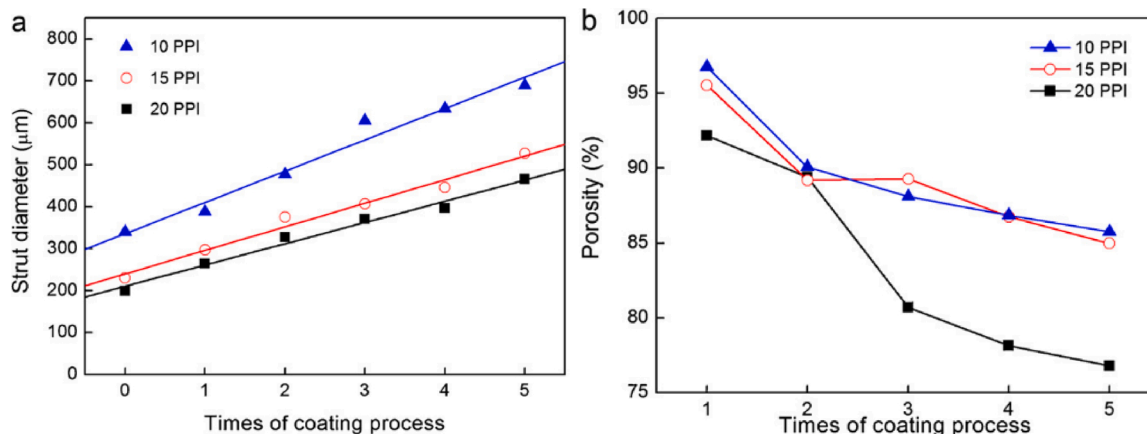


Fig. 15. Effect of coating times on (a) ceramic foam strut diameters; and (b) ceramic foam porosity. Reproduced with permission [75]. Copyright 2012, Elsevier B.V.

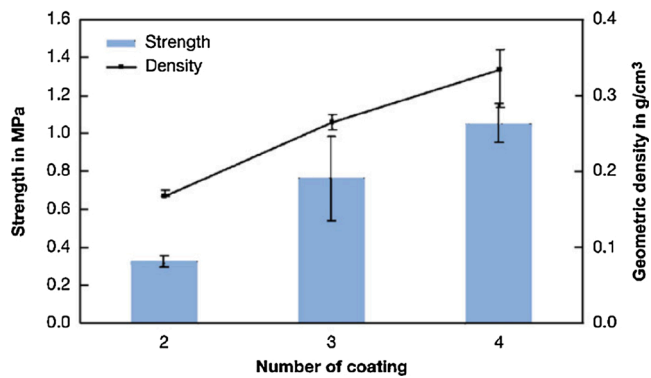


Fig. 16. A linear relationship of the compressive strength and density of foams vs coating cycles. Reproduced with permission [89]. Copyright 2007, Elsevier B.V.

2.3. Sacrificial template

Sacrificial template method is different from the template replica method in that the original configuration of template is copied in the latter, whilst a negative replica of original pore features is created in the former. Therefore, the sacrificial template method has the ability of creating pores of either open-cell or closed-cell. By homogeneously incorporating appropriate amounts of sacrificial porogen, which was subsequently removed via evaporating, burn-off, thermal decomposition, etching, or leaching, the sacrificial template process can generate porous ceramics with desired porosity and mechanical strength.

The starting material is generally a type of biphasic composites,

either a powder mixture of two components, two-phase suspension, or a template impregnated with preceramic polymer or ceramic slurry [2]. It is essential that the matrix materials do not react with the sacrificial materials at elevated temperatures. Frequently used sacrificial porogens have been classified into natural sources (silk [93], Metroxylon sagu [94], etc.); synthetic organics (polyethylene (PE) beads [95], polymethyl methacrylate (PMMA) microbeads [96], gas-filled expandable polymeric microspheres [97], epoxy resin (EP) particles [98], etc.); inorganic matters (graphene sheets [99], mesocarbon microbeads [100], etc.); and frozen liquids (water [101], tert-butyl alcohol (TBA) [102], etc.). The former three sources are generally categorised as non-liquid template, as compared with the liquid counterpart. By choosing proper templates, the morphology of porous ceramics can be tailored. In this process, the type, fraction and dimensional features of the sacrificial template therefore play a key role in determining the size, shape, and structures of the pores, ultimately controlling the properties of resulting materials [103–105]. Detailed parameters affecting these pore characteristics will be presented in the following sections.

2.3.1. Non-liquid template

As shown in Table 7, the materials templated by non-liquid pore formers, as well as resulting pore features and target applications are summarised. It has been demonstrated that porosity is controlled by the volume fraction of the sacrificial template [105]. Konegger et al. utilised polycarbosilane and polysilazane precursors to create polymer-derived SiC-C-N-based ceramic structures [125]. They investigated the relationship between the content of polyethylene (PE) template and the microstructural features of specimens (Fig. 19a-f) and found a direct correlation between the porogen content and the resulting porosities, as shown in Table 8. For ultimate mechanical properties, the template

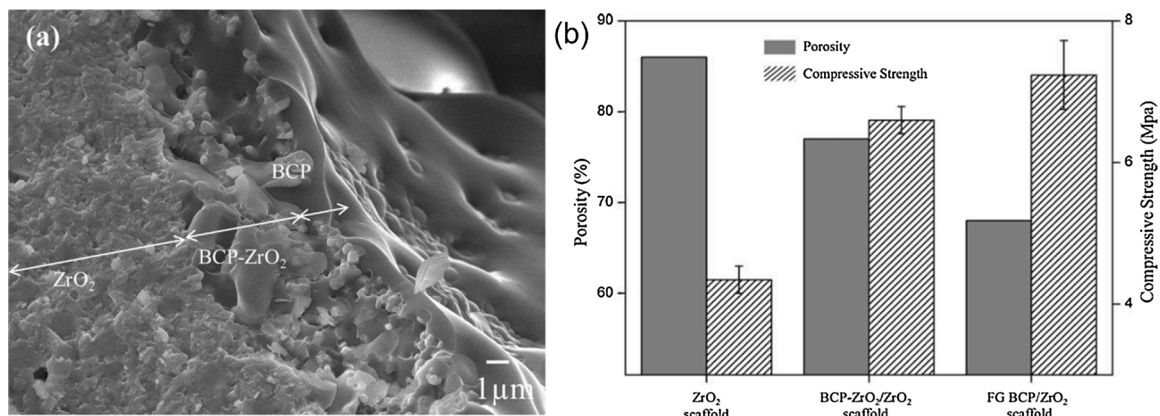


Fig. 17. (a) SEM images of BCP/BCP-ZrO₂/ZrO₂ scaffold. (b) Porosity and compressive strength of different scaffolds. Reproduced with permission [47]. Copyright 2011, Elsevier B.V.

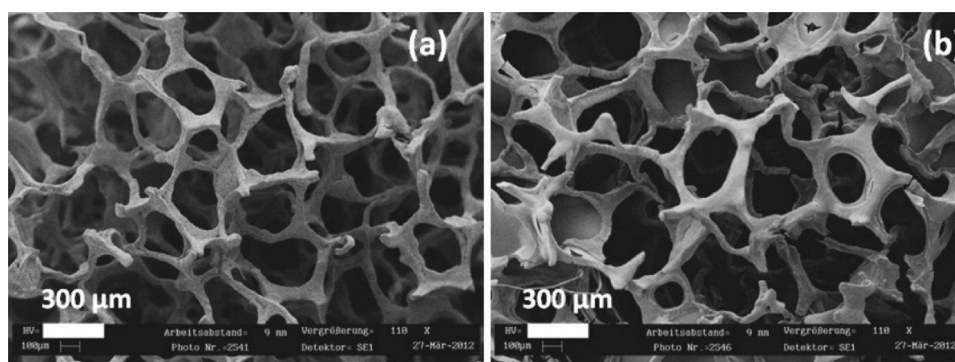


Fig. 18. SEM images of (a) the as-obtained Biosilicate scaffolds, and (b) Biosilicate-gelatine scaffold. Reproduced with permission [56]. Copyright 2013, Informa UK Limited.

Table 7

A list of materials fabricated from sacrificial template with the non-liquid template, porosity, pore size, and applications.

Materials	Template	Porosity (%)	Pore size (μm)	Target applications	Refs
Al ₂ O ₃	Starch	6–47	5–50	–	[106]
Al ₂ O ₃	Gas-filled polymer spheres	<86	15–150	Catalyst support/ bone scaffolds	[97]
(Ba, Sr) TiO ₃	Lamellar graphite	9–29	–	Ferroelectrics	[107]
Cordierite	Expandable spheres	11–72	<40	–	[108]
Cordierite-bonded SiC	petroleum coke (PC)	30.1–71.7	6–50	Filter	[109]
HA	Silk	62.9 \pm 2.7	<20	Bone replacement	[93]
LaC ₂	Nylon6,6/Polypropylene	42.9–55.3/ 38–51.7	–	–	[110]
LaOC	PMMA microbeads	64.8–88.9	10	–	[111]
Ni-BCY	Gelled starch	36–49	0.2/1	Protonic ceramic fuel cell applications	[112]
Samarium-doped cerium (SDC)	NiO	–	–	–	[105]
Si ₃ N ₄	Epoxy resin (EP) particles	71–77	50–200	–	[98]
Si ₃ N ₄ -BN-SiO ₂	Core starch	14–79.9	–	–	[113]
Si-B-C-N	Metroxylon sagu	69	50–150	Both closed and open cells	[94]
SiC	Expandable microspheres	77–94	12.9 \pm 4.1/ 13.8 \pm 4.8	–	[114]
SiC	Polymer microbeads (~20 μm)	–	10–30	–	[115]
SiC	Graphite flakes	55.5–76.1	–	Meso-pores in the skeleton, interconnected flakelike micro-pores	[116]
SiC	Silica sphere	–	0.085–0.660	–	[117]
SiC	Poly microbeads (~8 μm)/Expandable microspheres (~13 μm /~20 μm)	35–95	–	–	[36]
SiC	Polystyrene (PS) spheres (1.1 μm /3.2 μm /10 μm)	74	0.75/2.2/7.2	Catalyst support	[118]
SiC	Hollow microsphere (diameters 15–25 μm)	44–77	0.003–30	–	[119]
SiC	PMMA microbeads (diameter 5 μm)	76.1–80.7	–	–	[96]
SiC	Polymer microbeads (~20 μm)	60–95	–	–	[120]
SiC	Silica	–	0.084–0.658	–	[121]
SiC	NaCl	30–58	125 (average)	–	[122]
SiC	Polymer microbeads	32–64	–	–	[123]
SiC	Butoxylated silica nanoparticles	72.9–80.0	0.011	Catalytic support	[61]
SiC	Starch	34.2–48.1	–	–	[124]
SiCN	Polyethylene microbeads (~10 μm)	35.6–48.0	7–8	Separation, catalysis	[125]
SiCN	Silica spheres (112–650 nm)	–	0.098–0.578	–	[126]
SiCN	UHMW-PE	41.6–43.2	1.6–2.0	Membrane and catalysis support	[104]
Si-C-N	Polydivinylbenzene (PDVB) microspheres	–	–	–	[127]
SiOC	Layered double-hydroxide	–	10–30 (hollow spheres)	Catalyst support	[128]
Ti ₂ AlC	NaCl powders (45–90 μm /180–250 μm /355–500 μm)	10–71	42–83/77–276/ 167–545	–	[129]
YSZ	Tert-butyl alcohol (TBA)	86.6–90	30.2	High-temperature thermal insulation applications	[130]
β -TCP	Polyethylene beads	71	0–10/10–30/ 100–300	–	[95]

content should be optimised. Badarulzaman et al. reported different paper fibre contents (2, 4, 6, 8, 10 wt.%) as the sacrificial template, and they showed that increased paper fibre content created higher porosity (from 0.09 % to 0.33 %), larger pore size in the porous ceramics [131]. However, higher porosity was accompanied with the formation of voids, fragility, shrinkage and deformation of the original material. They have concluded that 6 wt.% of paper fibre were optimum for preserving the original shape of specimen.

The quality of the porous ceramics including their properties and potential applications is determined by the type of template, since the pore morphology is controlled by the architecture of the incorporated porogen. Corradetti et al. prepared a porous lanthanum carbide disk with interconnected channels for permeation purpose [110], using up to 21.3 Vol% Nylon (NY) 6,6 and 24.8 vol% polypropylene (PP) with average length of 500 μm and diameters of 18 and 20 μm , respectively (Fig. 20a,b). They claimed that the Darcian permeability coefficient and non-Darcian coefficient were increased for 50 times and 1200 times respectively ($k_1 = 6.48 \times 10^{-14} \text{ m}^2$ and $k_2 = 3.6 \times 10^{-9} \text{ m}^2$), in comparison with the permeability level of the products without fibres. This was due to the interconnected networks in the radial direction. Fibrous fillers are thus more effective than spherical template porogens. In fact, these Nylon 6,6 and polypropylene fibres achieved similar permeability level to the spherical pore forming porogens, such as PMMA beads (Fig. 20c, d), whilst the latter demanded a very high addition of 60.6 Vol% which

led to poor mechanical properties, as a consequence.

A combination of preceramic polymer precursor and sacrificial templates is a common approach for the fabrication of advanced porous crystalline ceramics, such as SiC [132,121,123], SiCN [127], and SiOC [133]. Owing to the use of polymer precursor, this method can provide high flexibilities in the shaping options, and a range of shapes from monolithic materials to fibres or coatings can be created. Furthermore, low thermal treatment is required which is another major advantage of this route. The combined effect of ceramisation of the precursor and decomposition of the template at low temperatures contributes to the final high quality porous ceramic structures. The preceramic polymers provide a strong skeletal structure and suffer from little shrinkage upon sintering. Wang et al. fabricated macroporous SiC by using SiO₂ spheres as the sacrificial template (Fig. 21a) [117]. The SiO₂ spheres were firstly synthesised via a sol-gel reaction, which were closely packed by natural sedimentation to form the template. The template was then infiltrated with PMS solution, which was transferred to SiC during high temperature treatment up to 1400 °C. They also suggested a possible reaction mechanism following Eq. 4:



As summarised in Table 9, after etching with HF to remove the SiO₂, 3D ordered macroporous SiC with different pore sizes (84–658 nm), BET surface areas (299.44–584.64 $\text{m}^2 \text{g}^{-1}$), and micropore volumes

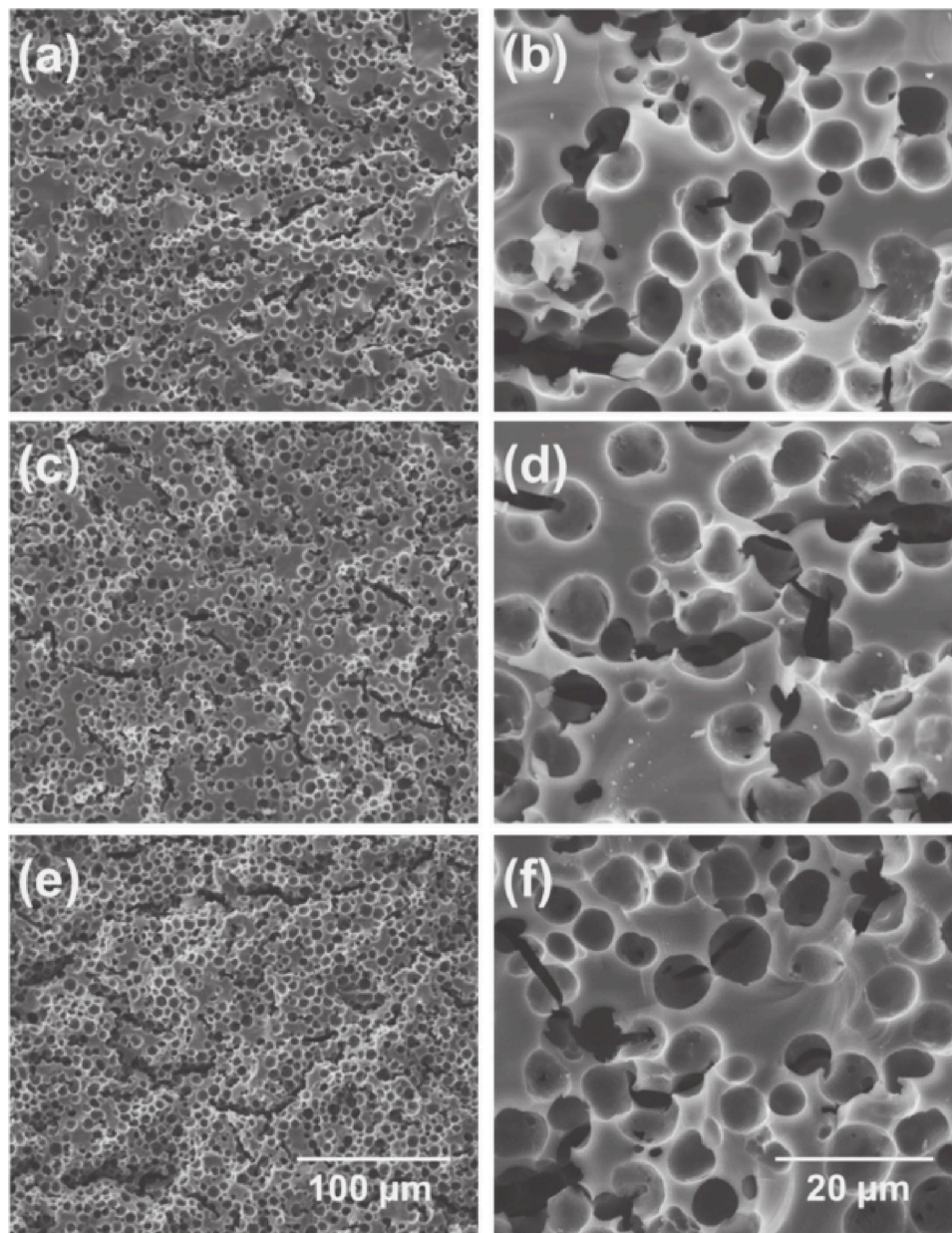


Fig. 19. SEM images of as-obtained tubular Si-C-N-based specimens subjected to heating at 800 °C for 4 h with initial PE microbeads porogen contents of (a, b) 25 %, (c, d) 30 %, and (e, f) 35 %. Reproduced with permission [125]. Copyright 2016, The Ceramic Society of Japan.

(0.25–0.64 cm³ g⁻¹) was obtained by simply choosing different SiO₂ sizes. The wall-thickness, however, was dependent on the packing degree of the sphere templates. As shown in Fig. 21(b–e), regular pores with uniform size and homogeneous walls are orderly distributed, and the wall thickness ranging from 10 to 85 nm depends on the packing

Table 8

The effects of template content on the density, porosity, and pore size of specimens. Reproduced with permission [125]. Copyright 2016, The Ceramic Society of Japan.

Template content (vol.%)	Bulk density (g cm ⁻³)	Total porosity (%)	Average pore opening radius (μm)
25.0	1.31 ± 0.03	35.6 ± 0.7	1.1
27.5	1.26 ± 0.01	38.3 ± 0.4	–
30.0	1.18 ± 0.01	42.0 ± 0.5	1.1
32.8	1.10 ± 0.04	46.1 ± 1.5	–
35.0	1.06 ± 0.01	48.0 ± 0.6	0.8

degree of templates and the properties of precursor solution. They also reported that the concentration of the templates should be high enough, no lower than 8%, otherwise broken walls would result due to poor resistance to contraction stress during pyrolysis, although a too high concentration over 80 % would severely degrade the infiltration performance. This technique was also adopted for similar preparation of macroporous SiCN ceramics under N₂ atmosphere, and generated pore size of 98–578 nm, BET surface area of 250–455 m² g⁻¹, and pore volume in the range of 0.16–0.31 cm³ g⁻¹ [126].

Furthermore, advanced hierarchical silicon oxycarbide (SiOC) ceramics with high surface area of 531 to 1311 cm² g⁻¹, large pore volumes from 0.47 to 1.20 cm³ g⁻¹ were reported by Yan et al. [133] using a mixture of allyl hydridopolycarbosilane (AHPCS) and hydridopolycarbosilane (HPCS) as pre-ceramic polymer precursors, surfactant sodium dodecylbenzenesulfonate (SDBS) modified Layered double hydroxides (LHDs) as the sacrificial template, which was extracted by acid leaching. The resulting materials exhibited pore spaces with

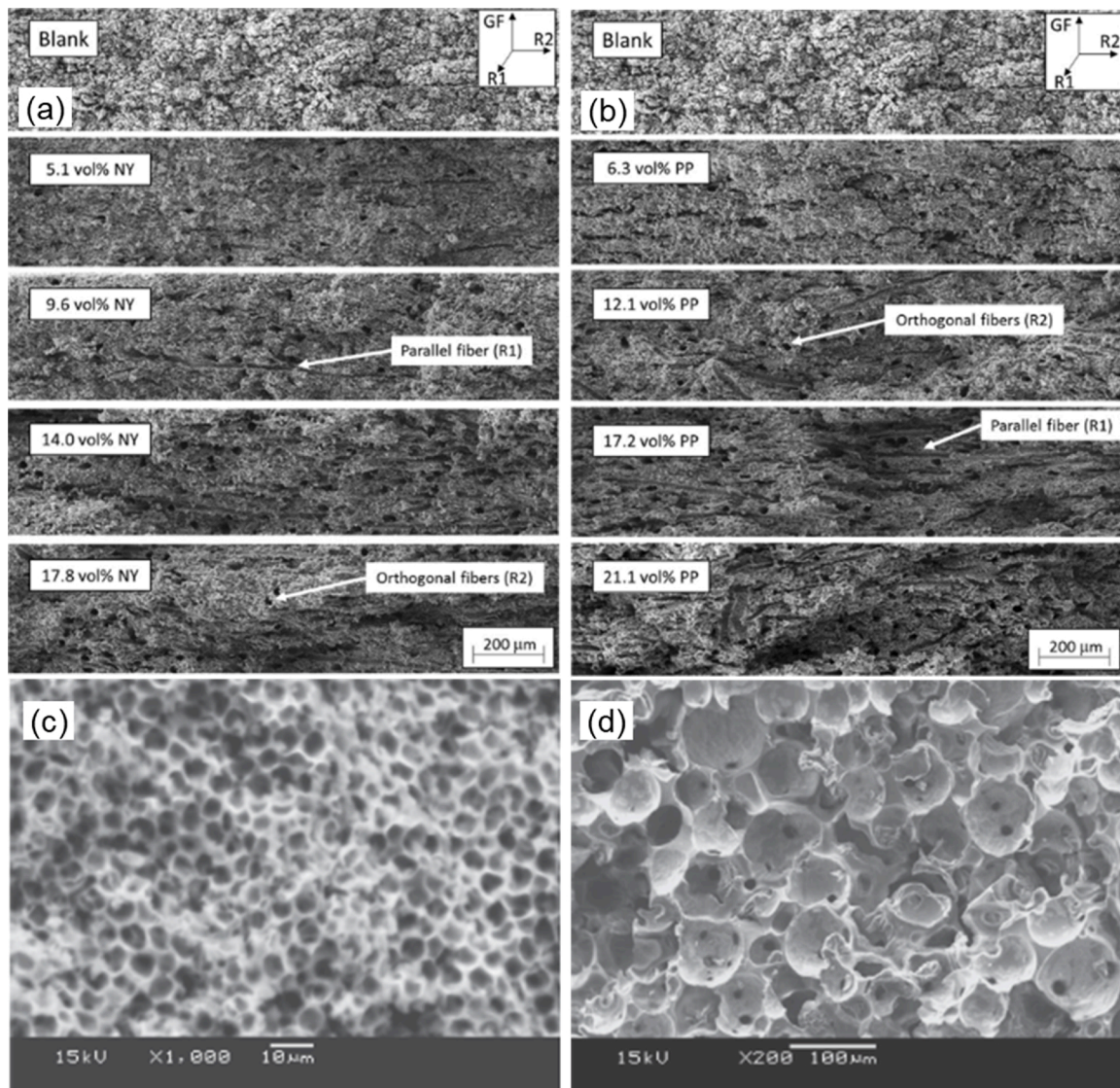


Fig. 20. (a, b) SEM images of the LaC_2 derived from different fractions of nylon and PP fibres acting as the sacrificial template. Reproduced with permission [110]. Copyright 2016, Elsevier B.V. (c, d) SEM micrographs of porous SiC using spherical PMMA as the sacrificial template. Reproduced with permission [132]. Copyright 2011, The Ceramic Society of Japan.

desirable structures.

It can be concluded that the non-liquid based sacrificial template approach gives rise to a direct management of the porosity, pore dimension and consequently a certain level of control over the mechanical properties and permeability. The surface area, porosity and structure of resultant porous ceramics largely depends on the selection of template, precursor and the ratio between them [133]. A well-defined porous structure can be obtained by uniformly distributing the porogen within the precursor, a tightly controlled precursor/porogen ratio and porogen decomposition routine would result in efficient crack suppression and good dimensional stability [125,132].

2.3.2. Liquid template - freeze casting

For sacrificial template method, the mismatch in thermal expansion coefficient between different phases can induce cracks within the structure during the following up pyrolysis or sintering stage. These drawbacks can be overcome by employing aqueous pore formers which can be easily sublimated [2]. Freeze-casting is a form of sacrificial template method that uses frozen liquid as templates to generate pores [134]. In this process, ceramic suspensions undergo a directional cooling process, which is a key operation that allows for the frozen suspension

subsequently removed by directional sublimation, so that generating macroporous ceramics with unidirectionally aligned pores [135]. Porous ceramics with high porosity (>50 %) and vertically aligned hierarchical pores fabricated by this method are suitable for thermal insulators [136,137], absorbers [138], and energy harvesting applications [139].

Porous ceramics fabricated via freeze-casting method with their preparation conditions and resulting microstructural features have been summarised in Table 10.

Deville has summarised the principles of freeze-casting of porous ceramics [164]. The freeze-casting process can be divided into four steps (Fig. 22): slurry preparation, solidification of slurry, sublimation of the fugitive second phase, and sintering of the remaining ceramics. The slurry generally comprises three components: ceramic powder, solvent, and additives. To prepare a slurry of high quality, the solid loading should be carefully controlled based on the targeted porosity. It is worth noting that the collapse of green body may happen during the sublimation stage in the absence of binder, therefore proper binder additives should be used to maintain the structural integrity of the porous ceramics. In the solidification stage, the suspension undergoes a directional cooling, a natural segregation phenomenon occurs as ceramic

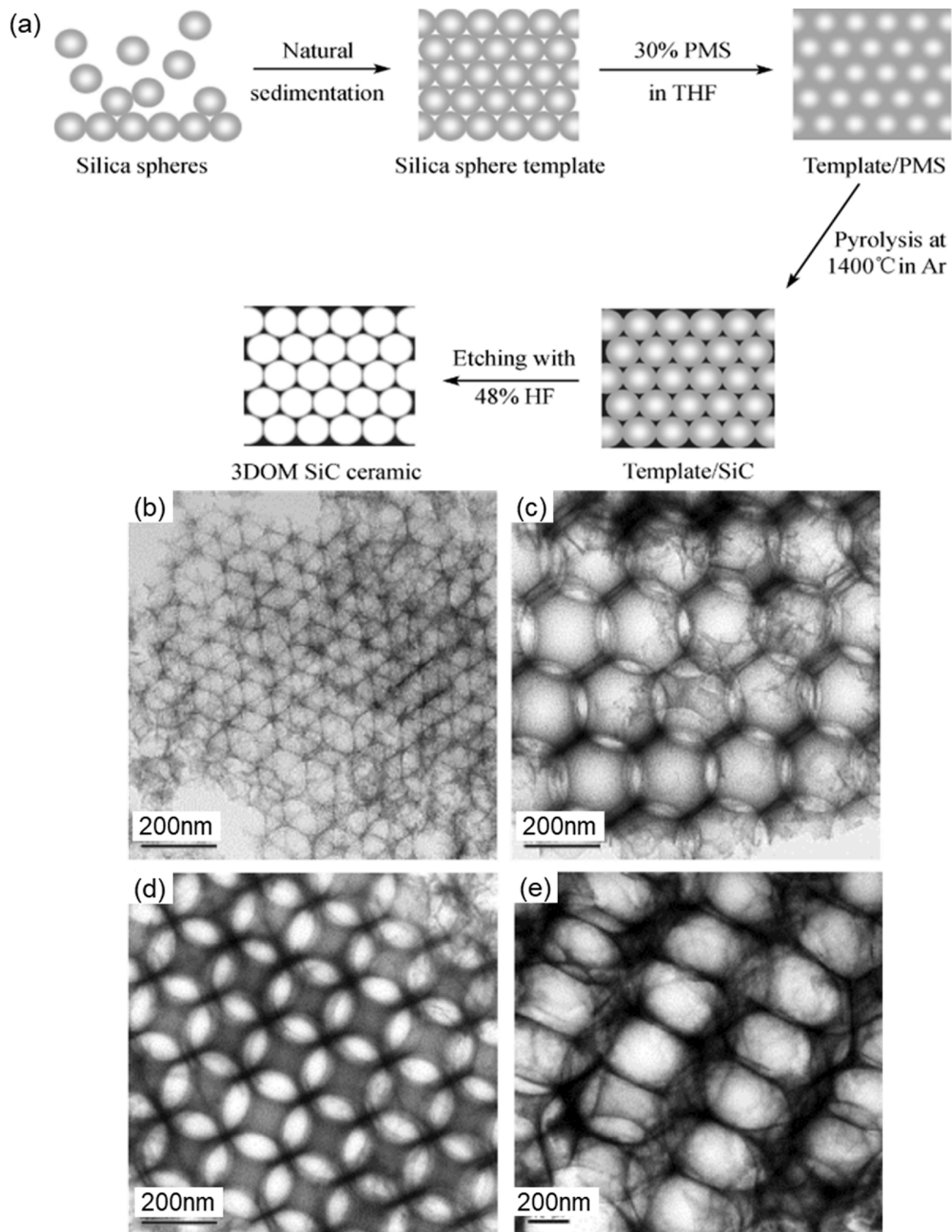


Fig. 21. (a) Schematic showing the fabrication steps used to produce 3D ordered macroporous SiC from sacrificial templates of self-close-packed SiO₂. Representative TEM images of 3DOM SiC ceramics with different pore sizes and planes: (b) 135 nm, [111] plane; (c) 220 nm, [110] plane; (d) 220 nm, [100] plane; (e) 660 nm, [211] plane. Reproduced with permission [117]. Copyright 2006, Springer Nature Switzerland AG.

particles within the slurry are rejected by the growing solidification front to form ceramic walls. When water is used as the solvent, the ice front grows 10^2 to 10^3 times faster along a-axis than along the c-axis, since the preferred ice growth direction is parallel to the temperature gradient. The cooling conditions of this process including cooling rate and temperature gradient largely dictate the microstructure of the final product, which is also dependent on the type of solvent used. Following

the solidification stage, the fugitive solvent is transferred to the gas state by vaporisation/sublimation and then removed, leaving behind the final porous structure. Eventually, sintering is carried out and the porosity created by solvent is preserved.

The microstructures and properties of the final products are largely dependent on the formulation of slurry, solidification conditions, and the choice of additives and solvent. These factors should be carefully

Table 9

The pore characteristics of 3D ordered microporous (3DOM) SiC ceramics derived from templates with different SiO₂ sizes. Reproduced with permission [117]. Copyright 2006, Springer Nature Switzerland AG.

Diameter of the SiO ₂ spheres (nm)	Pore size of the porous SiC ceramics (nm)	BET surface area (m ² g ⁻¹)	Micropore volume (cm ³ g ⁻¹)	Wall thickness (nm)
112	85	584.64	0.68	15 ± 6
192	135	457.28	0.46	25 ± 12
300	220	387.05	0.35	30 ± 15
500	475	362.32	0.26	30 ± 15
700	660	299.42	0.25	60 ± 35

controlled for obtaining materials with desired characteristics. These parameters are interlinked, and their influence on the final products is complex, but can be tuned for obtaining ceramics with specific pore structures [164,165].

The initial level of solid loading played a primary role in the resulting porosity of the scaffolds [148]. By increasing the initial solid loading, a reduction of porosity in the porous ceramics and the suppression of pore shrinkage can be achieved [154]. Liu et al. fabricated a porous Al₂O₃-ZrO₂ with different initial solid loadings by freeze casting [144]. With the increase of initial solid loading from 40 wt.% to 80 wt.% (Fig. 23a-e), the porosity of the as-obtained materials decreased from 74 % to 19 %, as the gaps between ceramic walls were filled; whilst the average ceramic wall thickness increased from ~ 4 to 17 μm when the initial solid loading reached 70 wt.% and no visible porosity can be found when this value reached 80 wt.%. Zhang et al. prepared porous Yb₂SiO₅ ceramics [157], and by increasing the solid content from 10 to 25 vol%, they have reduced the porosity from 72 % to 52 %. They also found that the pores evolved from dendritic to 3D reticular shapes with the formation of strong sintering necks. As a result, they reported that the compressive strength of the product increased from 2.82 to 7.01 MPa; whilst the thermal conductivity increased from 0.113 to 0.301 Wm⁻¹K⁻¹, which correlated very well with the porosity values, i.e. samples with lower porosity exhibited higher mechanical strength and thermal conductivity. Additionally, the dielectric constant of Yb₂SiO₅ which is known to be strongly influenced by the porosity were also improved from 1.81 to 3.59 [157].

Freezing velocities also have an influence on the porosity. Generally, the slower the cooling rate, the larger the solvent crystals [166]. Sadeghpour et al. prepared nanostructured Baghdadite (Ca₃ZrSi₂O₉)-based scaffold using freeze-casting [148], and investigated the influence of cooling rate on the pore sizes and mechanical properties of scaffolds. They reported that when the cooling rate was raised from 1 to 4 °C min⁻¹, the strength of the scaffolds increased nearly twice, as a result of the smaller lamellar spacing due to the faster cooling rate used (Fig. 24a,b). It is obvious that the overall areas of the wall cross-connections are responsible for the mechanical properties of porous ceramics, rather than the scale of the porous structure. Therefore, porous structures generated at lower freezing rate had fewer cross-connections, walls broke individually and gave rise to the poor mechanical performance, as reported [167]. However, when the velocity is above a critical value, particles cannot be ejected by the escaping gases and the engulfment phenomenon would occur, the microstructural features can no longer be easily tuned. Typically, in a ceramic-ice two-phase system, ceramic particles with smaller sizes would obtain an accelerated ejection speed by the moving ice front, which would mostly concentrate on the ceramic walls that were further away from ice crystals; whilst larger particles would locate closer to ice crystals. Therefore, slurries containing larger particles or slurries with high viscosity have relatively low critical velocity of the cooling front during solidification [168].

The growth of ice crystals during freeze casting, the porosity, pore morphology and hence the mechanical strength of materials can be

modified by using additives such as organics (gelatine) [169], oxides (Al₂O₃-MgO) [170], in the water based slurries [147]. Zavareh et al. fabricated porous LiFePO₄/C cathodes for Li-ion batteries [171], and they found that materials fabricated without additives exhibited an irregular pore structure (Fig. 25a). When using modified butadiene-styrene copolymer (WSB) and sodium silicate (Na₂O: 7.80–8.50 %, SiO₂: 25.80–28.50 %) as the additive, they found dendrites (Fig. 25b,c). The formation of lamellar structures can be obtained by using gelatine as freezing additives, since the gelatine inhibits the growth of ice dendrites, allowing the specimen with well-defined lamellar pore structure (Fig. 25d). A further increase of both gelatine and solid content even leads to the formation of cellular pore structure with honeycomb-like morphology [171]. By contrast, lamellar structure can be transformed to dendrite-like structures by adding PVA into the slurry as the binder [140]. The addition of PVA increased the viscosity of ceramic slurry, as a result hindering the rearrangement of the ceramic particle to form unidirectional ice growth during water solidification. Wang et al. further tested the PVA as an additive in the fabrication of porous SiC, and they reported that by increasing the content of PVA, the growth of ice crystal was inhibited and lamellar pores became more irregular [152].

Although the water-based freeze-casting is the mainstream approach, it has been found that solidification of different solvents could generate different types of morphology. When water was used as the solvent, lamellar microstructures were formed. However, the solidification of liquid camphene led to the formation of clearly defined dendrites, while prismatic channels could be obtained when tert-butyl alcohol was used as the solvent (Fig. 26a,b) [159,164]. Although the fabrication of porous ceramics with lamellar microstructure by water-based freeze casting is more cost-effective and environmentally friendly [155], tert-butyl alcohol (TBA) can be frozen at around 25 °C and rapidly sublimated [160], which gives rise to relatively straight prismatic pores that provides effective diffusion pathways for gas permeation and the right pore size for high piezoelectric coefficients [161]. In addition, hydrogenated vegetable oil (HVO) has been used as the pore former for the preparation of macroporous ceramics, since the HVO can be dried in open air atmosphere and generates cells with spherical to polygonal shapes [135], and the pore sizes can be easily increased with higher concentration of the emulsifying agent and larger oil to alumina volume ratios. This process offers a cost-effective and eco-friendly approach for easy pore control.

Functional requirements necessitate more complexed porous structures in ceramics, which promoted research in the manipulation of pore orientation and morphology. Freeze-casting could provide a high degree of flexibility for controlling the morphology and hence the properties of samples by simply changing the slurry characteristics, initial solid loading, and temperature gradients during freeze casting [138]. Moreover, multiple cold sources or multiple external fields could be applied to manipulate the growth behaviour of ice crystals. An epitaxy technique that placing a mould filled with pure solvent on a cold finger was developed by Munch et al. [172], which provided a new mean to manipulate the structure of lamellae. Tang et al. further created porous alumina with axisymmetric structure by using a combination of directional solidification with multiple cold sources [142], both electric and magnetic fields (Fig. 27a-c), and they found the isotropy of the structures was improved and the mechanical properties was enhanced correspondingly.

It can be deduced that by controlling the solid loading of initial slurries, freezing conditions, additives, and solvent type, freeze-casting provides a precise control over the uniquely ordered microstructure of porous ceramics, better off other pore forming strategies. The microstructural features, mechanical properties, and functional properties of the freeze-cast porous ceramics have been intensively studied and summarised. However, little attention has been paid to the sublimation of frozen template, which could take up to 100 h and is responsible for the collapse of the structure. Moreover, the cryogenic energy

Table 10

A summary of materials fabricated by freeze casting: the template, porosity, pore size, and applications.

Materials	Solvent	Solid loading	Freezing conditions	Additive	Porosity (%)	Pore size (μm)	Refs
Al_2O_3	Water	23.5 vol.%	Freezing temperature: -50°C Holding time: 5 h	Dispersant: Sodium-hexametaphosphate (SHMP) Binder: Polyvinyl alcohol (PVA)	64.5–68.5	0.48–2/10–14 (bimodal)	[140]
Al_2O_3	Water	10–40 vol.%	Freezing temperature: -100°C Cooling velocity: $1-20^\circ\text{Cmin}^{-1}$	Dispersant: Ammonium polyacrylate Binder: Polyvinyl alcohol (PVA) Hardener: 3,3'-diaminodipropylamine Dispersant: Polyacrylate sodium	37.4–56.2	12–49 (ceramic wall thickness: 4–26)	[141]
Al_2O_3	Water	30 vol.%	Freezing temperature: -30°C	Binder: Carboxymethyl cellulose Surfactant: Ethoxylated acetylenic diol	49.8–51.1	–	[142]
$\text{Al}_2\text{O}_3\text{-ZrO}_2$	Water	25–30 vol.%	Freezing temperature: $<0^\circ\text{C}$	Binder: Polyvinyl alcohol (PVA) Space holder: Aspecial wax, cornstarch powder Dispersant: Duramax D3021	43.4–68	–	[143]
$\text{Al}_2\text{O}_3\text{-ZrO}_2$	Water	40–70 wt.%	–	Binder: Duramax B-1000, B-1007 Dispersant: Ammonium polyacrylate	35–74	–	[144]
BaTiO_3	Water	20–45 vol.%	–	Binder: Acrylic polymer emulsion	22–60	–	[145]
BaTiO_3	Water	17.5 vol.%	–	–	65 ± 1.4	0.3/30	[146]
Biphasic calcium phosphate (BCP)	Water	30 wt.%	Freezing temperature: -10°C	Binder: Sodium alginate	60.22–77.76	74.37–111.27	[147]
$\text{Ca}_3\text{ZrSi}_2\text{O}_9$	water	12.5–20 vol.%	Freezing temperature: -45°C Cooling velocity: $1/4^\circ\text{Cmin}^{-1}$	Dispersant: Dolapix P62 Binder: Polyvinyl alcohol	58.22–64.27	–	[148]
$\text{Ni}_{0.5}\text{Ti}_{0.5}\text{NbO}_4$	Water	40 vol.%	Freezing temperature: $-40/-70/-196^\circ\text{C}$ Holding time: 15 min	Dispersant: Polyacrylic acid Binder: Polyvinyl alcohol Dispersant: Ammonium polyacrylate	51.03–61.28	–	[149]
PZT	Water	–	–	Binder: Polyvinyl alcohol	25–45	3–30	[150]
Si_3N_4	Water	15–25 vol.%	Freezing temperature: -70 to -50°C Freezing temperature: -20°C	Dispersant: Ammonium polymethacrylate anionic Dispersant: Tetramethylammonium hydroxide Binder: Polyvinyl alcohol	66.4–76.8	–	[151]
SiC	Water	50 wt.%	Holding time: 4 h	–	66.46–71.68	0.42/2.49/7/19/216	[152]
SiC	Water	1.5–7 vol%	Cooling velocity: 15°Cmin^{-1}	Stabiliser: Chitosan	92–98	15–50 (interlayer spacing)	[153]
TiO_2	Water	10–30 vol.%	Freezing temperature: -50°C	Sodium hexametaphosphate Dispersant: Ammonium polymethacrylate anionic Binder: Polyvinyl alcohol Others: Glycerol	–	Diameter of pore 6–8/15–20 (Lamellar spacing 1.5–6.5 Lamellar thickness 15–30)	[154]
Y_2SiO_5	Water	15–30 vol.%	Freezing temperature: -55°C	Dispersant: Ammonium polymethacrylate anionic Binder: Polyvinyl alcohol Others: Glycerol	52–72	10–40	[155]
Y_2SiO_5	Water	20 vol.%	–	Dispersant: Ammonium polymethacrylate anionic Others: Glycerol	62–71	25–50	[156]
Y_2SiO_5	Water	10–25 vol.%	–	Dispersant: Ammonium polymethacrylate anionic Binder: Polyvinyl alcohol Others: glycerol	71.2–85.7	0.2–1/10–30	[157]
Yb_2SiO_5	Water	15 vol.%	–	Dispersant: Ammonium polymethacrylate anionic Binder: Polyvinyl alcohol Others: Glycerol	82–86	0.3–50	[158]
ZrB_2	Water	35–48 vol.%	Freezing temperature: -40°C Freezing temperature: 5°C	Dispersant: Ammonium polyacrylates Dispersant: Ammonium polyacrylates	49–57	1–2/20–30	[138]
Al_2O_3	Hydrogenated vegetable oil	30 vol.%	Holding time: 30 min	Emulsifying agent: Sodium dodecyl sulphate Gelling agent: Carrageenan	70.7–84	3.6–13.24	[135]
Al_2O_3	TBA	25 vol.%	–	Dispersant: Citric acid	58 ± 3	–	[159]

(continued on next page)

Table 10 (continued)

Materials	Solvent	Solid loading	Freezing conditions	Additive	Porosity (%)	Pore size (μm)	Refs
Alkali niobate-based (NKN) Binder: Polyvinyl butyral	TBA	–	Freezing temperature: 0 °C Holding time: 1 h [160]	Freezing temperature: -40 °C	Dispersant: Floren G700	Open 29–74	–
PZT	TBA	15–40 vol%	Freezing temperature: -10/-25/-40/-60/-78/-100 °C	Dispersant: Acacia Binder: Polyvinyl butyral	–	0.01–0.1	[161]
PZT	TBA	15–40 vol.%	Freezing temperature: -30 °C	Dispersant: Acacia Binder: Polyvinyl butyral	28.1–68.7	–	[162]
Silicate cement	TBA	40–60 wt.%	Freezing temperature: -10 to -80 °C Holding time: 30 min	Ethyl cellulose ethocel, Polyvinylpyrrolidone	56.67–72.22	2.05–17.28 (peak distribution)	[163]

consumption and vacuum conditions as the basic requirement of the method not only result in high cost, but also restrict the possibility for mass amount production [173]. In this regard, efforts should be made to reduce the cost and improve the easiness of manufacturing.

2.4. Direct foaming

In direct foaming technique, a pre-ceramic suspension containing surfactant as the starting material is foamed via a gas incorporation

(mechanical stirring or chemical blowing), followed by the stabilisation and sintering processes, both open- and close-pored structures with porosities up to 97 % can be obtained by this simple, low-cost, and fast processing approach [174–176]. Meanwhile, the possibility of mass production is another advantage.

The most critical issue in direct foaming is the stabilisation of air bubbles incorporated into the suspension, particularly when the slurry contains a high content of bubbles the wet foam is prone to collapse and crack [173]. Short-chain amphiphilic molecules as a surfactant has been

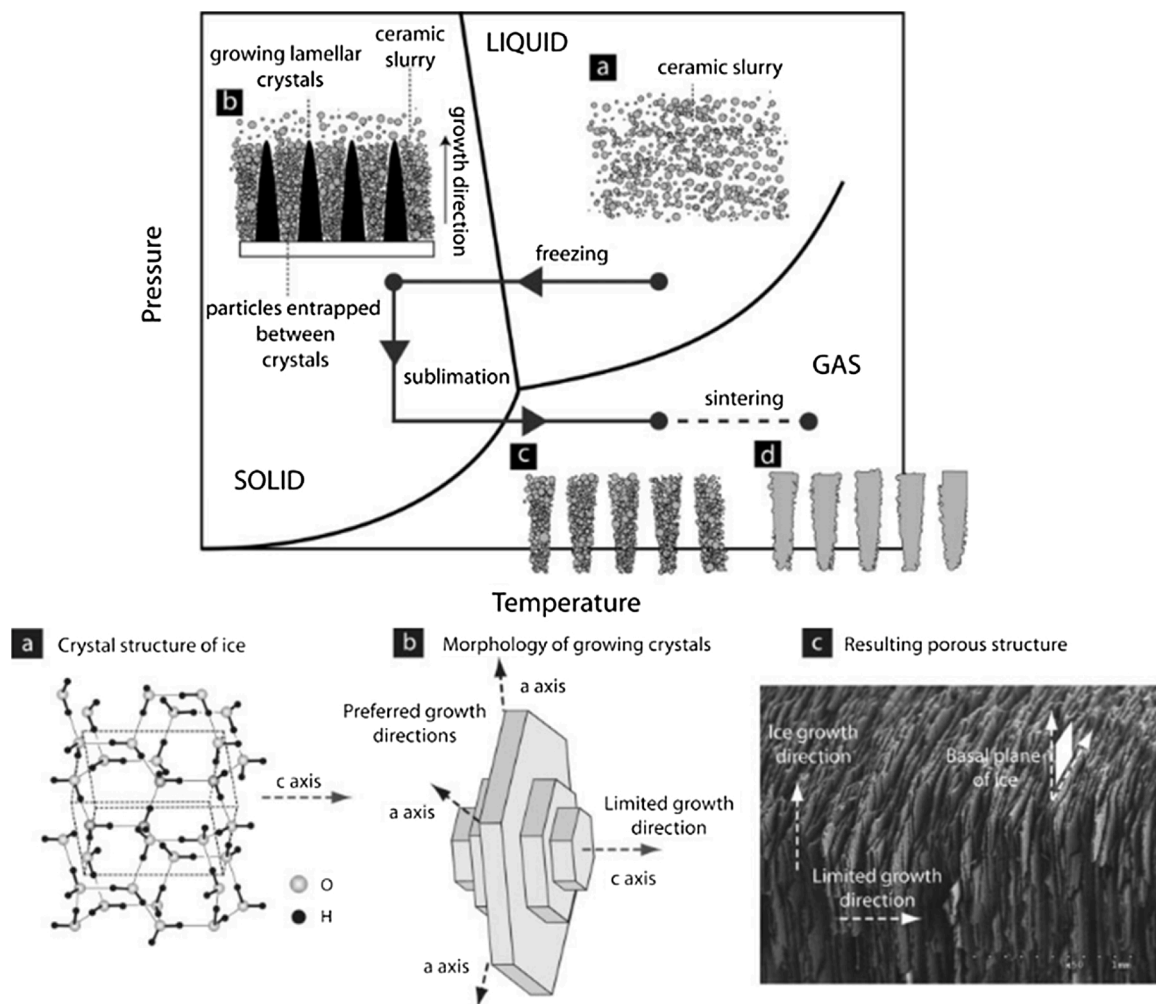


Fig. 22. A drawing (top picture) to show the solvent phase changes involved in the four stages during a freeze-casting process; which are: slurry preparation, solidification, sublimation, and sintering; and an illustration of using ice as the solvent (bottom drawing) to show the crystal structure of ice (a), morphology of growing crystals (b), and resulting porous structures (c). Reproduced with permission [164]. Copyright 2008, John Wiley & Sons, Inc.

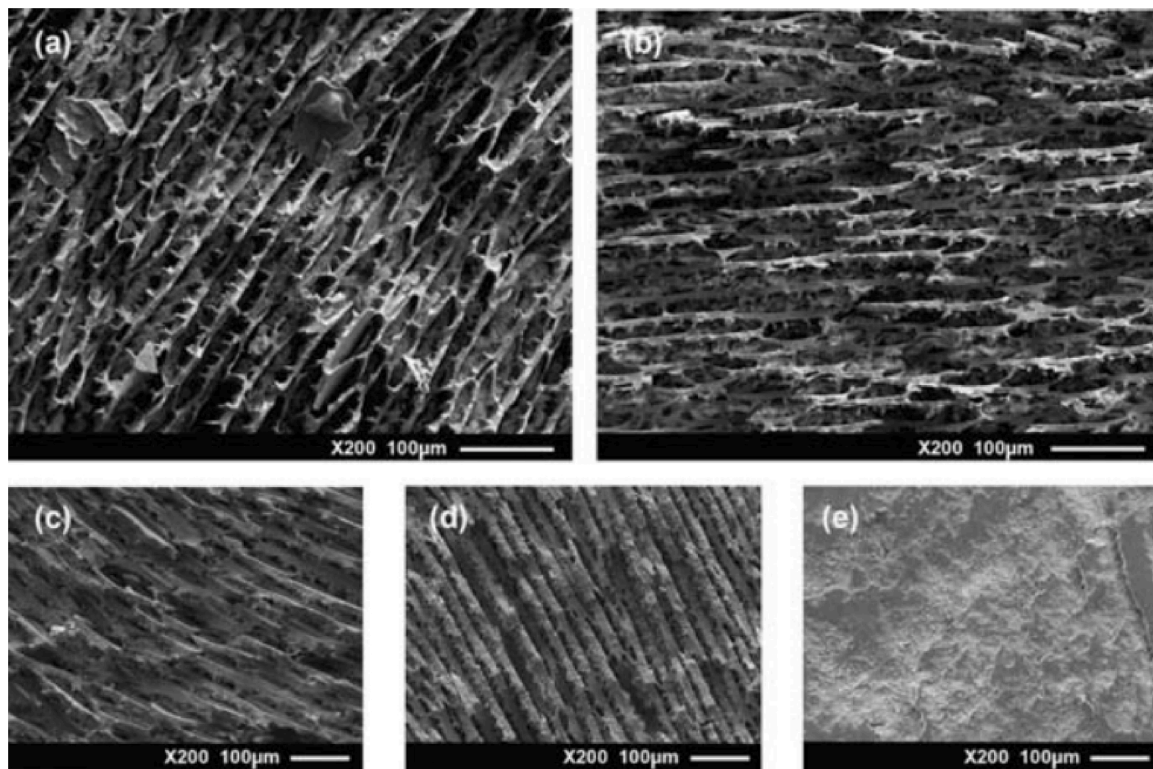


Fig. 23. SEM micrographs of the porous $\text{Al}_2\text{O}_3\text{-ZrO}_2$ fabricated from slurries with different initial solid loadings of: (a) 40 wt.%, (b) 50 wt.%, (c) 60 wt.%, (d) 70 wt.%, (e) 80 wt.%. Reproduced with permission [144]. Copyright 2010, Elsevier B.V.

added to impart hydrophobicity to the particle surface in a suitable pH range (Fig. 28), the surface modified partially hydrophobic particles absorbed at the gas/liquid interfaces impede the coalescence of bubbles, which enables the production of high volume stable foam and leads to the production of porous ceramics after drying/setting and sintering [177,178]. To form a stable suspension, the pH value, solid loading, and surfactant in the initial suspension should be well-controlled.

Ceramics fabricated using the direct foaming method, including their preparation conditions and resultant microstructural features, have been summarised in Table 11.

2.4.1. Foaming by mechanical agitation

The foaming of the suspension is mostly carried out at room temperature simply by mechanical frothing, despite that the injection of compressed air has also been reported [201]. Sarkar et al. used Al_2O_3 , TiO_2 and SiO_2 as the starting materials to prepare macroporous Al_2TiO_5 -mullite ceramics [177], and they directly incorporated air into the colloidal suspension by using a household hand mixer to create the pores. The products were finally obtained following subsequent drying and sintering procedures, as shown in Fig. 29.

They have found that the porosity of the resultant ceramics is proportional to the air content in the suspension after foaming, which is calculated as:

$$\text{Air content} = \frac{(V_{\text{wet foam}} - V_{\text{suspension}}) \times 100}{V_{\text{wet foam}}} \quad (5)$$

Where $V_{\text{wet foam}}$ and $V_{\text{suspension}}$ represent the volume of the suspension before and after the foaming process, respectively. However, the stability of the foam, as the most critical issue, requires partially hydrophobic particles to be attached on the surface of bubbles with a contact angle $\theta < 90^\circ$ (which readily occurs when θ is between 50 and 90°). The stability can be evaluated by the volume change of the wet foam subjected to drying in a cylindrical mould for:

$$\text{Foam stability} = \frac{V_{\text{Final}}}{V_{\text{Initial}}} \times 100 \quad (6)$$

Where V_{Final} is the volume of the foam after the drying procedure, while V_{Initial} indicates the volume of the wet foam when it is filled into the mould. The foam stability can also be measured by the free energy (ΔG)

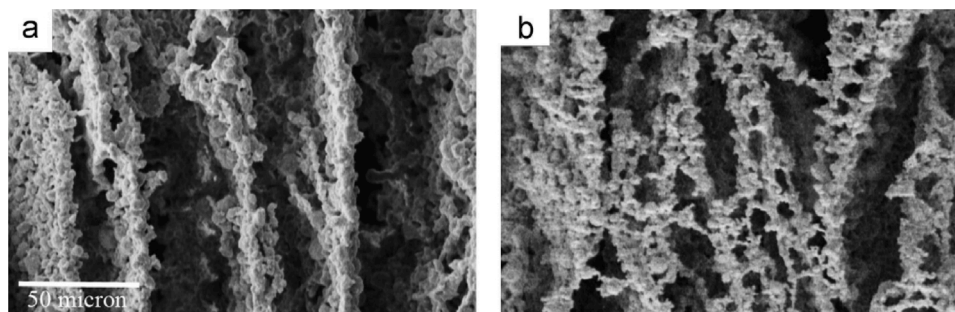


Fig. 24. SEM images of Baghdadite ($\text{Ca}_3\text{ZrSi}_2\text{O}_9$)-based scaffold freeze-cast at cooling rate of 1°C min^{-1} and 4°C min^{-1} [148]. Copyright 2014, Elsevier B.V.

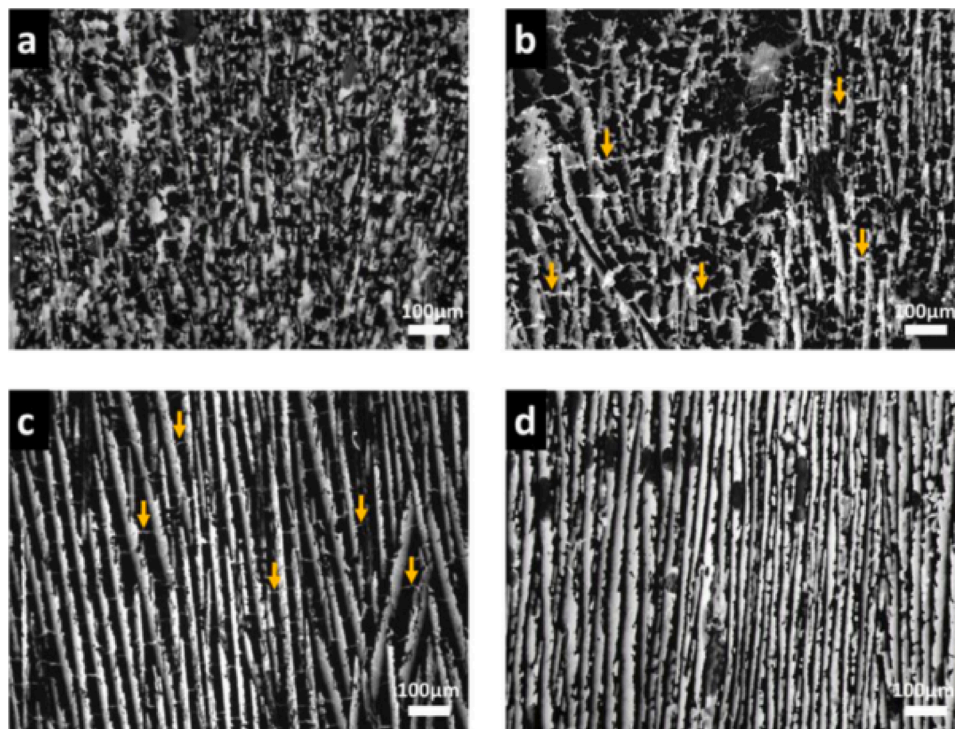


Fig. 25. UV optical micrographs of freeze-cast specimen fabricated (a) without binder, (b) with WSB, (c) with sodium silicate and (d) with gelatine. Arrows point to the dendrites. Reproduced with permission [171]. Copyright 2016, The Ceramic Society of Japan.

for the adsorption of a particle at the interface:

$$\Delta G = \pi r^2 \gamma_{\alpha\beta} (1 - \cos \theta)^2, \theta < 90^\circ \quad (7)$$

Where r is the radius of the particle, γ is the surface tension of the suspension, and θ is the contact angle. High adsorption free energy enables irreversible adsorptions of particles at the air-liquid interface and leads to outstanding stability. Additionally, they investigated the Laplace pressure (ΔP) that indicates the pressure difference between the inside and outside of a gas bubble, which is also considered as an important parameter of the foam stabilisation:

$$\Delta P = \gamma \left(\frac{1}{R_1} + \frac{1}{R_2} \right) = \frac{2\gamma}{R} \quad (8)$$

Where γ is the surface tension of the suspension, and R_1 and R_2 are the radii of two interfacing bubbles.

Bhaskar et al. prepared porous SiO₂-SiC ceramic by direct foaming and extensively investigated the influence of the composition of the initial suspension on the wet foam stability [194], which is reflected on the change of the contact angle, adsorption free energy, and Laplace pressure. With the increasing amount of SiC addition to the SiO₂ suspension, the contact angle changed as a result of different hydrophobisation degree, and the surface tension changed due to the increase of the particle concentration (Fig. 30a). By adjusting the solid content of the suspension, the adsorption free energy ($5.5 \times 10^8 - 7.0 \times 10^8$ kTs), Laplace pressure (1.15–1.9 mPa), air content (~57–67 %), pore size (~70 – 110 μm), and wet foam stability can all be tailored according to above equations (Fig. 30b-e). At the same time, they found that the relative bubble size increases with respect to the foaming time (Fig. 30f) [194].

Sciamanna et al. further studied the relationship between the microstructure of porous ceramics and the solid loading, surfactant

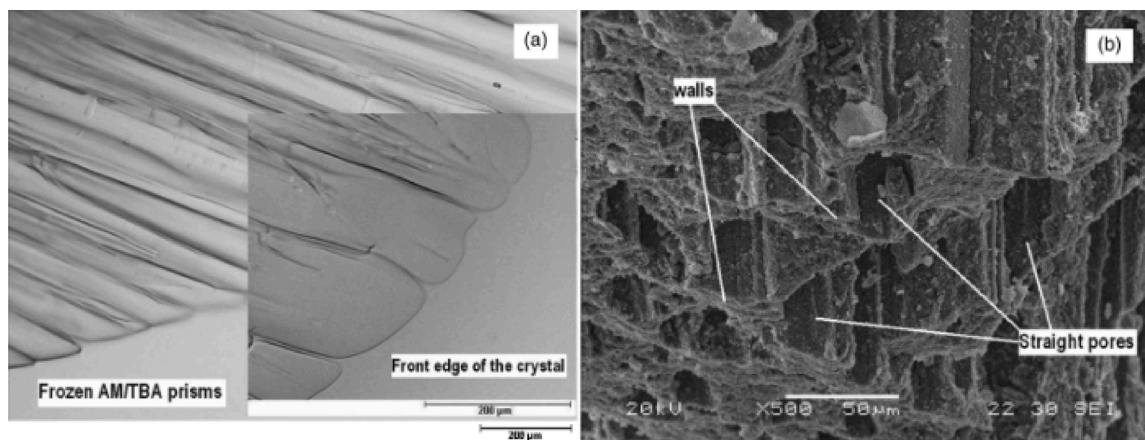


Fig. 26. The microstructure of pores formed using tert-butyl alcohol (TBA) as the solvent, depicting the pore formation mechanism. (a) The growth of TBA ice prisms, and (b) Pore channels. Reproduced with permission [159]. Copyright 2007, The American Ceramic Society.

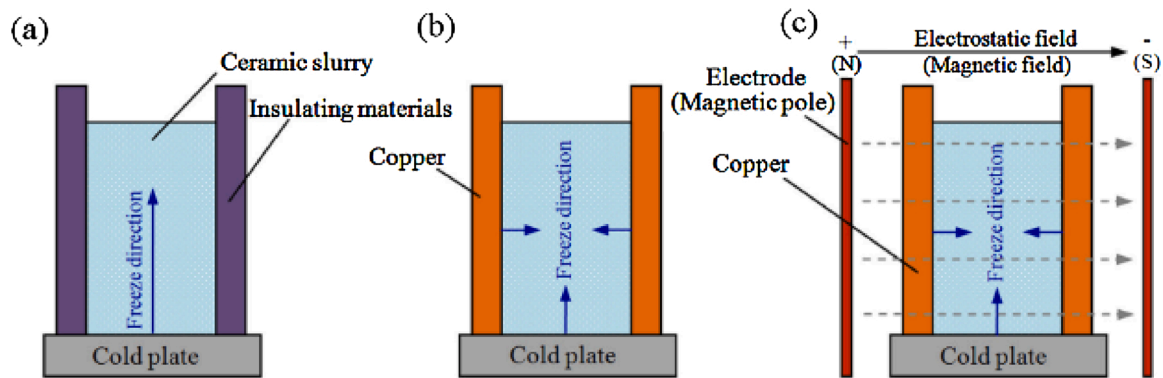


Fig. 27. Schematics of different freeze casting conditions: (a) Conventional single cold source; (b) Parallel dual cold sources; and (c) With applied electric and magnetic fields. Reproduced with permission [142]. Copyright 2016, Elsevier B.V.

contents, and stirring velocity during the foaming process [184]. Porous alumina ceramics were obtained by direct foaming of aqueous alumina suspensions, with butyric acid as a hydrophobisation agent for alumina particles. As shown in Fig. 31a, with the increase of alumina content from 25 to 40 vol%, the porosity dropped from 89 % to 65 %, while the corresponding pore size decreased from 140 μm to 60 μm . Meanwhile, increasing the content of butyric acid resulted in larger viscosity of the suspension (Fig. 31c), which made the incorporation of air more difficult, therefore the final porosity and pore size decreased (Fig. 31b). Additionally, they have found that by increasing the stirring velocity, the pore size was slightly decreased (Fig. 31d), however the porosity remained unchanged [184].

Apart from the composition and solid loading of initial suspension, the use of the surfactant greatly dictates the microstructure of the final product as well. The increase of the surfactant concentration favours the formability of the suspension [199]. However, high surfactant concentration resulted in over-flocculation by increasing the ionic strength of the medium, making the foaming procedure difficult [192]. Ahmad et al. prepared ZrO_2 foam through direct foaming and investigated the effect of valeric acid as the surfactant [198]. As shown in Fig. 32a, cells derived from 5 mmolL^{-1} valeric acid were irregular, whereas from higher concentrations of 30 and 50 mmolL^{-1} exhibited non-uniform cell-size and agglomeration (Fig. 32c,d). They further obtained an optimal foamability and stability of ZrO_2 using a valeric acid concentration of 10 mmolL^{-1} , documented a cell size ranging from 50 to 150 μm and porosity exceeding 90 % (Fig. 32b).

It can be envisaged that the foaming time could directly affect the porosity of the resulting foam, and Jana et al. verified such an effect by

establishing the relationship of foaming time against the relative density of SiC foams [192], as displayed in Fig. 33.

Therefore, for porous ceramics foamed by mechanical frothing, a good control of the composition, solid loading, and viscosity of the initial suspension, with the addition of a suitable amount of surfactant is the key to good formability and stability of the foam, leading to homogeneous pore distribution; whereas the stirring velocity has a negligible effect. However, the relationship between the mechanical stirring time and incorporated air content should be quantitatively established to unlock the true relationship and achieve precise pore size and volume control.

2.4.2. Foaming by chemical blowing

In addition to the above-mentioned physical foaming approaches, chemical blowing is another efficient foaming technique. In this approach, although a laboratory mixer is used for dispersion and homogenization of the suspension, pores are mostly generated by in-situ evolution of gases from the chemical reaction and/or thermal decomposition of a chemical blowing agent.

Barg et al. attempted to utilise alkane or air-alkane emulsified ceramic powder suspensions for cellular ceramics production, and this time-dependant autonomous foaming was generated by the evaporation of the emulsified alkane droplets (Fig. 34a,b) [176]. Due to the very fine nature of the emulsified droplets, a uniform distribution of the porosity could be achieved. Meanwhile, they studied the effect of anionic, cationic, and non-ionic surfactant and confirmed that the foaming process proceeded at the highest rate in the anionic surfactant-based system, which led to thinner struts, larger cell and window size than using

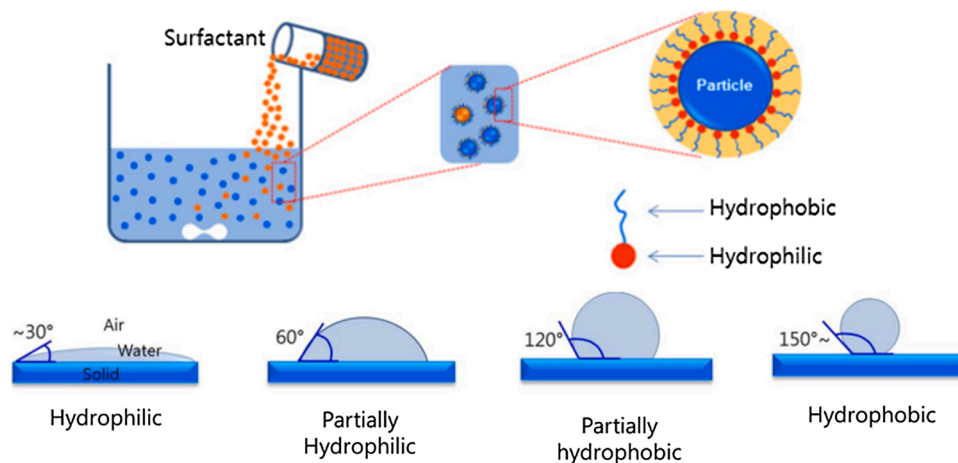


Fig. 28. Schematic of in-situ hydrophobisation of Al_2O_3 particle, illustrating the changes of the partial hydrophobisation of particles with varying contact angles of the initial suspension. Reproduced with permission [174]. Copyright 2013, The Korean Ceramic Society.

Table 11
Examples of porous ceramics fabricated by direct foaming.

Material	Foaming method	Additives	Porosity (%)	Pore size (μm)	Refs
Al(OH) ₃	Mechanical agitation	Surfactant: Sodium dodecyl sulfate Strengthening agent: Cement	86–93	69–140	[179]
Al(OH) ₃	Mechanical agitation	Surfactant: Sodium dodecyl sulfate Setting agent: Cement	88–92	50–180	[180]
Al ₂ O ₃	Mechanical agitation	Foaming agent: Carboxylic acids (Propionic acid/ Butyric acid/ Valeric acid/ Enanthic acid)	45–95	10–300	[181]
Al ₂ O ₃	Mechanical agitation	Surfactant: Valeric acid, Sodium dodecyl sulfate	85–95	17–140	[182]
Al ₂ O ₃	Mechanical agitation	Surfactant: Butyric acid, Propyl gallate Water-retention additive: Wheat starch	80.2–89	24–35	[183]
Al ₂ O ₃	Mechanical agitation	Surfactant: Butyric acid Surface modifier: Propyl gallate	25–89	20–140	[184]
Al ₂ O ₃	Mechanical agitation	Foam stabiliser: Cement Ca ₃ SiO ₅ Setting accelerator: Li ₂ CO ₃	40–65	100–1000	[185]
Al ₂ TiO ₅ -mullite	Mechanical agitation	Surfactant: Propyl gallate	–	51.78–410.71	[186]
Al ₂ TiO ₅ -ZrTiO ₄	Mechanical agitation	Surfactant: Propyl gallate	–	150–400	[187]
CaAl ₂ O ₄	Mechanical agitation	Surfactant: Propyl gallate Setting accelerator: Li ₂ CO ₃	76–86	170–460 (average)	[188]
Ceramic (kaolin-talc powder-Al ₂ O ₃)	Mechanical agitation	Foaming agent: Cattle hoof shell powder Curing agent: α -Ca ₃ (PO ₄) ₂ stabilising agent: Hydrophobic activated C	62.7–78.8	100–500	[173]
cordierite	Mechanical agitation	Foaming agent: Dodecyl sodium sulfate Dispersant: Gum Arabic Solidifying agent: Agar	87–90	190–230	[189]
Diatomite	Mechanical agitation	Foaming agent: Triethanolamine lauryl sulfate Dispersing and gelling agent: Isobutylene-maleic anhydride copolymer Foam stabilising agent: Sodium carboxymethyl cellulose	82.9–84.5	109.7–130.5	[190]
Mullite	Mechanical agitation	Foaming agent: Sodium lauryl sulfate Foam stabiliser: Aluminate cement Dispersant: (CH ₃) ₄ NOH	65.32–83.02	3.3–17.07	[191]
SiC	Mechanical agitation	Surfactant: Cethyltrimethylammonium bromide	56–88	100–1700	[192]
SiC/ CA ₆	Mechanical agitation (Ball milling)	Foaming agent: Triethanolamine dodecyl sulfate Dispersant: Tetramethylammonium hydroxide	67.2–82.9	30/ 200	[193]
SiO ₂	Mechanical agitation	Surfactant: Hexylamine Anionic surfactant: Ammonium decanoate	–	–	[194]
TiO ₂	Mechanical agitation	Cationic surfactant: Cetyldimethylethylammonium bromide Non-ionic surfactant: Triton X-100	Open porosity 72–88	<550	[195]
Y ₂ SiO ₅	Mechanical agitation	Foaming agent: Sodium dodecyl sulfate Dispersant: Ammonium citrate (AC) Gel former: Gelatin, polyethylene glycol	60.7–88.4	0.2–1/30–400	[196]
Y ₂ SiO ₅	Mechanical agitation	Foaming agent: Sodium dodecyl sulfate (SDS) Dispersant: Ammonium citrate (AC) Gel former: Gelatin, Polyethylene glycol	80.1–82.1	30–260/ 0.1–0.8	[197]
ZrO ₂	Mechanical agitation	Dispersing agent: HCl Surfactant: Valeric acid	>90	50–150	[198]
ZrO ₂	Mechanical agitation	Surfactant: Sodium dodecyl sulfate (SDS)	96–98	50–150	[199]
ZrTiO ₄ -TiO ₂	Mechanical agitation	Amphiphile: Propyl gallate	57.55–78.33	53.77–101.30	[200]
ZTA	Mechanical agitation	Surfactant: Valeric acid	88–94	80–200	[178]
Al ₂ O ₃ / Al ₂ O ₃ -mullite/ Al ₂ O ₃ -CA ₆	Mechanical agitation + injection of compressed air	Foaming surfactant: alpha olefin sulfonate Thickening agent: Hydroxyl-propyl-methyl-cellulose	76.01 \pm 1.44/ 78.14 \pm 0.99/ 84.61 \pm 0.35	100–1300	[201]
Al ₂ O ₃	Mechanical agitation + Evaporation of emulsified alkane droplets	Foaming agent: Decane Anionic surfactant: Sodium lauryl sulfate	78	5–21	[202]
Al ₂ O ₃	Chemical blowing	Blowing agent: Hexamethylenetrtramine (HMT)	64.3	4/11	[175]
Al ₂ O ₃	Mechanical agitation + Evaporation of the emulsified alkane droplets	Foaming agent: Heptane Surfactant: Lutensol AS 2230, B8879, Lutensol ON80; Dispersion agent: Dolapix CE-64	97.5	500–3000	[176]
Al ₂ O ₃	Chemical blowing: (Decomposition of sulphate salt blends)	Blowing agent: (NH ₄) ₂ SO ₄	92.40–96.53	26.00–368.38	[203]
BaTiO ₃	Chemical blowing (Gas evaporation from polyurethane system)	Blowing agent: Polyethylene glycol, 1,4-diazabicyclooctane, Polyoxyethylenesorbitan monooleate	50–70	>30	[204]
SiC	Thermo-foaming	Blowing agent: Water vapor from OH and -OH condensation	93–96	1100–1600	[205]
SiC	Thermo-foaming	Blowing agent: Mg(NO ₃) ₂	94.9–97.5	560–1110	[206]
SiO ₂	Chemical blowing	Foaming agent: CaCO ₃ Fluxing agent: Borax	–	–	[207]
ZrC	Chemical blowing	Blowing agent: <i>n</i> -pentane Curing agent: Ammonia	67.6–93	–	[208]
ZrC	Mechanical agitation + chemical blowing	Blowing agent: Pentane Emulsifier: Tween 20 Curing agent: Citric acid	85	40	[209]

other surfactants. The advantage of this approach over the physical blowing methods is that it allows for a narrower cell size control, ranging from 0.5 to 3 mm, and higher porosity up to 97.5 %, after sintering. Shimamura et al. documented hexamethylenetetramine (HMT) as a blowing and curing agent for the fabrication of porous alumina [175], and the gas released from thermal decomposition of HMT created the desired pores (Fig. 34c). They pointed out that a successful foaming process requires: (1) blowing should occur before the thermosetting resin cures; (2) the fluidity of the suspension should be adequate to retain the gas from escaping outside; (3) The foamed body should be cured after blowing in order to retain the shape and morphology of the pores.

Li et al. further investigated the effect of the precursor sol viscosity, curing agent concentration, and blowing agent concentration on the foam structures [208]. They found that the foam structure was significantly affected by the viscosity of precursor sol (Fig. 35). At the lowest viscosity of 1554 cp, the sample exhibited reticulated pore structure with cell sizes of $\sim 300 \mu\text{m}$, and broken and cracked struts, which was attributed to insufficient stabilisation during the growth of bubbles. Spherical and interconnected cells with size of $\sim 200 \mu\text{m}$ appeared when the viscosity increased to 2025 cp; however when the sol viscosity reached 2700 cp, the structure of foamed ceramics was dominated by closed cells, since it became more difficult for bubbles to rise and break the cell walls during the foaming process. It was then confirmed that the foam prepared from precursor sols with higher viscosity had smaller pore volume and larger densities, as summarised in Table 12. Furthermore, they examined the effect of curing agent concentration on the pore structures and found that the increase of curing agent concentration gave rise to a more rapid gelation. This inhibited the bubble rise and led to the thickening of the struts and cell windows diminish, and foams with higher density and spherical cell like structures were therefore obtained (Fig. 36a-d). Additionally, as expected, the porosity and cell size of the foam increased with the increase of blowing agent, however the effect on the morphology is very limited.

Additionally, Soh et al. used a mixture of ammonium sulphate and aluminium sulphate to fabricate porous alumina. Upon sintering, gases were produced by the thermal decomposition of the mixture which resulted in porous structures [203]. In this process, the foaming heating rate had an effect on the microstructure of the foam, and a higher foaming heating rate led to faster gas evolution intensity and higher porosity, from $\sim 94 \%$ to 96% . However, the high heating rate could cause instability in the foam, therefore an optimum foaming heating rate for gas evolution should be found for good microstructure of the resulting foam.

In summary, macroporous ceramics can be prepared by this easy, inexpensive, and rapid direct foaming approach, and porosity can be controlled by incorporating the right amount of gas foaming phases. This simplified fabrication technique is more suitable for industrial level production than the freeze-casting described above. Meanwhile, the cellular structures produced by direct foaming are stronger than those produced by the replica method due to the absence of flaws in the cell struts [174]. Future work can be done to optimise the pore structures, since the control of the pore morphology, orientation, and distribution is the biggest drawback of direct foaming [204].

2.5. Additive manufacturing

With the demands of advanced energy and environmental applications, porous ceramics ideally should have precisely customised architectures with full control of the geometrical parameters, such as porosity, pore size, and pore interconnectivity [210]. However, despite great efforts paid in the past decades, above discussed techniques can hardly fit for the purpose. Additive manufacturing as an emerging technology allows for the fabrication of precisely tailored porous scaffolds with complex shapes via a layer-by-layer process according to a file of computer aided design (CAD), without using specific tooling (Fig. 37). A scaffold's performance can be realised by the design of materials with adequate pore sizes and porosities, so that mechanical strengths [211].

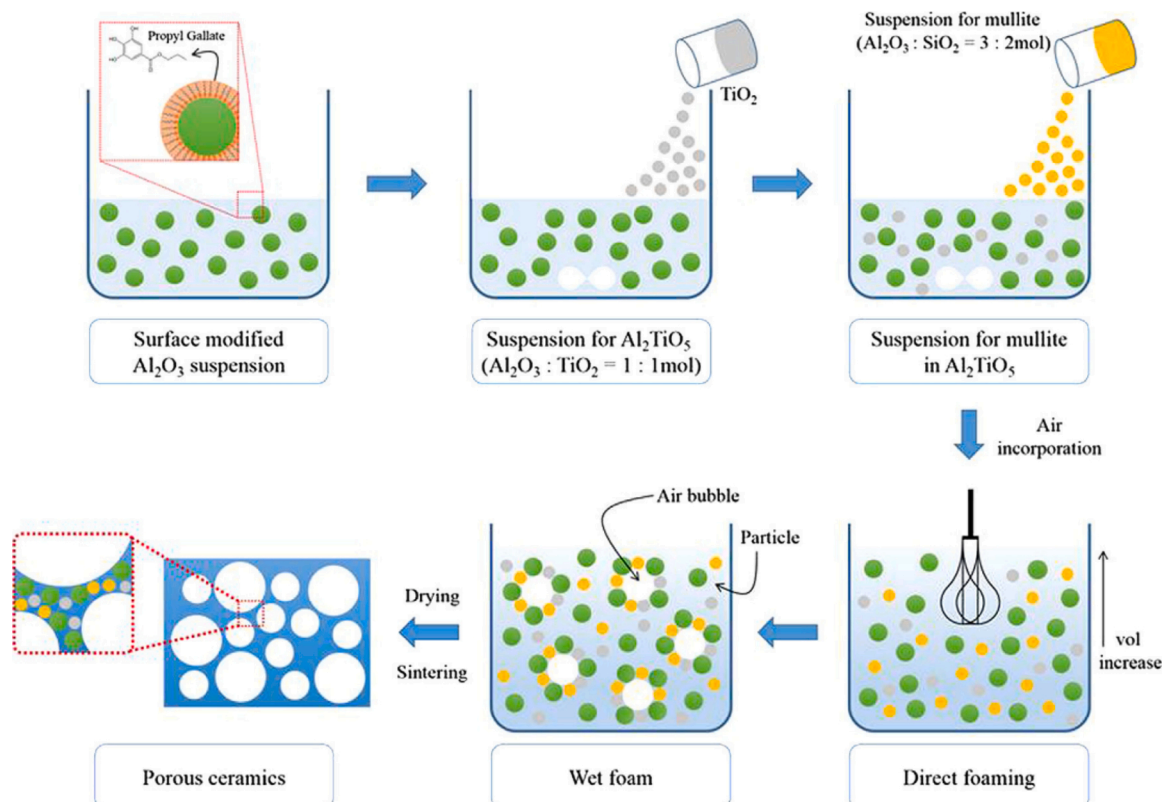


Fig. 29. Preparation of porous Al₂TiO₅-mullite porous ceramics by direct foaming. Reproduced with permission [177]. Copyright 2015, Elsevier B.V.

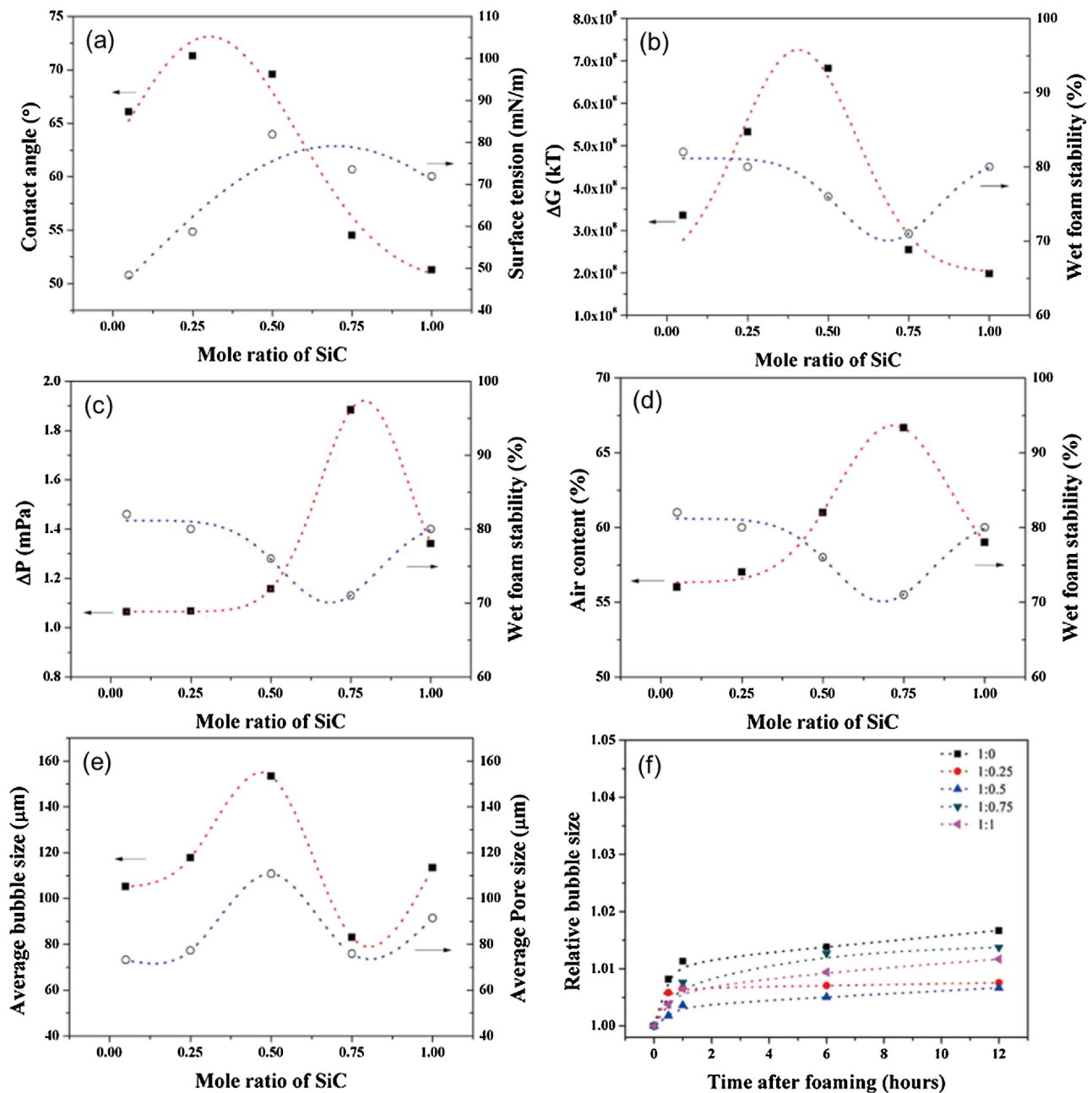


Fig. 30. (a-e) Contact angle and surface tension, adsorption free energy and wet-foam stability, Laplace pressure and wet-foam stability, air content with wet foam stability, average bubble size and average pore size with respect to the mole ratio of SiC in the initial suspensions. (f) The relationship of relative bubble size vs foaming time for foams with different initial SiC: SiO₂ ratios. Reproduced with permission [194]. Copyright 2015, The Ceramic Society of Japan.

This technology stands out over conventional manufacturing methods with such advantages [212]:

- (1) Allow the production of customised near-net-shape pieces with intricate details.
- (2) Reduced human error relevance in the procedures.
- (3) Lower environmental impact, higher manufacturing sustainability as it reduces material waste and energy consumption.

2.5.1. Basics of ceramic additive manufacturing

Compared with metals and polymers, the extremely high melting point of ceramics is one of the most critical challenges in the field of ceramic additive manufacturing. Moreover, the scarce availability of starting materials for the production of the feedstock is another

limitation [214].

As shown in Fig. 38, seven major AM methods including Vat Photopolymerisation (VP, also referred to as stereolithography (SLA)) [215], Binder Jetting (BJ) [216], Material Jetting (MJ, or inkjet printing) [217], Powder Bed Fusion (PBF, extended to selective laser sintering (SLS)) [218], Material Extrusion (ME, or fused deposition modelling (FDM)) [213], Sheet Lamination (SL, or laminated object manufacturing (LOM)) [219], and Direct Energy Deposition (DED) [212], have all been utilised for the fabrication of ceramics.

These methods have been classified as direct method and indirect method, with the starting materials categorised in three states: dry powder, liquid/slurry, and solid-state object (e.g. continuous filament or sheet) (Fig. 39). In a direct method, ceramic material is deposited on the building area to form a layer and sintered immediately to densify the layer. The rapid direct method therefore does not require post-

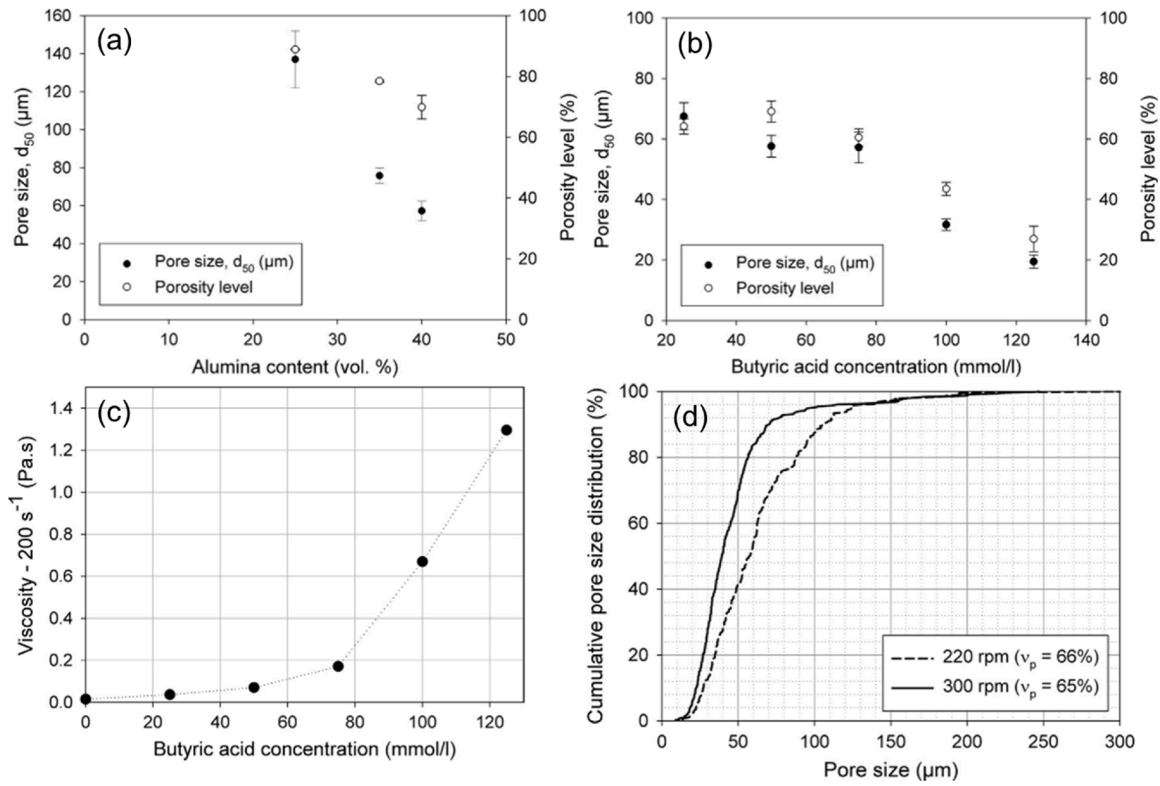


Fig. 31. The pore size and porosity as a function of (a) alumina content, and (b) butyric acid concentration in the initial suspension. (c) The influence of butyric acid concentration on the viscosity of 40 vol% alumina suspension. (d) Cumulative pore size distribution as a function of pore size for foam with 40 vol% alumina suspension, stirred under 220 and 300 rpm respectively. Reproduced with permission [184]. Copyright 2014, Elsevier B.V.

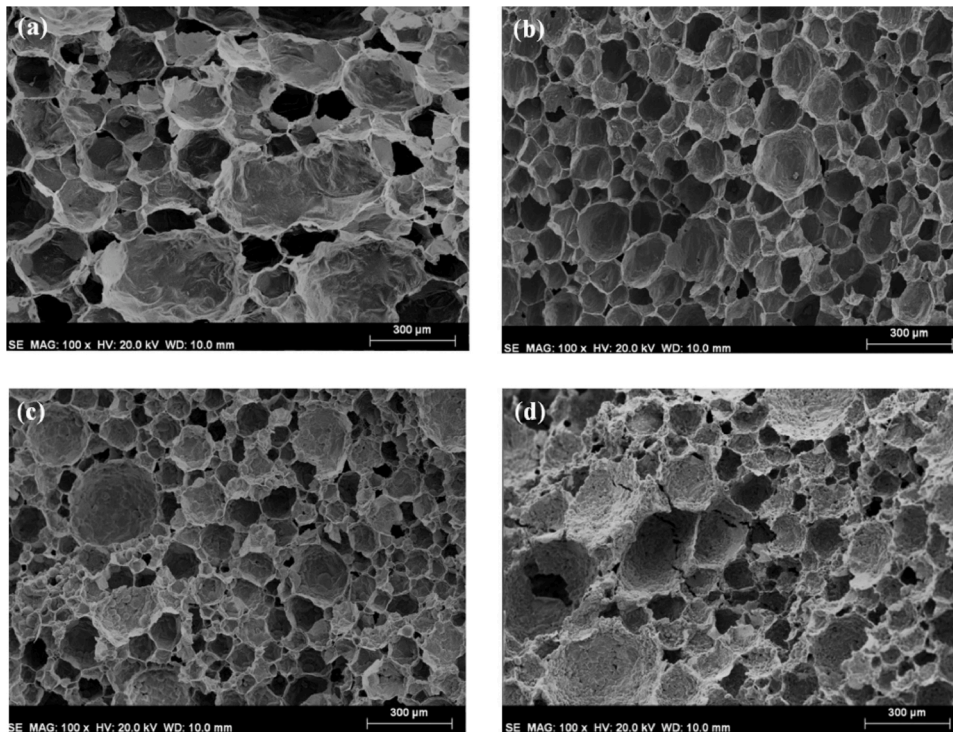


Fig. 32. SEM images showing the effect of valeric acid concentration on the morphology of ZrO_2 sintered at 1480°C for 2 h. (a) 5 mmolL^{-1} , (b) 10 mmolL^{-1} , (c) 30 mmolL^{-1} , and (d) 50 mmolL^{-1} . Reproduced with permission [198]. Copyright 2013, Elsevier B.V.

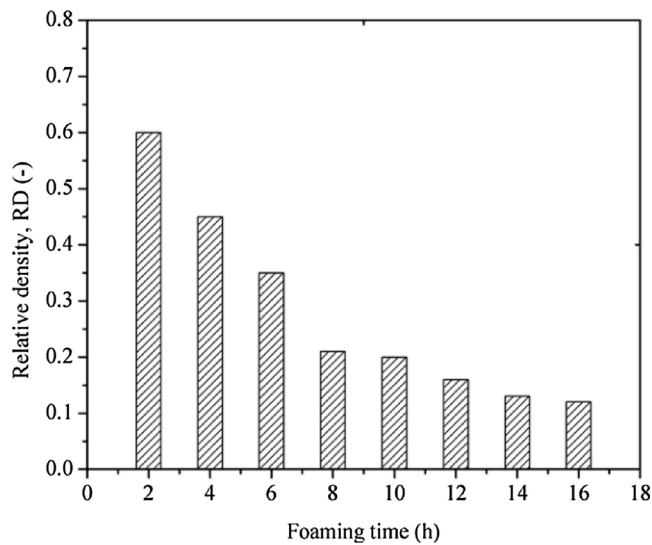


Fig. 33. Effect of foaming time on the relative density of SiC foams. Reproduced with permission [192]. Copyright 2016, The American Ceramic Society.

processing, which gives rise to less densified products and high surface roughness, as compared with indirect AM processes. For indirect AM processes, ceramic materials are mixed with sacrificial polymeric binders, followed by a sintering process to densify the green bodies before optional post-processing to clean the residual material. Indirect AM processes tend to produce highly densified parts with high surface quality and high-strength values, and they are built with high resolution. However, the drawback is that the sintering and other post-processing are demanded, which leads to shrinkage of the final products [221].

Despite that the cost of AM has fallen due to new processes being achieved in the past few decades, it is still more expensive than

conventional methods and not suitable for mass productions [221], the ceramic products have therefore been merely utilised in the field of bioengineering. In this regard, not only high strength, hardness, wear resistance, corrosion resistance, and thermal stability are required, but also the biocompatibility, aesthetic features, surface roughness, and ageing have been the driving force for research [212]. Owing to these outstanding features, ceramics including oxides (Al_2O_3 , ZrO_2 , SiO_2 , TiO_2), nitrides (Si_3N_4 , AlN), carbides (SiC , TiC), calcium phosphates (HA , TCP) [221,222], have been utilised as bone substitute, implants, dentistry, and orthopaedic prostheses [223]. Additionally, piezoceramics like PZT have been fabricated for sensors. These ceramics with applicable AM techniques have been collectively summarised in Table 13.

2.5.2. Potential for porous ceramics production

Due to the brittleness nature, a very tight control of the manufacturing process is needed to deliver the ceramic products with adequate mechanical strength, since the existence of porosity impairs the mechanical strength [212]. However, this inherent feature can be favourable for producing highly-open porous shapes, typically, structures including corkscrew, microlattices, and honeycomb structures that can be easily fabricated by powder-based AM techniques [214]. Although AM fabricated porous ceramic scaffolds can be merely used as non-load or low-load bearing applications, due to the low mechanical strengths that could be generally achieved, the layered structure however was found to be effective in improving the compressive strength of scaffold, due to the progressive failure mechanism [226]. Therefore, we see the opportunity for the production of porous ceramics by AM techniques, which provides the following benefits [220]:

- (a) Structure with almost any shapes and different degrees of geometrical complexity can be manufactured.
- (b) Microstructural features such as porosity, pore size, and pore size distribution can be accurately controlled.

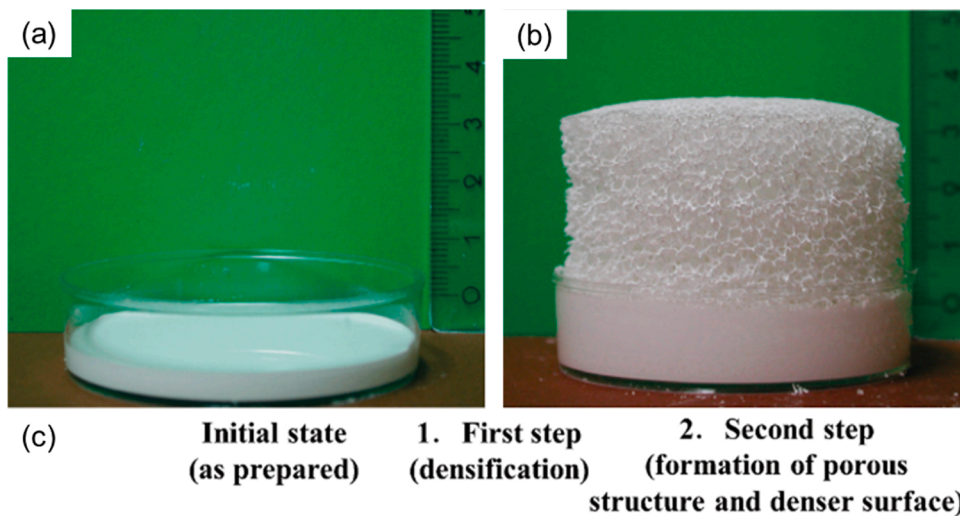
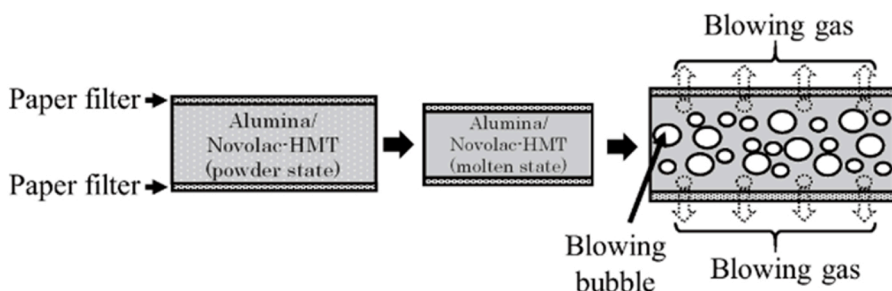


Fig. 34. Bread-making type of autonomous foaming processes: (a) alumina powder suspension poured into the mould, (b) foamed green body under controlled temperature of 23 °C, humidity of 65 % for 3 h. Reproduced with permission [176]. Copyright 2008, The American Ceramic Society. (c) Schematic fabrication steps for porous alumina by using HMT as the blowing and curing agent. Reproduced with permission [175] Copyright 2017, The Ceramic Society of Japan (For interpretation of the references to colour in this figure legend, the reader is referred to the web version of this article.).



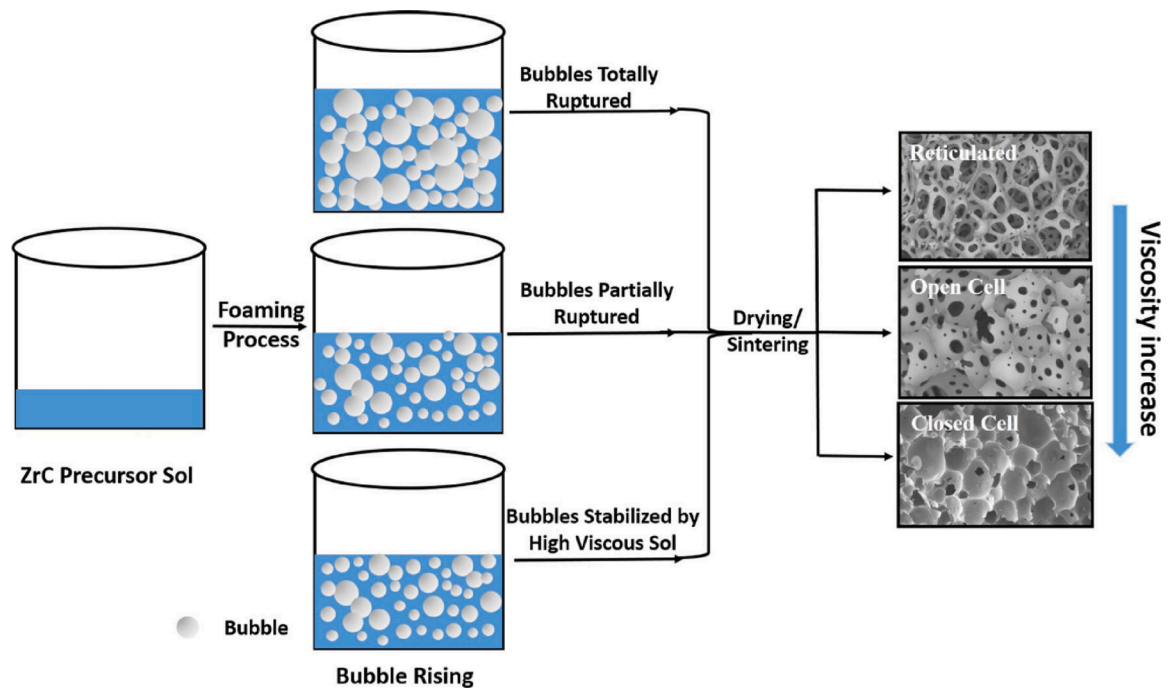


Fig. 35. The effect of viscosities on the foaming process and final microstructures of the resulting samples. Reproduced with permission [208]. Copyright 2015, Springer Nature Switzerland AG.

(c) Time effectiveness compared with traditional pore forming strategies.

Polzin et al. printed porous Al_2O_3 and SiC ceramics via the binder jetting technique [227], and highly porous Al_2O_3 and SiC with porosities up to 69 % and 55 % were obtained, demonstrating abilities for their potential applications, including insulators, hot gas filters, and catalyst support. Meanwhile, using the AM techniques for the fabrication of interconnected HA [228], bioglass [229], and TCP-based bio-scaffolds [230], with porosities from 40 % to 70 % and pore sizes from 50 to 1000 μm , has been well-established [210].

It is worth noting that powder-based technologies have been mostly used for the fabrication of porous ceramics (Fig. 40a-c) [221], and inherent porous structures can be easily produced, which reduces the cost [214]. However, low strength along with the brittleness makes these scaffolds difficult to handle during the processing stage [211], especially removing excessive loose powders without damaging the fragile scaffold is one of the major challenges. Therefore, the fabrication details and limitations should be taken into consideration during the early designing stage [231,232].

In this regard, as summarised in Fig. 41, the processing parameters such as powder packing density, powder flowability, layer thickness, binder drop volume, binder saturation, powder wettability, and post-processing should be optimised, since non-uniform shrinkage during sintering may lead to a lower mechanical strength or even breakage of the scaffolds [211]. Advanced sintering technique such as plasma treatment of the powder particles is ideal for enhancing the flowability of fine particles, giving rise to high level resolution of scaffolds,

meanwhile, the development of fast and reliable print heads can be of help as well [210].

The AM for porous ceramics is still in its infancy stage, and significant achievements could be achieved by completing the following works in the future [212,220,224,234]:

- The impact from the inherent drawbacks of AM techniques: low dimensional accuracy and poor surface finishing due to the layer by layer formation of the parts should be minimised.
- The selection of printable materials for each AM method is quite limited, therefore improvement of the existing technologies with an emphasis on printable materials should be addressed.
- The pore size distribution of existing AM fabricated porous ceramics is in the microscale, reducing it down to nanoscale will pave the way to a wide variety of energy and environment related applications. This could be achieved by combining AM with other pore forming strategies such as partial sintering and sacrificial templates.
- The porosity-property relationship that indicates the effect of pore geometry, orientation, and pore arrangement on the mechanical properties of materials has yet to be established. Finite element modelling can be combined with experimental study to provide an insight of this relationship.
- The cost of the AM techniques should be more competitive.

3. Properties of porous ceramics

3.1. Mechanical properties

Introducing pores into ceramics is believed to be detrimental to the mechanical strength of structural materials, since high-porosity porous ceramics exhibit weak resistance to crack initiation, as a result, the improvement of desired specific performance always comes at an expense of their mechanical properties [167,235]. However, a good offset to the sacrificing mechanical performance and even enhanced damage tolerance can be obtained by controlling the microstructural characteristics.

Table 12

The effect of precursor sol viscosity on the density of foamed ceramics. Reproduced with permission [208]. Copyright 2015, Springer Nature Switzerland AG.

Viscosity (cP)	Density (g cm^{-3})	Porosity (%)
1554	0.12	92.5
2025	0.21	89.4
2699	0.38	74.5
2954	0.53	67.6

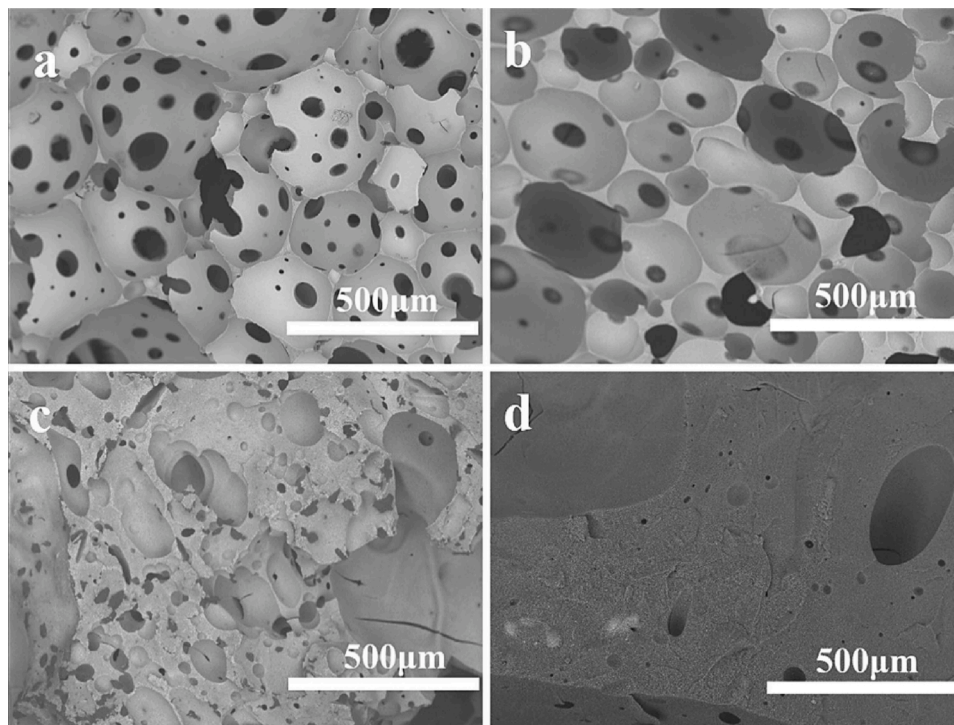


Fig. 36. SEM images of ZrC foam prepared with various curing agent concentrations of (a) 1%, (b) 1.5 %, (c) 2%, (d) 3%. Reproduced with permission [208]. Copyright 2015, Springer Nature Switzerland AG.

3.1.1. Mechanical performance of porous ceramics

Porosity of porous ceramics has the most direct influence on their mechanical performance. As shown in Fig. 42a,b, when the porosity of porous Y_2SiO_5 increases from 60.7% to 88.4%, the density reduces from 1.74 g cm^{-3} to 0.52 g cm^{-3} , whilst the compressive strength decreases dramatically from 38.2 MPa to 0.9 MPa, correspondingly [196].

Apart from porosity, the pore orientation is believed to be another factor that influences the mechanical behaviour of porous ceramics. Lichtner et al. obtained the relationship between pore anisotropy and the mechanical response of hierarchical porous ceramics [167]. As shown in Fig. 43, by changing the orientation of pores relative to the applied stress, the compressive strength of porous ceramics was increased by an average of 6.9 times (Fig. 43a). The longitudinal samples produced via freeze-casting exhibited the highest compressive strength and failed gradually, since the solid phase aligned in the direction of loading would help to carry and transfer the load through the porous structure (Fig. 43b). On contrast, when samples were loaded transversely to the applied force, the volume of material that carrying the load was minimised, thus localised damages immediately occurred and disconnected walls were densified (Fig. 43c). While the isotropic samples that fabricated by sacrificial template has uniform compressive strength between the longitudinal and transverse samples, they also experienced a relatively sharp compressive peak and failure, which can be ascribed to the concentration of randomly located pores, leading to the brittle rupture (Fig. 43d). Based on the failure behaviour of samples under compression test, it can be deduced that the connectivity of walls transverse to the pore orientation helped in preventing the buckling and

shearing passing through each other. Hence, the density of cross-connections is virtually responsible for the final mechanical performance.

The fracture energy and strain tolerance in porous ceramics, however, can be increased by carefully controlling the size, shape, and orientation of the pores and grains. To this end, Ohji studied the mechanical properties of porous Si_3N_4 with fibrous grains both randomly oriented and aligned in one direction [24]. They showed that by adjusting the sintering temperature and holding time, it is possible to achieve improved fracture energy and strain tolerance depending on the porosity for isotropic porous Si_3N_4 , as displayed in Fig. 44(a,b). Meanwhile, aligned fibrous grains were obtained by tape casting the fibrous seed crystals under a pressure of 1 MPa. It was found that the pores around the grains promoted debonding between interlocking grains without fracture. Owing to the crack bridging and pull-out of the grains, the large fracture energy ranging from 300 to 500 J m^{-2} was obtained for samples with porosity below 20 %, as shown in Fig. 44(c,d), when the stress was applied parallel to the alignment direction. Surprisingly, when the stress was applied perpendicular to the grain alignment, the fracture energy was still considerably higher than that of the isotropic material, despite the slightly lower fracture strength, indicating that tilted fibrous grains also contributed to the bridging or pull-out toughening (Fig. 44e). This study has demonstrated that a well-controlled size, shape, and orientation of pores and grains provides a good offset of the mechanical strength loss.

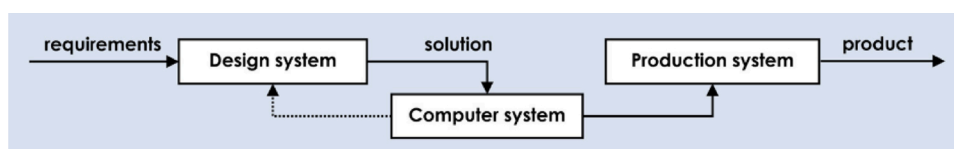
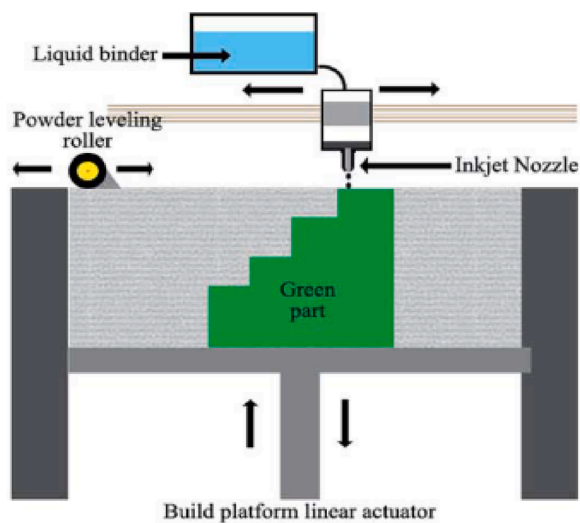
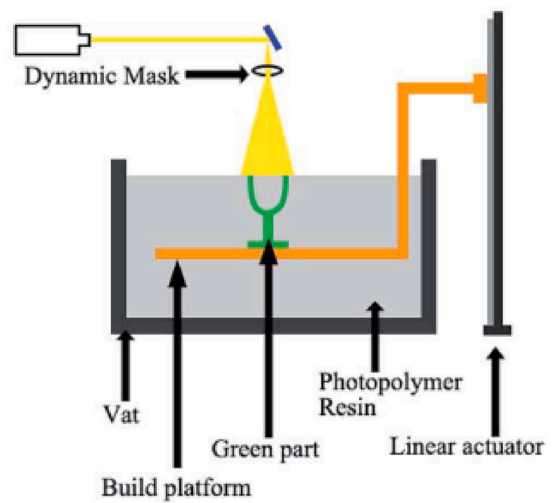


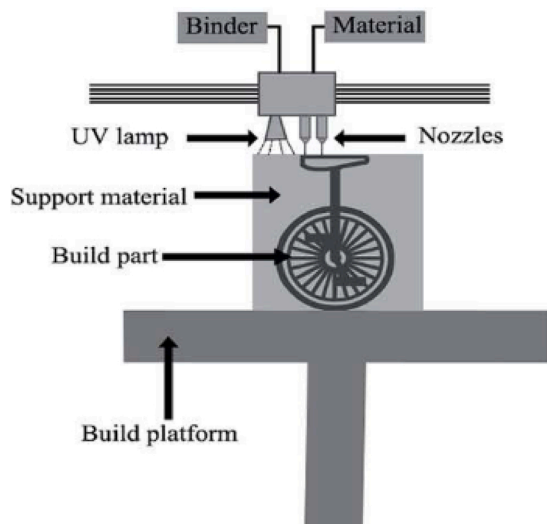
Fig. 37. Overview of producing ceramic objects via AM. Reproduced with permission [213]. Copyright 2017, Emerald Publishing Limited.



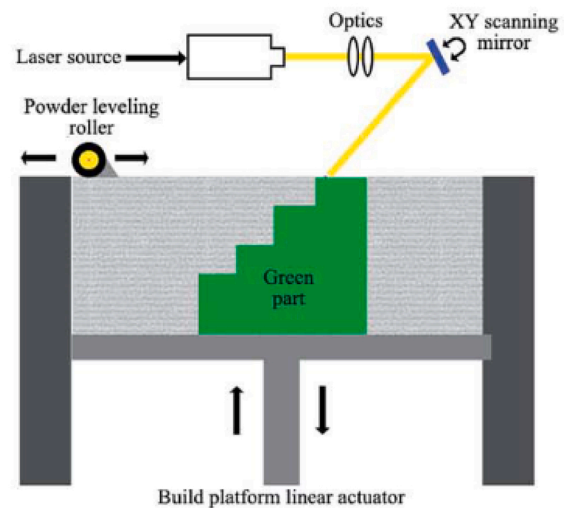
i. Vat Photo polymerization



ii. Binder Jetting



iii. Material Jetting



iv. Powder Bed Fusion

Fig. 38. Schematic of different types of AM techniques. Reproduced with permission [220]. Copyright 2019, The Royal Society of Chemistry.

3.1.2. Enhanced damage tolerance of porous ceramics

A significantly improved mechanical behaviour can be obtained through the crack deflection, bridging, pull-out, and phase transition mechanisms, by incorporating reinforcing phases into the ceramic matrix, to form porous ceramic matrix composites [165].

Incorporation of a second phase into the matrix is more effective for improving the strength than changing the fabrication approach. Oh et al. successfully increased the fracture strength of porous Al_2O_3 by using SiC particles as a filler [41]. The strengthening mechanisms are believed to originate from the grain refinement and crack-tip bridging effects. Han et al. introduced mullite fibres into porous SiC ceramics [236]. They found that merely 4% of mullite fibres could successfully increase the bending strength for 2.2 times to 15.7 MPa through the synergistic effect of fibre bridging, crack deflection, and pull-out mechanisms despite the increase of porosity from 41.4 % to 46.8 % (Fig. 45a,b).

As outlined in 2.1.1, sintering additive induced in-situ reaction-

bonding technique has exhibited potential for enhanced strength. Han et al. reported the preparation of SiC whisker reinforced SiC porous ceramics, using ZrO_2 as the sintering aid. A bending strength improvement from 9.7 MPa to 28 MPa was obtained for the sample with 3.3 wt.% SiC whiskers [237]. Therefore, the concept of composite could have a very impressive role to play in improving the mechanical performance of the porous ceramics. This can be translated as that the SiC whiskers not only bridged the SiC grains, but also transformed into SiO_2 and then reacted with the sintering aid ZrO_2 to form a third phase, zirconite, leading to more compact SiC particles after sintering, also known as transformation toughening mechanism.

All above-mentioned mechanisms confer optimal damage tolerance to the materials, overcoming the brittleness limited mechanical strength of porous ceramics. The remaining challenge, as in any composites, is the effective dispersion of the reinforcement agent and the binding between the filler and matrix, whilst the alignment in these porous

structures is even more essential. Existing knowledge in conventional composites therefore can be borrowed in order to tackle these issues.

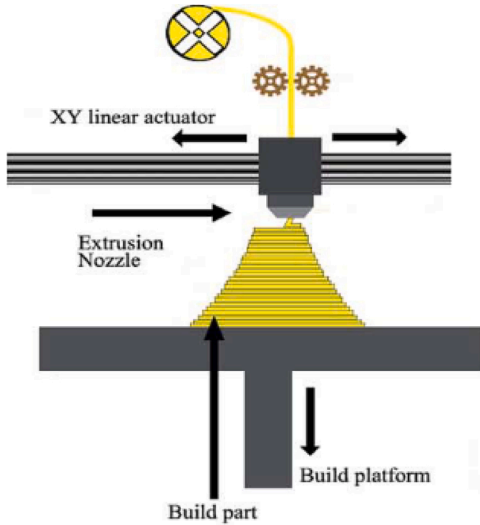
3.2. Thermal properties

Following the discussion of damage tolerance in 3.1.2, porous ceramics possess extremely good maintenance of their mechanical properties after being subjected to cold-hot cycles, which is referred as great thermal shock resistance. Porous ceramics require tortuous and lengthy path for heat transfer, therefore exhibiting low thermal conductivity. The combination of excellent thermal shock resistance and low thermal conductivity, as well as good mechanical strength at high temperature, make porous ceramics exceptional candidates for applications under harsh

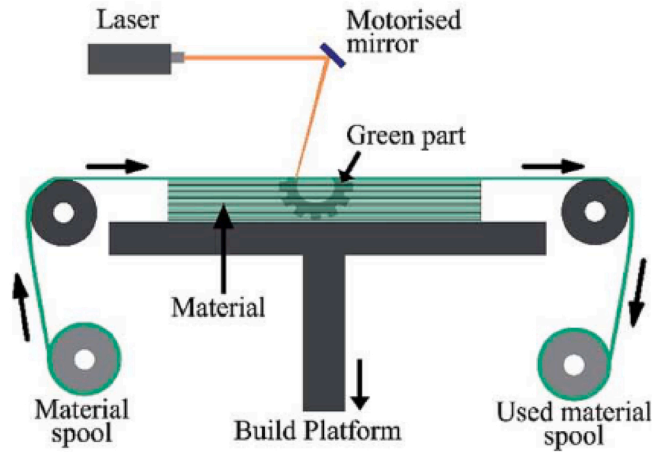
conditions.

3.2.1. Thermal shock resistance

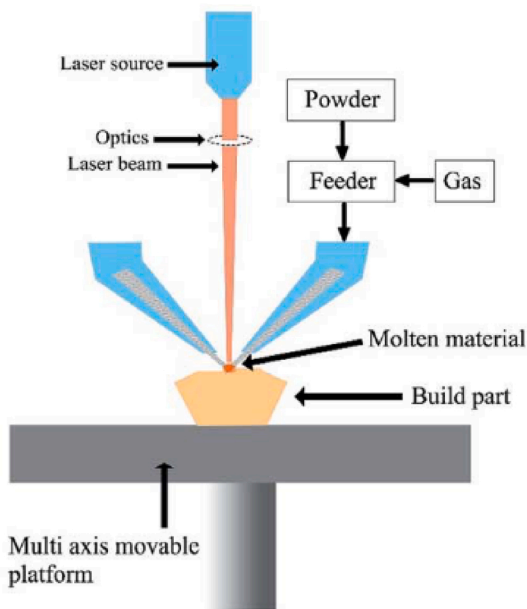
The thermal shock resistance of ceramics is defined by the reduction in strength and degree of damage in the materials, subjected to significant temperature fluctuations [238]. In general, this property is examined by measuring the residual flexural strength of a sample after a heating and quenching cycle. The energy dissipation during fracture as a result of pore-induced crack deflection and arrest is believed to be the main reason for the improved thermal shock resistance in porous ceramics [239]. Chen et al. investigated the effect of pores on the crack initiation and crack propagation within Si₃N₄ ceramics subjected to thermal shock [240]. As shown in Fig. 46a-d, owing to the crack-pore



v. Material Extrusion



vi. Sheet Lamination



vii. Directed Energy Deposition

Fig. 38. (continued).

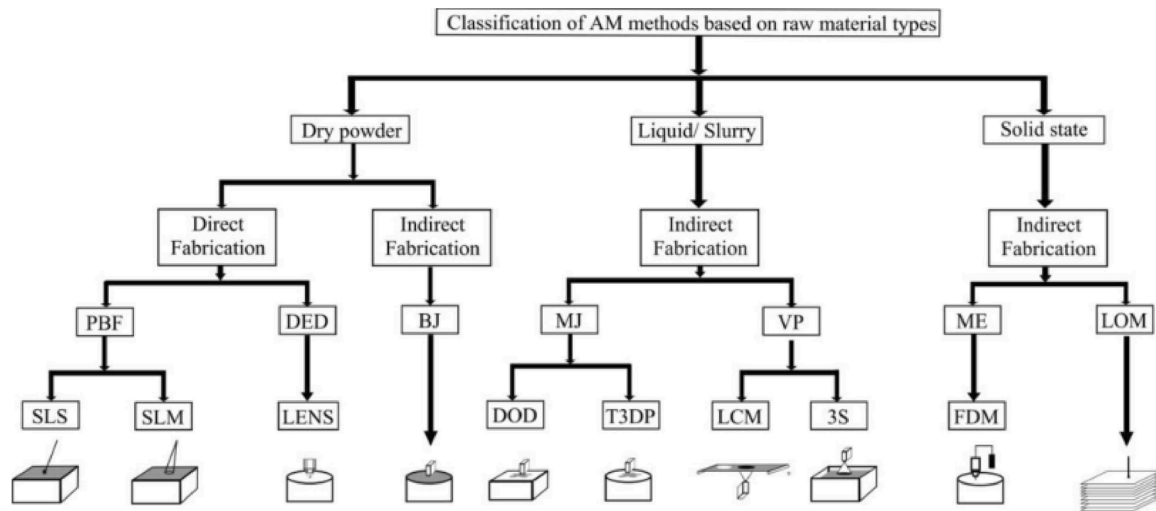


Fig. 39. Classification of AM methods based on types of raw materials. Reproduced with permission [221]. Copyright 2019, Springer Nature Switzerland AG.

Table 13

List of ceramics prepared by different AM methods, summarised from previous reviews [210,221,224,225].

Categories	Materials	VP	BJ	MJ	PBF	ME	SL	DED
Oxides	Al ₂ O ₃	✓	✓	✓	✓	✓	✓	✓
	ZrO ₂	✓	✓	✓	✓	✓	✓	✓
	SiO ₂	✓		✓	✓	✓	✓	
	TiO ₂		✓		✓	✓	✓	
Nitrides	Si ₃ N ₄	✓	✓		✓	✓	✓	✓
	AlN					✓	✓	
Carbides	SiC	✓	✓		✓	✓	✓	
	TiC				✓	✓	✓	
Calcium phosphate	HA	✓	✓		✓	✓	✓	
	TCP	✓	✓		✓	✓	✓	
Piezoceramics	PZT	✓	✓	✓	✓	✓	✓	

interactions, the pores could terminate the propagation of cracks, which resulted in a decreased crack depth and less strength loss (Fig. 46e). Furthermore, they proposed numerical simulations considering the coupling between the thermo and mechanical behaviour of porous Si₃N₄ and found that the time for crack initiation dropped with the increase of

the porosity in porous ceramics. On the contrary, the time for crack propagation rose remarkably with increased porosity, since pores could hinder the propagation of crack (Fig. 47a, which restricted the crack expansion and further strength loss (Fig. 47b) [240].

For this reason, the strength of samples with higher porosity therefore undergoes a relative mild decrease under thermal shock [241,242]. Lu et al. evaluated the thermal shock behaviour of porous Si₃N₄ [243], and found that higher porosity exhibited better thermal shock resistance. Since the pores acted as crack arresters, thereby increased their resistance to thermal shock fatigue (Table 14). Furthermore, they proposed that the oxidation layers formed on the cracks might have acted as a thermal barrier, which reduced the heat transfer and benefitted the thermal shock resistance [243].

It has been conclusively shown that the thermal shock resistance closely associates with mechanical properties including fracture strength, elastic modulus, poisson ratio, and thermal properties such as thermal expansion coefficient and thermal conductivity [244]. A better connectivity of open pores and degraded bonding between grains within highly porous ceramics are therefore favoured, as they could provide a reduction in the stress concentration, therefore good crack propagation resistance [243]. Jin et al. used porous ZrB₂-SiC ceramics of different

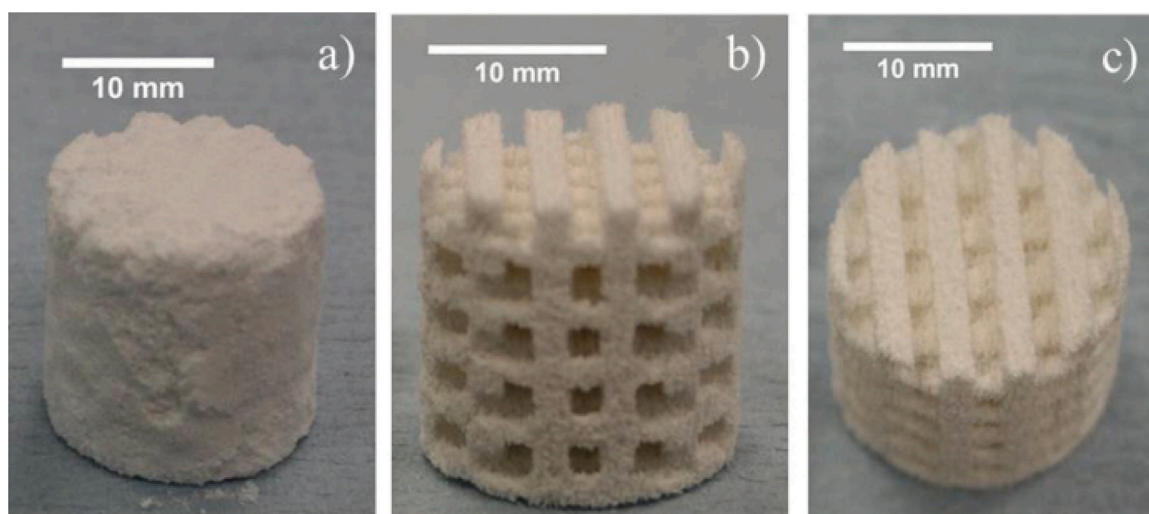


Fig. 40. Schematic of de-powder of as-obtained HA green bodies: (a) Printed scaffold as-removed from the build bed, (b and c) de-powdered scaffold. Reproduced with permission [233]. Copyright 2014, Elsevier B.V (For interpretation of the references to colour in this figure legend, the reader is referred to the web version of this article.).

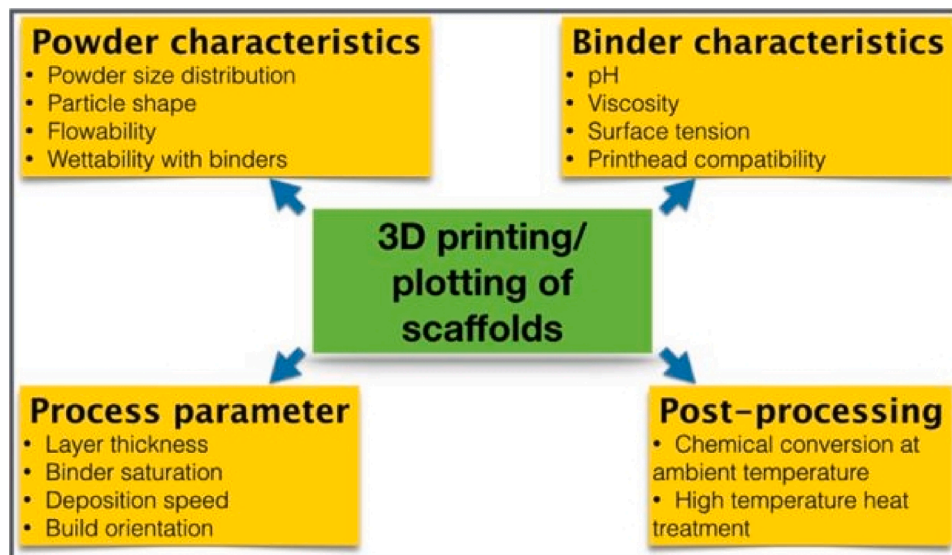


Fig. 41. Major parameters that should be taken into consideration upon powder-based 3D printing. Reproduced with permission [223]. Copyright 2016, Elsevier B.V.

porosities and pore sizes to achieve a good balance between mechanical properties and thermal shock resistance, and reported that the sample with a porosity of 11 % and mean pore diameter of $5.5 \pm 0.1 \mu\text{m}$ prepared by partial sintering had achieved an optimal balance [25]. The results suggest that an optimum configuration of porosity and pore size could allow for the optimal combination of mechanical properties and thermal shock damage resistance.

It is well-known that porous ceramics possess good thermal shock resistance, which can be used for a series of cyclic thermal shock applications such as solar thermal storage system [244], heat absorbing materials [245], thermal insulator, hot-gas and molten-metal filters [237]. However, competent thermal shock resistance is normally obtained by ceramics with low porosities ($< 50\%$). Studies of improving thermal shock resistance for highly porous structures are therefore demanded for the aforementioned applications. A comprehensive understanding of the effect of fabrication method, the resulting pore characteristics on the thermal shock resistance has yet to be gained.

3.2.2. Low thermal conductivity in porous ceramics

As the conduction is generally believed to play the leading role in heat transfer compared with the convection and radiation mechanisms,

since the convection and radiation only take effect at high temperatures [106]. Reduced thermal conductivity is essentially governed by materials' capability to resist thermal transfer through scattering of phonons (or photons) by defects, such as grain boundaries, stacking faults, and pores, or "hopping" of vacancies [246,247]. It has been well-established that the air-containing pores have significant effects on the thermal conductivity of materials because the pores function as obstacles against heat transfer. Alternatively, the air with conductivity of $0.025 \text{ W m}^{-1} \text{ K}^{-1}$ can be regarded as incorporated insulation phase that leads to lower thermal conductivity [248]. These findings imply that by introducing pores and controlling the microstructural features of porous ceramics including porosity, pore size, and size distribution, a good management of phonon transport which dictates the thermal insulation performance can be obtained [182]. In this regard, ceramic thermal insulators containing high volume fractions of smooth and uniformly distributed pores have been actively pursued [249,250].

The porous ceramics with outstanding thermal insulation effect ($K < 1 \text{ W m}^{-1} \text{ K}^{-1}$) are listed in Table 15. From Table 15 we can see that there is a synergistic effect of intrinsic thermal conductivity and porosity on the thermal conductivity of porous ceramics. The rule-of-mixture has also been adopted to describe their relationship [251]:

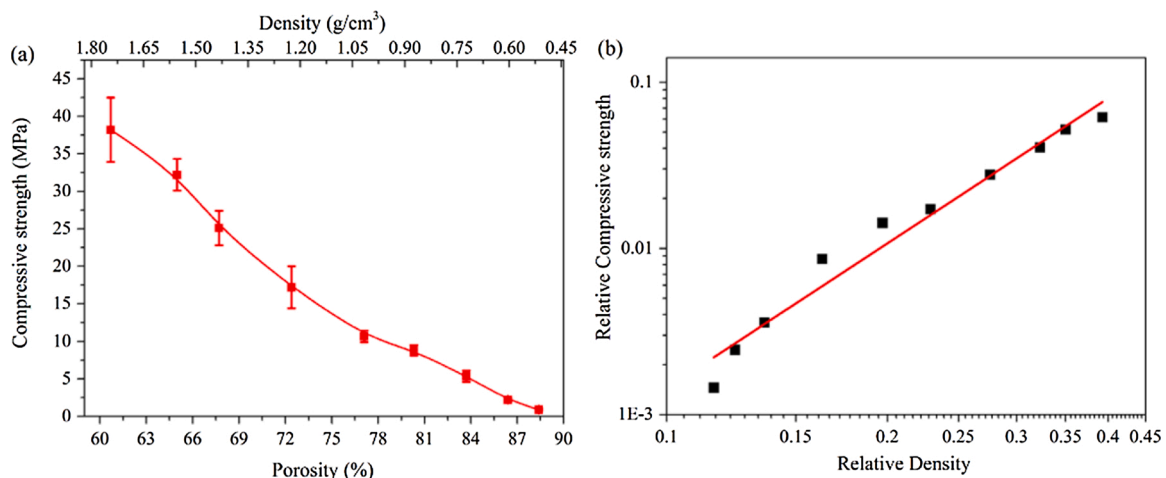


Fig. 42. Mechanical properties of porous Y_2SiO_5 : (a) Effect of porosity on the density and compressive strength; and (b) Relationship between the relative density and relative compressive strength. Reproduced with permission [196]. Copyright 2016, Elsevier B.V.

$$K_T(T) = \phi K_g(T) + (1 - \phi) K_s(T) \quad (9)$$

Where ϕ is the porosity, $K_g(T)$ is the gaseous thermal conductivity, and $K_s(T)$ is the intrinsic thermal conductivity of a solid material.

Hu et al. summarised the thermal conductivity of Ti_2AlC with porosities from 34 to 60 vol. % from their experimental results [129], EMT model, and Maxwell-Eucken model, respectively (Fig. 48a,b). It was concluded that with the increase of porosity the thermal conductivity declined significantly, while the change of pore size could hardly affect the thermal conductivity. This study again demonstrated the direct relationship between porosity with thermal conductivity.

3.2.3. Anisotropy of heat transfer

Both experimental results and analytical models indicate that porous ceramics with pore size ranging from submicron to several microns exhibit different thermal properties in the direction of elongation. Honda et al. studied the anisotropic thermal conductivity of porous alumina with highly oriented grains in one direction, fabricated by pulsed electric current sintering (PECS) [42]. The thermal conductivity alongside the pressing direction was $11.0 \text{ Wm}^{-1} \text{ K}^{-1}$, as a result of a small number of points of contact between alumina platelets and the existence of large pores. By contrast, the thermal conductivity perpendicular to the pressing direction was $22.6 \text{ Wm}^{-1} \text{ K}^{-1}$ since the alumina platelets were interconnected as a continuous body. The $11.6 \text{ Wm}^{-1} \text{ K}^{-1}$ variation with respect to different directions indicates that the thermal conductivity of porous ceramics is highly direction-sensitive.

It is possible that porous ceramics with closed pores aligned orthogonal to the heat flow significantly enhanced the thermal insulation capability, as heat preferentially transferred along the struts that parallel to the pore orientation (Fig. 49a,b). In this regard, freeze casting that provides a good control over the microstructure is therefore possibly the most effective method for the fabrication of porous ceramics targeting thermal insulation applications, with good mechanical strength and low thermal conductivity [5].

Furthermore, five basic thermal conductivity models for the two-

component porous ceramics have been summarised in Table 16. Based on these theoretical models, the series model is believed to be the best model to describe the thermal insulation performance, agreeing well with experimental results (Fig. 50).

The pore geometry also has a strong influence on the thermal properties, which includes the pore shape, tilt angle, and aspect ratios of ellipse pores. Arai et al. used open pores of porous thermal barrier coatings (TBCs) prepared from a mixture of zirconia and polyester to investigate this influence [256], and the results is presented in Fig. 51a-c. They found that the pore shape had little effect on the thermal conductivity, however a lower thermal conductivity could be achieved by models with low tilt angle and aspect ratio of ellipse pores. These findings again suggest that porous TBCs with needle-like pores have significantly reduced the thermal conductivity, and that pores arranged normal to heat flow direction lead to lower thermal conductivity. These results agree with their theoretical model analyses.

As summarised in Table 17, an increase of porosity for achieving low thermal conductivity inevitably sacrifices the mechanical strength of porous ceramics, i.e. a trade-off between low thermal conductivity and high mechanical strength. To address this issue, a second phase can be introduced to improve the mechanical strength for porous ceramics, whilst trying to maintain the good thermal insulation performance by selecting suitable fillers and controlling the pore features. Zhang et al. attempted to address this issue by introducing ZrO_2 fibres as the reinforcing phase into porous Y_2SiO_5 [257]. By increasing the ZrO_2 fibre content from 0 to 30 Vol%, the thermal conductivity of the samples dropped from 0.68 to $0.35 \text{ Wm}^{-1} \text{ K}^{-1}$, while the bending strength increased from 12.2 to 40.1 MPa . Impregnating porous ceramics with other materials is another efficient approach. Hong et al. impregnated highly porous zirconia ceramics with silica aerogel [258], and they recorded an increased compressive strength from 9.2 - 25.5 to 15.4 - 36.8 MPa . The silica aerogels with mean free path of $\sim 50 \text{ nm}$ gave rise to a lower thermal conductivity of $0.041 \sim 0.098 \text{ Wm}^{-1} \text{ K}^{-1}$ for the resultant composites, despite of the decrease in porosity [258].

The mechanical properties and thermal performance of porous

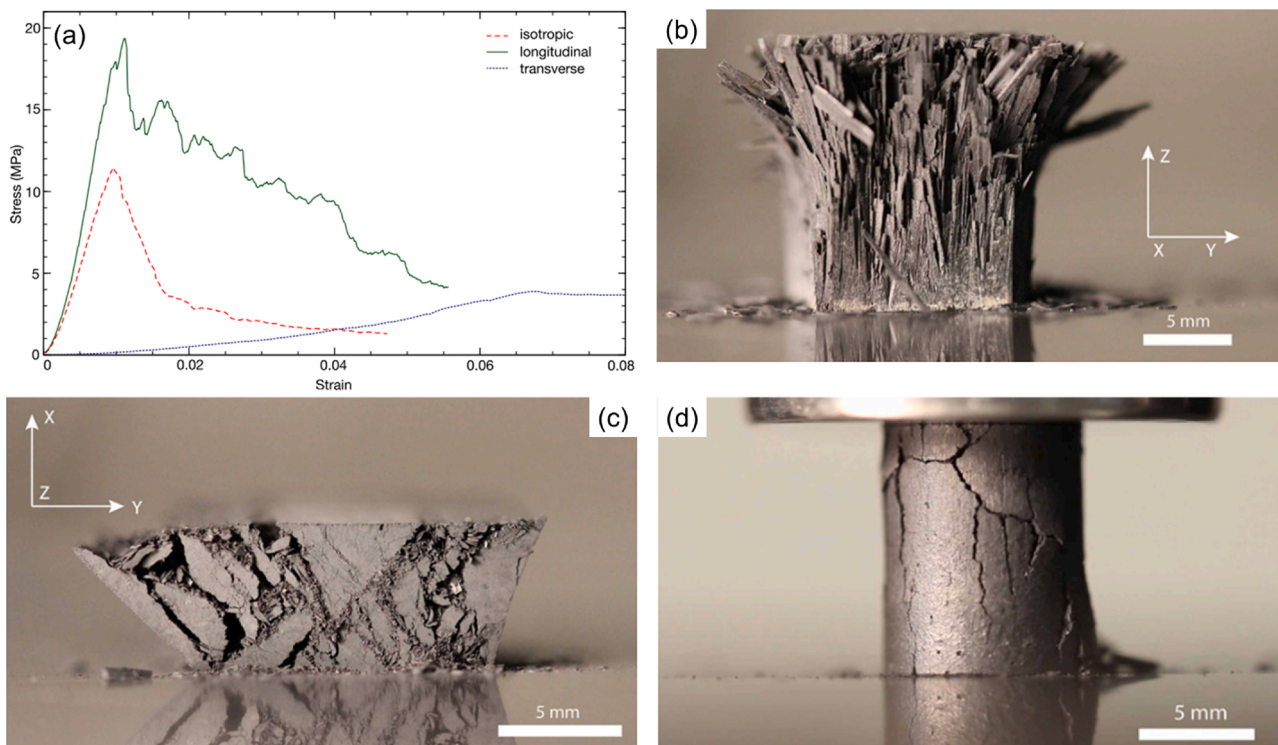


Fig. 43. (a) Stress-strain curves obtained under compression and (b-d) digital images of the failed samples with pores arranged in: longitudinal, transverse, and isotropic to the freezing directions. Reproduced with permission [167]. Copyright 2015, The American Ceramic Society.

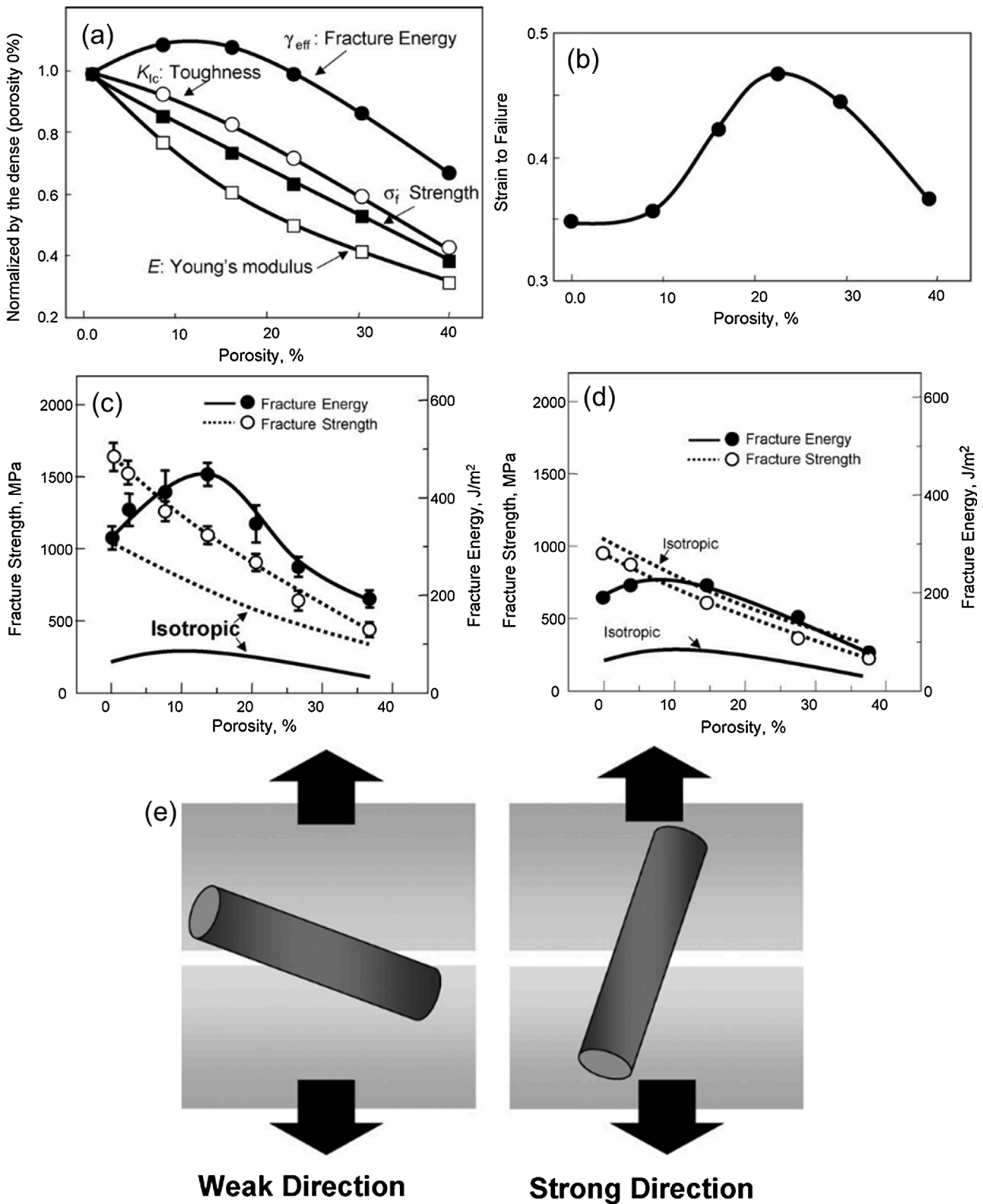


Fig. 44. (a) Young's modulus (E), (b) fracture strength (σ_f), (c) fracture energy (γ_{eff}), and (d) fracture toughness (K_{IC}), as a function of porosity for isotropic porous Si_3N_4 ceramics. (e) Schematic of crack bridging in both the strong direction (parallel to the grain alignment) and the weak direction (parallel to the grain alignment). Reproduced with permission [24]. Copyright 2008, Elsevier B.V.

ceramics are comprehensively summarised in this section. Engineering pores in the ceramics inevitably sacrifice their mechanical strength, however, a good offset of the mechanical strength loss can be achieved by either carefully controlling the microstructural features of both pores

and grains or introducing reinforcement phase and sintering additives during the synthesis. Furthermore, benefiting from the energy dissipation effect during fracture, as a result of pore-induced crack deflection and arrest, porous ceramics possess enhanced damage tolerance and

thermal shock resistance, as compared with their dense counterpart. The additional merit comes from the low thermal conductivity, which can be effectively manipulated by changing the microstructural characteristics of pores.

Combined with their low thermal expansion coefficient, high temperature stability, and excellent chemical stability, porous ceramics have been widely used as thermal insulators in heat exchangers, and heat shields [259], energy-efficient building materials [260], and thermal barrier coatings (TBCs) on gas turbines [256]. By selecting the appropriate materials and processing approach, the conflicting demands of low thermal conductivity and high mechanical strength can be met.

4. Applications

Sustainable energy production today represents the biggest global challenge, because large CO₂ emission was caused by industrial production that rely mainly on fossil fuels which results in global warming, climate change and environmental contaminations. This needs to be tackled urgently by finding alternative energy sources, as a contribution to establish a sustainable society. In this regard, porous ceramics could play a valuable role in these efforts, owing to the special features discussed previously. We will summarise below the typical examples that porous ceramics have been applied in different areas.

4.1. Filtration applications

Filtration has been heavily involved in modern industries, from chemical, biomedical and environmental sectors to energy sectors. Porous ceramics with uniform porosity, pore sizes, adequate permeability, and certain structural strength can be the core elements for components in constructing a variety of filtration systems [202,261]. Compared with metal- and polymer-based porous materials, the unique and outstanding properties, such as high temperature stability, strong thermal shock resistance, excellent corrosion resistance, low thermal expansion, and good durability, make porous ceramic ideal candidates for hot gas filtration in the power generation industry, diesel particulate filters, and water purification media.

Aerosol emissions that have severe effects on human health can be removed by filters via three major mechanisms: sieving, surface adhesion, and pore channel capture [262]. By controlling the porosity and pore size, filters can be tailored for different situations. Filters with pore size around 1 μm are suitable for fine-particle filtration (e.g. PM_{2.5}), while for hot-gas filtration applications and diesel particulate filters, the pore sizes are normally larger than 10 μm [263].

The permeability of porous ceramics is considered as one of the most important properties for gas filters (Fig. 52a), which is given by Darcy's equation:

$$\frac{\Delta P}{L} = \left(\frac{\mu}{k_1}\right) \times \nu_s + \left(\frac{\rho}{k_2}\right) \times \nu_s^2 \quad (10)$$

Where ΔP is the pressure drop, L is the thickness of the filter material, μ is the viscosity of the gas, ν is the fluid velocity, ρ is the fluid density, and k_1 and k_2 are Darcian and Non-Darcian permeability [264].

As shown in Fig. 52(b–e), the high open porosity, large pore size, and good pore connectivity all contribute to the enhanced permeability and filtration velocity, but at the expense of deteriorated mechanical strength and insufficient separation efficiency, in agreement with the modelling studies (Fig. 53). A balance is thus required to achieve an optimal performance for the final filter. The filter quality factor has also been adopted to evaluate the filtration performance:

$$q_F = \frac{\ln(1/P)}{\Delta p} \quad (11)$$

Where q_F is defined as the filter quality factor, P is the particle penetration, and Δp is the pressure drop [265].

The microstructural features of filters should be optimised for a trade-off between ideal filtration performance and mechanical robustness. Considering the above-mentioned criteria, ceramic filters normally present a porosity around 50 % and an average pore diameter of 10 μm [68]. In this context, emphases should be placed on the material selection, processing approaches, and microstructural features for designing efficient porous ceramic-based hot-gas filters, diesel particulate filters, and water filtration systems.

4.1.1. Hot gas filters

The specific high temperature processes (600–900 °C) in advanced clean coal and fuel cell technologies necessitate the development of hot-gas clean-up units, which separate particles at high temperatures to avoid excessive emission or damage to the downstream equipment for power conversion [261,266]. Porous ceramics with high collection efficiency and high temperature durability are preferable, if not the only, candidates for hot-gas filters [267]. Materials that exhibit competent feasibility have been listed in Table 18.

Zhong et al. cleverly developed a self-regeneration system of the vertical ceramic filter (multichannel tubular Al₂O₃, pore size: 4.0 μm, and porosity: 0.33) for removing organic aerosols from furnace flue gas [262]. As illustrated in Fig. 54, particles will deposit on the membrane and form a fouling layer, the permeation flux therefore drops; as the filtration process goes on, the layer becomes thicker and starts to fall down under the effect of increasing gravity, the membrane surface is then regenerated and the permeation flux recovers. Even if the sizes of particles are smaller than the pore size of ceramic membranes, the depth filtration mode could still capture the particles after the collisions with individual air molecules. Meanwhile, small particles could join during

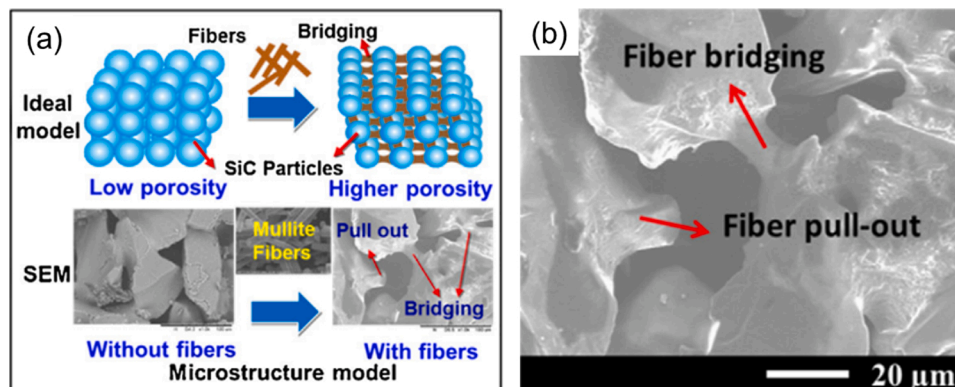


Fig. 45. (a) Schematic of the incorporation of mullite fibres into the porous SiC; (b) SEM image of the SiC porous ceramics containing 4% mullite fibres. Reproduced with permission [236]. Copyright 2016, Elsevier B.V.

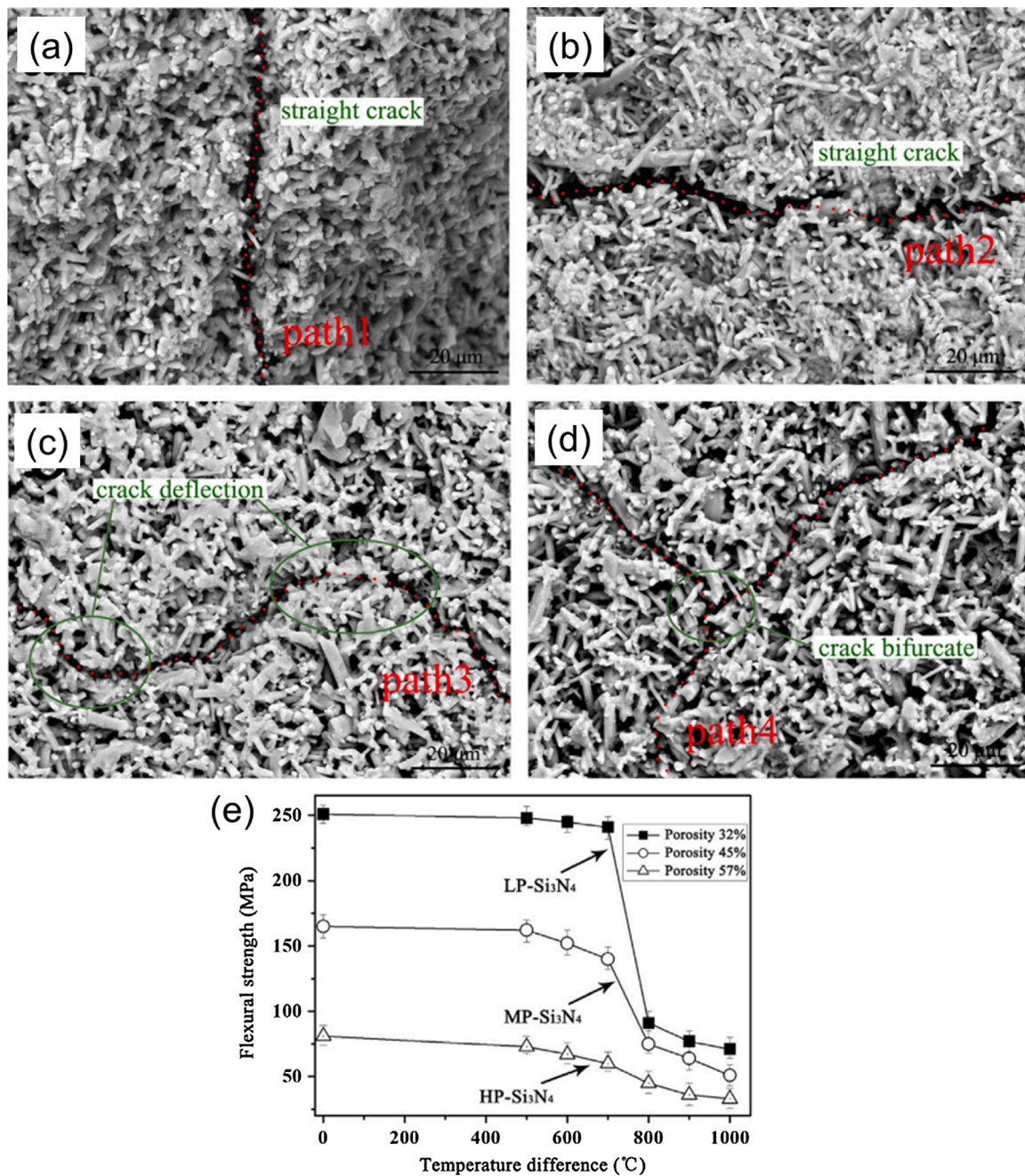


Fig. 46. SEM images of fracture surface after a single thermal shock at $\Delta T = 1000^\circ\text{C}$ for Si₃N₄ with porosity of (a, b) 32 %, (c) 45 %, (d) 57 %. The crack paths were marked by dashed lines. (e) Flexural strength as a function of quenching-temperature difference for Si₃N₄ with different porosities (LP: low porosity, MP: medium porosity, HP: high porosity). Reproduced with permission [240]. Copyright 2015, Elsevier B.V.

the transportation to form larger ones and be arrested by the filter. This mechanism leads to a collection efficiency higher than 98.5 %, with little change happened to the flexural strength, pore size distribution, and microstructure of the ceramic membranes after a long-term operation.

4.1.2. Diesel particulate filters (DPFs)

To meet the ever-stringent vehicle emission regulations, diesel particulate filters (DPFs) for trapping unburning carbon-based particulate matter (PM) in the diesel exhaust demands filters with low pressure drop, high filtration efficiency, high strength, and good thermal shock resistance. In this regard, porous ceramics with high porosity, narrow pore distribution, good pore connectivity, and large specific surface area are highly promising [7]. Currently, the honeycomb wall filters with openings in the millimetre range are the most used materials for DPFs.

Indeed, they have demonstrated higher efficiency than foam-like filters (Fig. 55) which suffer from more pressure drops. [6,268].

Dejneka et al. developed porous niobite ceramics using partial sintering as the porous particulate filter for diesel engines [269], and investigated its filtration mechanism, as shown in Fig. 56a. The particulates from the exhaust gas flow were captured by the walls of the porous ceramic substrate, and the high porosity of the filter ensured a reduction of the backpressure on the engine. The filters that impeded by accumulated soot could be regenerated after removing them either through electrical heater, post-injection of fuel into the exhaust stream, or by continuous regeneration of the catalysis.

SiC and Cordierite are considered a the most popular materials for particulate filter in diesel boilers, for their high melting temperature, good heat transfer ability, low thermal expansion, high hardness and

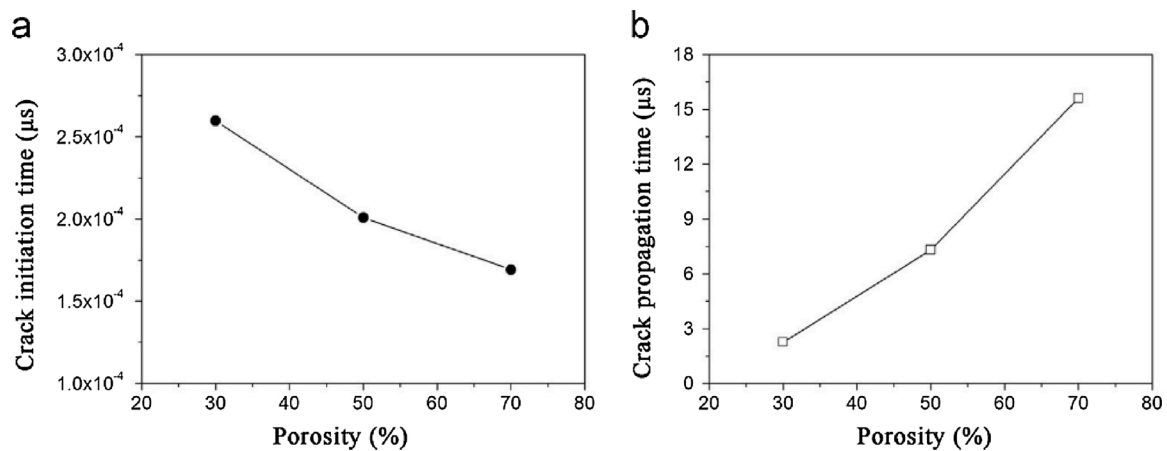


Fig. 47. A novel model that couples the X-FEM technique and thermal-mechanics fracture mechanism for analysing (a) crack initiation time and (b) crack propagation time as a function of porosity in porous Si_3N_4 that caused by thermal shock from 1000 °C to room temperature. Reproduced with permission [240]. Copyright 2015, Elsevier B.V.

high strength [270]. Park et al. fabricated porous cordierite pellets through direct foaming, and they found that the pressure drop and particle loading rate of their porous pellet filters exhibited superior filtration efficiency to nonporous ones, and small particles were also collected within the pores of the pellet filters (Fig. 56b) [271].

4.1.3. Water treatment

The microbiological quality of water has drawn a lot of attention since millions of people suffer from water-related disease every year. This demands the development of water treatment approaches. Porous ceramic water filters that generally made from diatomite or clay with porosity in the range of around 30–40% and pores in the micrometre scale can be a dependable option, as they have been proven effective in blocking bacteria and suspended solids from point-of-use (POU) water [272,273].

Although the filters could remove over 97 % of pollutant in water, to further improve the filtration efficiency and ensure the elimination of bacteria, physical filtration can be combined with metallic disinfection mechanism, which allows for in-situ clean of bacteria [273]. Silver nanoparticles (nAg) or silver nitrate (AgNO_3) added onto the porous ceramic filters could act as antimicrobial agent which removes microbial pathogens such as coliform [274], or *Cryptosporidium parvum* [275], but do not affect the nature of the water. As shown in Fig. 57, the porous ceramics are made as disc-shape Ag-containing filter for point-of-use drinking water purification [276]. However, the shortcoming is that saline, hard, or acidic water might damage the integrity of silver incorporation and thereby reduce the filter lifespan [277]. It has been found that silsesquioxane (poly(trihydroxysilyl) propyldimethyloctadecyl ammonium chloride (TPA)) [278], and chitosan [279], can be a viable and economical alternative to noble Ag. A higher bacterial reduction efficiency and lower price of TPA incorporated into ceramic water filters could benefit the manufacturers. Chitosan as a promising natural coagulant can be used as a pre-treatment for ceramic water filters, to create a multi-barrier system, and then improve the capability of

porous ceramic filters for removing micro-organisms from water. However, the release of these antibacterial compounds might have long-term health effects, which needs further investigations.

Apart from PoU water treatment, ceramic filters can also be extensively used for wastewater treatment and seawater desalination [280], which are directly or indirectly related to energy saving and energy production while protecting the environment. Phosphorus from lake sediment results in eutrophication of water bodies, which is a sign of serious lake water pollution. To restore the lake ecosystem, an in-situ adsorption for lake sediment of phosphorus was obtained by incorporating a nano- TiO_2 film or submerging macrophytes on porous ceramic filter media (PCFM), and an impressive phosphorus removing rate up to 46.7 % had been reported [281,282]. The PCFM containing ecological environment compositions is very effective to reduce the P release in lake sediment, without producing secondary pollution. Additionally, Zhang, et al. have demonstrated the utilization of combined porous ceramic filters with a UV system for marine bacteria inactivation and plankton removal in seawater [283]. As a result, no marine bacteria was detected after treatment of 20 L ceramic filter and UV radiation at $1.3 \times 10^4 \mu\text{Wscm}^{-2}$, 91.9 % of plankton was removed by a 80 L ceramic filter at a flow rate of $70 \text{ m}^3 \text{ h}^{-1}$ and UV radiation of $1.3 \times 10^4 \mu\text{Wscm}^{-2}$. Meanwhile, a 20 L ceramic filter can run continuously for 5.3 h at a flow rate of $15 \text{ m}^3 \text{ h}^{-1}$ before the pressure dropped to 0.195 MPa, demonstrating great feasibilities for onshore ballast water treatment.

As most of the existing filtration applications do not required an accurate control over the microstructure of the material, the designing of the filtrations system that leads to high efficiency and low cost has therefore been the top priority. However, in the future, attentions are likely to be given to emissions of ultrafine particles due to the ever increasing stringent emission regulatory control around the world [109]. The capability of capturing ultrafine dusts smaller than $0.1 \mu\text{m}$ (PM 0.1) is emerging in high demand, which requests research for the tight control of pore sizes and pore arrangements during the fabrication stage by choosing the proper strategy. Meanwhile, a smooth surface of

Table 14

A comparison of the mechanical properties of porous Si_3N_4 with various porosities. Reproduced with permission [243]. Copyright 2014, Elsevier B.V.

	Porosity (%)	Fracture strength (MPa)	Fracture toughness (MPa $\text{m}^{1/2}$)	Young's modulus (GPa)	Poisson's ratio	Thermal expansion coefficient ($\times 10^{-6}/^\circ\text{C}$)	R (°C)	R'''' (μm)
Sample 1	32	250 ± 10	2.11 ± 0.05	270 ± 5	0.24	2.75	252	46
Sample 2	37	230 ± 8	3.53 ± 0.03	220 ± 3	0.23	3.28	245	153
Sample 3	42	115 ± 11	1.84 ± 0.04	120 ± 5	0.22	3.54	210	164

Table 15

A summary of thermal conductivity, porosity, and the associated fabrication process of different porous ceramics.

Materials	Porosity (%)	Thermal conductivity at room temperature ($\text{W m}^{-1} \text{K}^{-1}$)	Fabrication strategy	Ref.
Al_2O_3	76.21	0.495	Sacrificial template	[252]
Al_2O_3	85–95	0.05	Direct foaming	[182]
Al_2O_3	42	0.14	Sacrificial template	[14]
Diatomite	84.5	0.097 (200 °C)	Direct foaming	[190]
Glass	~80	0.36	Direct foaming	[207]
Kaolin-based ceramics	>90	0.054	Direct foaming	[253]
Mullite	61.1–71.7	0.467–0.378	Partial sintering	[254]
Mullite	85–91	0.38–0.23	Freeze casting	[136]
Mullite	65.32–83.02	0.42–0.28 (1100 °C)	Direct foaming	[191]
Si_3N_4	80.5	0.084	Freeze casting	[137]
SiBCN	–	0.4–1.8	Sacrificial template	[94]
SiC	55.5–76.1	0.74–0.14	Sacrificial template	[116]
SiC	94.9–97.5	0.183–0.089	Direct foaming	[206]
SiC	94–97	0.14–0.61	Freeze casting	[153]
Y_2SiO_5	79.6	0.228	Direct foaming	[197]
Y_2SiO_5	60.2–87.1	0.513–0.126	Direct foaming	[196]
Y_2SiO_5	62–71	0.07–0.22	Freeze casting	[156]
Yb_2SiO_5	79.1	0.168	Freeze casting	[157]
Yb_2SiO_5	82.15–85.65	0.132–0.117	Freeze casting	[158]
YSZ	87.9–88.5	0.027–0.018	Sacrificial template	[130]
YSZ	62.9–77	0.141–0.090	Sacrificial template	[255]
YSZ	75.9	0.06	Sacrificial template	[248]
ZrC	85	0.94	Direct foaming	[209]
ZrO_2	46–18.3	0.63–1.88	Partial sintering	[22]
ZrO_2	54	0.16	Sacrificial template	[14]
ZrO_2	97.9	0.027	Direct foaming	[199]

the porous filter is preferable, as rough surfaces may lead to stronger interaction with foulants, which causes low durability and high maintenance cost for the filters [262].

4.2. Catalyst support

Catalysis has received increasing academic and industrial interest, as about 90 % of chemical processes involve at least one or more catalytic steps. Tremendous efforts have been poured onto the development of new catalytic processes, in order to achieve high selectivity, low energy input, low waste generation, and long-term stability [60].

Traditional catalysts supported by granular or packed powder bed (porosity in the range of 0.3–0.6) have been found problematic in applications like water purification or industrial emission treatment, due

to their low mechanical strength, high pressure drop and gas dynamic resistance, which restricts the activity and selectivity of the reaction [284]. Moreover, the powders are difficult to be collected or removed from the reaction media, leading to a complicated, uneconomical recycling process, and hindering large scale applications [285]. To overcome these drawbacks, the effective catalyst can be immobilised on a highly permeable porous substrate as support [286]. These supports are generally having a porosity from 0.6 to 0.95, and are required to provide high specific surface area and effective heat and mass transfer, for improved efficiency [287].

Porous ceramic-based catalyst supports have attracted a lot of interests, for their low thermal expansion coefficient, high mechanical strength, thermal shock resistance, chemical durability, and refractoriness [288], which, in turn, endow them a series of advantages: (1) The ceramic foam can be pre-shaped to match complicated reactor configurations, thus simplify the reactor loading; (2) The lower pressure drops compared with packed beds lead to higher efficiencies and low-contact-time in operation; (3) The high specific surface areas provide improved mass transport, good anchorage and dispersion of the active phase, high accessibility of the reactants to the active sites, which eventually give rise to an increased reaction effectiveness than pellet catalysts; (4) The enhanced radical convection with improved heat transfer, enables better feasibility for highly exothermic or endothermic reactions. (5) The long-term stability in oxidising, neutral, and reducing atmosphere at high temperatures makes them unique as compared with polymer or carbon material-based catalyst support [6,54,60,64,104,287,289,290].

Krivoshapkina et al. fabricated $\text{CuO-Co}_3\text{O}_4\text{-CeO}_2/\text{kaolinite}$ and $\text{CuO-Co}_3\text{O}_4\text{-CeO}_2/\text{cordierite}$ catalysts by a surface self-propagating thermal synthesis (SSTS) method, using porous kaolinite (porosity 40 %) and cordierite (porosity 25 %) as the ceramic support, and with the active ingredient uniformly distributed on the surface of the substrate [284]. In this configuration, the active ingredients exhibited high activity, whilst the support had no negative effects on the entire system. As shown in Fig. 58, they examined the performance of their system in the oxidation of carbon monoxide, and a significantly improved catalytic activity has been achieved.

It has been found that the optimisation of structures of the catalytic support is of more importance than purely increasing the intrinsic activity of catalysts [291]. Therefore, in practice, tailoring the porosity with narrow pore size distribution, uniform pore structure and volume is more effective and desirable for many catalytic applications [292]. Additionally, the complex hierarchical pore systems consisting of continuous macro-, meso-, and micropores have been shown to provide a combination of high specific area, good accessibility to the catalytic sites, meanwhile maintain good mechanical strengths [289,293,294].

It is worth noting that the weak interaction between the host and catalyst phase (normally noble metal) may cause poor activity and short durability. To overcome this issue, proper surface modifications can be introduced to improve the bonding between the support host and catalysts, for better catalytic efficiency. Han et al. obtained an improved connection between an hierarchically porous SiC support and the noble metal nanoparticles by applying a N-containing composition (N–C) on the surface of SiC ultrafine fibres [295], as presented in Fig. 59a. They have shown that the resulting N–C/SiC fibres obtained homogeneous and compact distribution of g- C_3N_4 (Fig. 59b–e), suggests superb affinity of N–C with noble metals, and as a result, enhanced the suitability of the catalyst support for electrocatalytic reactions, especially in harsh environments.

In this section, porous ceramics supported catalyst for environmental remediation and hydrogenation process are displayed, the special role of porous ceramic in catalyst support has been critically reviewed. Almost every study of porous ceramics claims that the material they obtained shows great potentials as a catalyst support, however, only a few of them has attempted to realise the intended functions. Here, we have summarised commonly used catalyst supports including fully specified

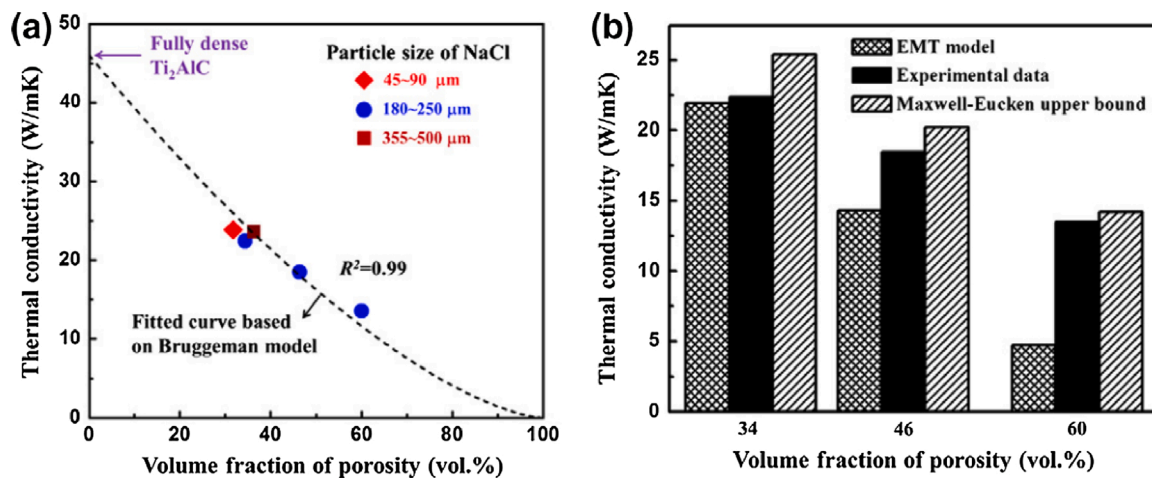


Fig. 48. (a) Room temperature thermal conductivity of Ti_2AlC as a function of porosity and pore size; and (b) The comparison of experimental results with theoretical EMT and Maxwell-Eucken upper bound models. [129] Copyright 2012, Elsevier B.V.

fabrication methods, pore features, loading materials and realised applications in Table 19, which constitutes the basic selection criteria for choosing the right process and materials for specific applications.

4.2.1. Photocatalyst for environmental remediation

The agent-containing ceramic filters in 4.1.3 show capability of removing bacteria and suspended solids in the water. However, the growing concerns in water and air contamination from organic pollutants have led to a rising research interest in the development of new photocatalytic processes. TiO_2 as the most widely studied photocatalyst provides superb photocatalytic properties, biocompatibility, low toxicity and adequate photochemical stability. However, nano-sized TiO_2 powders are difficult to be separated from the reaction media, and their poor thermal stability and low adsorption capability limit their wide uses [302]. Porous ceramic supported TiO_2 catalysts are therefore widely developed for the water treatment by degradation of pollutants.

Du et al. deposited TiO_2 thin films onto microporous Al_2O_3 (porosity

of 60.4–79.5% and pore size of 180–315 μm) by using the sol-gel dip-coating method, for uses as photocatalyst [286]. They found a linear relationship between the specific surface area and the amount of TiO_2 deposited, which had a direct effect on the final photocatalytic performance. Meanwhile, the regularity of the pore structure was of great importance, since distorted pore channels could result in uneven distribution of the coating and reduce the contact area between incident light and the catalysts. In their study, a good adhesion of the TiO_2 coating on the Al_2O_3 support was claimed, and a photocatalytic efficiency up to 79.52 % was reported, which is comparable to that of TiO_2 /water suspension [286]. Importantly, the cumbersome recycling process of the loose powder from the suspension was omitted, as an important advantage of practicability. Wan et al. prepared porous SiO_2 -supported TiO_2 catalysts using the surface absorption method [285], and achieved a core-shell structure (Fig. 60a-c). This structure showed an outstanding photocatalytic property, with the highest degradation efficiency of 92.07 % for Methyl Orange (MO) under 30 min

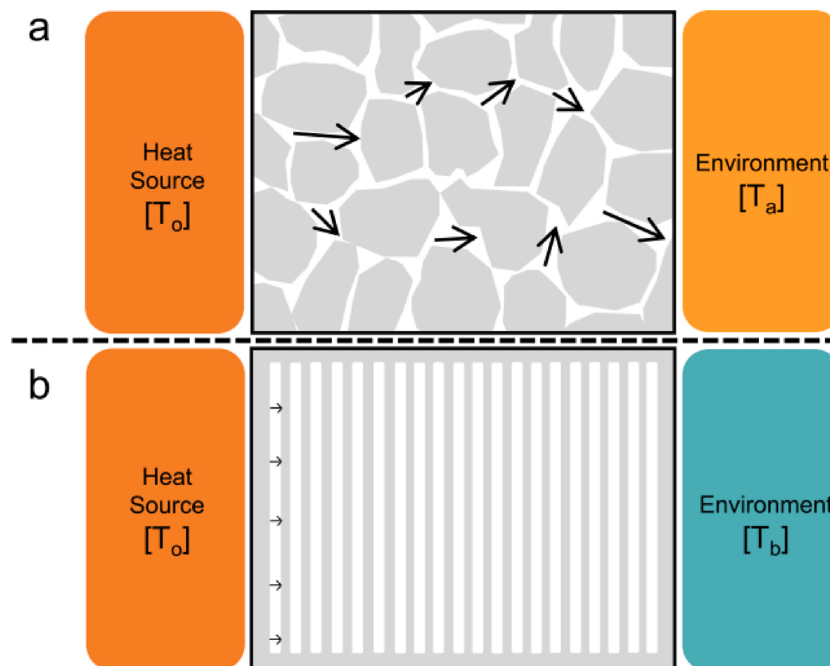
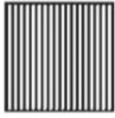


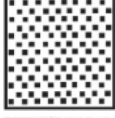



Fig. 49. Schematic of heat transfer in porous ceramics with: (a) randomly aligned porous microstructure, and (b) closed channels that perpendicular to the heat flow. $T_0 > T_a > T_b$. Reproduced with permission [5]. Copyright 2014, Elsevier B.V.

Table 16

Five basic effective thermal conductivity models for the two-component porous ceramics. [191] (v and K represent the volume fraction and thermal conductivity, respectively).

Model	Structure schematic	Effective thermal conductivity equation
Parallel model		$K = v_1 k_1 + v_2 k_2$
Series model		$K = \frac{1}{v_1/k_1 + v_2/k_2}$
Maxwell-Eucken 1 ($k_1 =$ continuous phase, $k_2 =$ dispersed phase)		$K = \frac{v_1 k_1 + v_2 k_2 \frac{3k_1}{2k_1 + k_2}}{v_1 + v_2 \frac{3k_1}{2k_1 + k_2}}$
Maxwell-Eucken 2 ($k_1 =$ dispersed phase, $k_2 =$ continuous phase)		$K = \frac{v_2 k_2 + v_1 k_1 \frac{3k_2}{2k_2 + k_1}}{v_2 + v_1 \frac{3k_2}{2k_2 + k_1}}$
EMT model		$v_1 \frac{k_1 - K}{k_1 + 2K} + v_2 \frac{k_2 - K}{k_2 + 2K} = 0$

UV irradiation. Similarly, Vargova et al. deposited TiO_2 thick films on reticulated Al_2O_3 foams [296]. Their samples exhibited strong photocatalytic activity, about 75 % of the photocatalytic activity of the corresponding powder dispersion, but with no measurable release of the deposited catalyst. This sort of strategy allows for the generation of photocatalyst with good reproducibility, easy handling, thus is more suitable for practical uses for the degradation of various pollutants and environmental remediations.

Zhu et al. developed porous TiO_2 membrane with an enhanced ozonation water treatment capability, by using the dip-coating technique [300]. The macroporous TiO_2 -nanorods-assembled membrane (MPTM) (200–400 nm in diameter and 5 μm long) was then uniformly coated with a mesoporous Ti-Mn layer (thickness 100 nm, pore size 10 nm), forming a hierarchical porous structure (Fig. 61a). This combined membrane-ozone system substantially improved the removal rates for COD_{Cr} , dye and Aniline (Fig. 61b,c), because the hierarchical membrane possessed high surface areas which created more active sites for catalytic ozonation. Meanwhile, the improved mass transportation within this hierarchical porous catalytic membrane (HPCM) increased the reaction probability with ozone, radicals, and organic pollutants.

In short, three basic factors are required for a good porous ceramic-supported TiO_2 photocatalyst: (1) The strong anchorage of TiO_2 onto the surface of the support material; (2) Open-cell foams with high geometric surface areas to allow for a close exposure and interaction of the TiO_2 active phase with the reactant; and (3) Highly porous ceramic support (porosity > 90 %) with large void allows the UV radiation to access deeply through the media, offering the maximum irradiation [293,303].

4.2.2. Micro-reformer for hydrogenation process

The continuous operation of electronic devices demands the development of portable electrical power sources. Micro-fuel cell due to its higher energy density than existing lithium ion batteries has thus attracted a lot of attentions. The catalytic conversion of hydrocarbons to supply hydrogen for fuel cells or other portable power sources is believed to be a safe and efficient approach. In this regard, on-site hydrogen production via steam reforming has been intensively studied

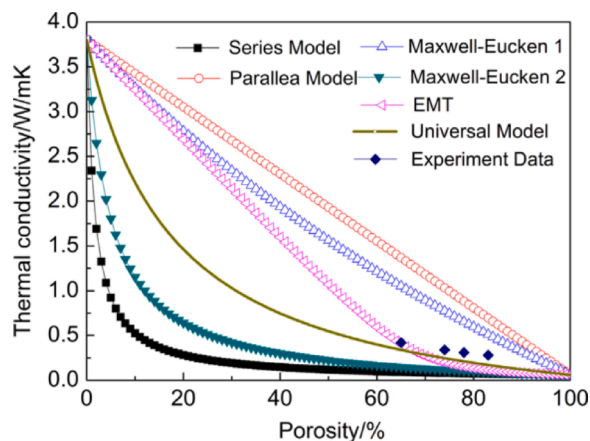


Fig. 50. Experimental thermal conductivity as a function of porosity at room temperature, against results obtained by using different models. Reproduced with permission [191]. Copyright 2016, Elsevier B.V.

[304]. Owing to the promising high external surface areas, low pressure drop, large heat transfer capability, and high temperature stability, pre-structured porous ceramic catalyst supports exhibit great potentials for this sort of highly endothermic processes [305].

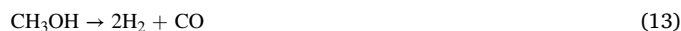
Hoffmann et al. developed nanoporous SiC (with pore size in the range of 11–18 nm, specific surface area 223–328 $\text{m}^2 \text{g}^{-1}$, pore volume in the range 0.4–0.5 $\text{cm}^3 \text{g}^{-1}$) as the support of Ni-containing catalyst systems, KPK1ox, for CO reforming of methane, and they recorded a conversion rate up to 22 % [298]. An oxidation layer of SiO_2 formed on the SiC core was reported to offer better stability for the support. Kim created porous ceramics (typically composed of 40 % Al_2O_3 and 55 % SiO_2 , porosity of 71 %, pore size ranging from a few to $\sim 100 \mu\text{m}$) with large surface areas and good thermal stability, and they further evaluated their performance as the Cu/ZnO catalyst support for steam reforming of methane [297]. The H_2 generated from the reformer was directly supplied to power the polymer electrolyte membrane (PEM) fuel cell, as demonstrated in Fig. 62. A methanol conversion over 93 % with a thermal efficiency of 76.6 % was achieved, which is enough to run a 4.5 W PEM fuel cell.

In this process, two reactions are involved:

Methanol steam reforming reaction:



Methanol decomposition:



As the methane reformer requires additional power to achieve the required temperature for the steam reforming, a combination of hybrid solar energy conversion system with fuel cell technology thus provides a controllable and flexible power supply. In this way, H_2 can be instantaneously converted to electric power, meanwhile, this offers solution to the problem of unbalanced power supply from the sunlight between day and night. The role of the so-generated porous ceramics in this process is acting as the solar-powered catalytic media to convert alcoholic biofuel (e.g. methanol) to H_2 -rich gas mixture (up to 75 % H_2 content), which can be directly used to power the fuel cell. Hotz et al. developed a solar to electricity energy system that combines catalytic particle-containing ceramic reactor with fuel cells using foam-like $\text{ZrO}_2/\text{Ce}_{0.5}\text{Zr}_{0.5}\text{O}_2$ ceramic, as shown in Fig. 63a,b [306]. The new system could convert methanol to H_2 gas mixture. With low concentrations of CO (less than 0.2 %), the poisoning of the fuel cell catalyst had been avoided, and the fuel-to-electricity efficiency of this system was above 50 %, indicating that the porous ceramic reactor in this study successfully fulfils the requirement.

In practical application, the emission of CO over 10 ppm may

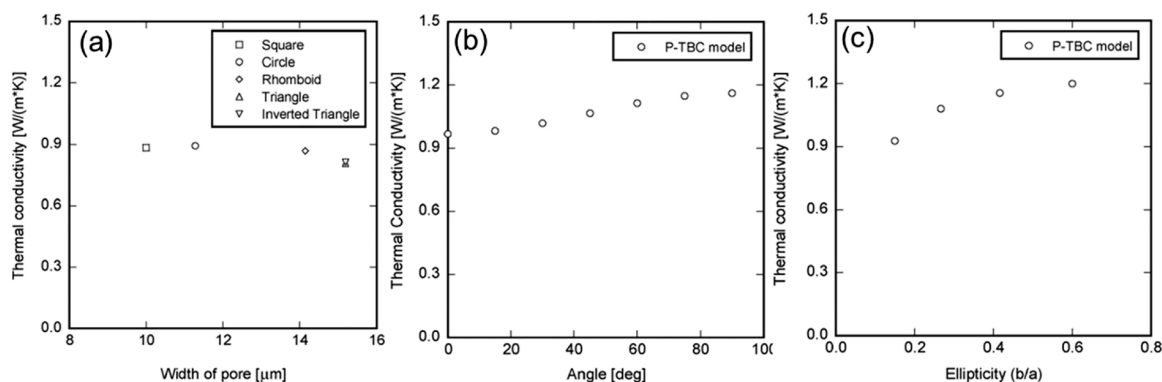


Fig. 51. Influence of pore geometry on the thermal conductivity of porous TBCs. (a) Pore shape, (b) Tilt angle, and (c) Ellipticity. Reproduced with permission [256]. Copyright 2016, Elsevier B.V.

deactivate the anode catalysts of the fuel cell [297]. To avoid the CO poisoning issue from steam reforming of liquid hydrocarbon, Christian et al. fabricated macroporous SiC monolith (volume surface areas $7.4 \times 10^7 \text{ m}^2 \text{ m}^{-3}$, porosity of 74 %) microreactor via a customised replica template method for on-site H_2 production by decomposing ammonia [118]. By applying Ru as the catalyst at temperatures between 450 and 1000 °C, 54 sccm of H_2 could be obtained from a 36 sccm entering stream of NH_3 , indicating a conversion of > 99.9 %. Meanwhile, the undesirable catalyst coking that occurs during the reforming of hydrocarbons in other systems was avoided by using these high temperature, compatible, porous ceramic microreactors.

Aran et al. developed a porous Al_2O_3 multiphase membrane reactor (active surface area: $\sim 73 \text{ m}^2 \text{ g}^{-1}$) for the gas-liquid-solid (G-L-S) micro-reaction technology (Fig. 64a,b), via the fabrication, catalyst deposition and surface modification steps [301]. The capability of the reactor was performed by hydrogenation of nitrite (NO_2^-) ions under Pd catalyst in an aqueous phase. The conversion rate remained high and stable when the concentration of the H_2 decreased (Fig. 64c), which demonstrated that this reactor provided good efficiency and allowed for operating at low partial pressures of reactants. The configuration, microstructure, and surface hydrophobisation of this membrane catalyst support can be further optimised to improve its performance.

It can be asserted that catalyst support has been one of the most widely used applications of porous ceramics. Despite great efforts have been made to increase the understanding of porous ceramics as catalyst support, additional work is required to discover their influence on the different catalytic processes, typically the heat and mass exchange between porous ceramic and the supported active catalyst phase, which can be realised by a combination of experimental study and thermodynamic modelling. Impacts of the microstructural features such as porosity, pore size, pore morphology, and pore distributions should be taken into consideration as well. Additionally, the approach to improve the anchoring and dispersing of active catalyst on the surface of supports

still needs fundamental understanding [60]. One possible solution could be the dopant on the porous ceramic matrix, which is believed to provide high chemical interaction with the catalyst phase deposited, leading to the formation of highly active and stable catalyst.

The development of porous ceramic catalyst support should keep up with the progress of catalyst. More effort can be made to improve the catalyst utilisation rather than increasing their intrinsic activity. Engineering the affordable, efficient and long-term reliable porous ceramics with optimised pore size distributions in the nanoscale for loading novel metal-organic frameworks (MOF) materials are expected to pave the way to more advanced energy and environmental applications, including hydrogen storage, gas purification, gas separation, and supercapacitor.

4.3. Energy storage and conversion media

Energy storage and conversion process generally comprises a series of complex electrochemical reactions. In these processes, porous ceramics with intrinsic thermal stability, chemical inertness, and permeability exhibit competent capability as components in concentrated solar power, fuel cell, and batteries. Furthermore, the possibility of coupling them with other chemicals could lead to enhanced efficiencies.

4.3.1. Solar energy absorption and conversion

The energy conversion from solar power to other forms of energy has not been well-demonstrated due to the limit of conversion efficiency. In this regard, using solar-heated air as a heat transfer medium could lead to a breakthrough. A concentrated solar power (CSP) plant captures solar power by concentrating the irradiation from sun directly onto a receiving surface which transfers the absorbed heat to mechanical work or electrical energy. Unlike other renewable energies such as wind or photovoltaics, dispatchable power can be provided by solar thermal power systems, by means of thermal energy storage or hybridisation

Table 17

Porosity, grain size, room-temperature thermal conductivity, and compressive strength of porous yttria-stabilised zirconia (YSZ) ceramics fabricated with different solid loading and sintering temperatures. Reproduced with permission [248]. Copyright 2010, Springer Nature Switzerland AG.

Sample	Solid loading (vol. %)	Sintering temperature (°C)	Porosity (%)	Grain size (μm)	Room-temperature thermal conductivity ($\text{W m}^{-1} \text{K}^{-1}$)	Compressive strength (MPa)
A	10	1350	75.9 ± 1.6	1.28	0.06 ± 0.04	3.04 ± 0.13
B	10	1400	74.2 ± 1.4	1.31	0.07 ± 0.02	7.92 ± 0.52
C	10	1450	72.4 ± 0.2	1.35	0.10 ± 0.06	9.64 ± 1.45
D	10	1500	66.0 ± 1.1	1.55	0.20 ± 0.09	13.15 ± 0.48
E	10	1550	65.6 ± 0.4	1.78	0.17 ± 0.06	24.92 ± 2.37
F	15	1350	71.8 ± 1.4	1.30	0.08 ± 0.01	4.12 ± 0.27
G	15	1400	65.0 ± 2.3	1.33	0.18 ± 0.01	9.22 ± 1.75
H	15	1450	63.1 ± 2.6	1.46	0.27 ± 0.06	11.19 ± 1.48
I	15	1500	51.5 ± 4.1	1.57	0.42 ± 0.11	10.66 ± 0.53
J	15	1550	56.4 ± 3.0	1.62	0.34 ± 0.06	29.01 ± 6.76

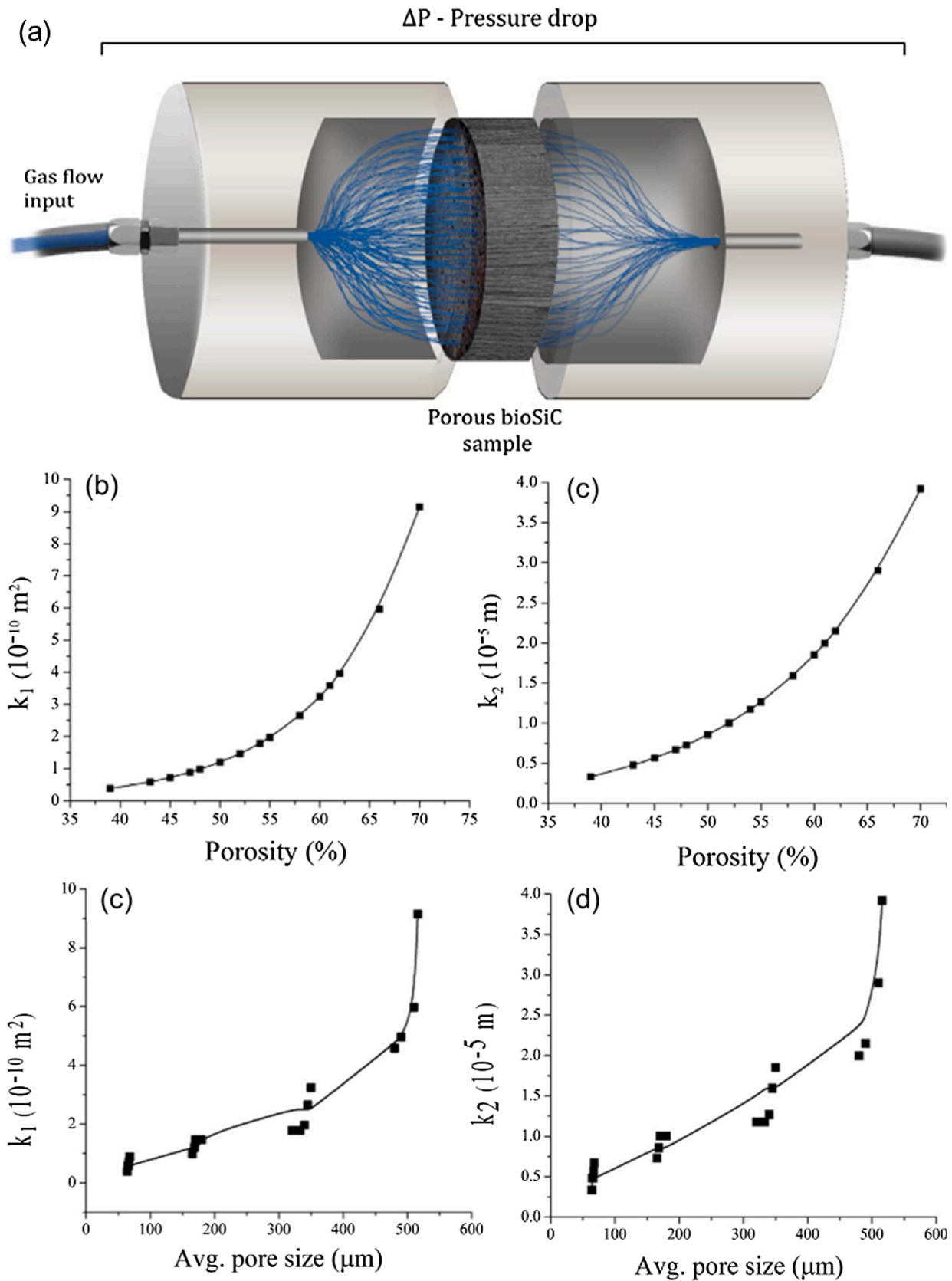


Fig. 52. (a) Schematic set-up for the measurement of gas permeability. Reproduced with permission [68]. Copyright 2016, Elsevier B.V. Plots of Darcian permeability and non-Darcian permeability constant as a function of (b, c) porosity and (d, e) average pore size of porous alumina compacts. Reproduced with permission [235]. Copyright 2015, Elsevier B.V.

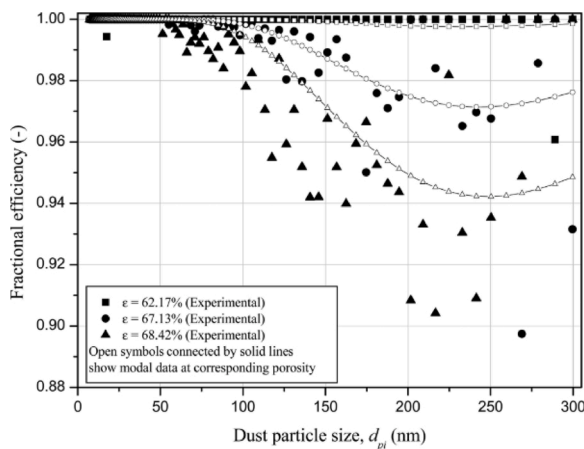


Fig. 53. Modelling and experimental result of particle collection efficiency vs. dust particle size for filters with different porosities ($\epsilon = 62.17\%$, 67.13% , and 68.42%). Reproduced with permission [109]. Copyright 2013, American Chemical Society.

with conventional fuels [307]. Ceramic foams with large specific areas, tortuous flow path, and excellent thermal shock resistance, are ideal materials for the absorber of volumetric solar-air receivers in CSP plants (Fig. 65a,b) [308]. As shown in Fig. 65c, ceramic honeycombs were used as the absorber elements, and they were heated up by concentrated solar radiations. The heat generated was transferred to air with temperatures up to more than 1000°C , for feeding the steam generator of a Rankine-Cycle [309].

It is believed that the temperature distribution in the key component – solar receiver is of great importance to guarantee the proper operation of a CSP plant [308]. Several thermal analyses have been carried out to investigate the effect of the microstructural features of the absorber material on the performance of a CSP [310–312]. The optimisation studies have indicated that in terms of thermal efficiency, a cell size of 1–2 mm with the highest possible porosity should be selected as solar receivers, and a second layer can be applied to improve the mechanical stability. Meanwhile, a thickness of absorber in the range of 10–30 mm is sufficient to ensure a good thermal performance [307].

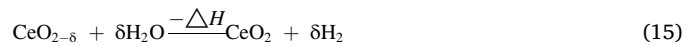
Solar energy can be efficiently stored by the above-mentioned CSP

plant, however its storage limit is just 1.5 h during the on-sun operation. To increase the storage capacity, a porous ceramic-based thermochemical storage module can be directly integrated in the CSP for H_2O and CO_2 splitting via a thermochemical redox cycle that powered by the stored heat. In such a way, the thermal energy can be entirely recovered from the reverse exothermic oxidation during the off-sun operation. Furler et al. prepared reticulated CeO_2 -based porous ceramic foams by applying the replica template technique for solar $\text{H}_2\text{O}/\text{CO}_2$ splitting (Fig. 66a,b) [313]. The CeO_2 -based reticulated porous ceramics inherently combine advantages including high volumetric radiative absorption, rapid reaction rates, and high mass loading of reactive material, since they could act as the reactive materials themselves. The reactions they may experience can be represented by [314]:

High-temperature reduction:



Low-temperature oxidation with H_2O :



Low-temperature oxidation with CO_2 :



The maximum $\eta_{\text{solar-to-fuel}} = 3.53\%$ was determined when specific O_2 evolution was $2.256 \pm 0.08 \text{ mL g}^{-1}$, and specific CO production was $4.56 \pm 0.12 \text{ mL g}^{-1}$ at 3.8 kW , which is four times greater than previously reported values [313].

Agrafiotis et al. developed porous heat-exchange modules with thermochemical redox oxide pairs coated, such as $\text{Co}_3\text{O}_4/\text{CoO}$ and $\text{Mn}_2\text{O}_3/\text{Mn}_3\text{O}_4$ with a wide redox temperature range of $800\text{--}1000^\circ\text{C}$ [315]. As shown in Fig. 67a,b, the endothermic reduction of the oxides was triggered by solar heat received during the on-sun operation, whilst the thermal energy was recovered by the reverse exothermic oxidation reaction during the off-sun operation. The highly porous ceramic with monolithic honeycomb or reticulated structures provided high geometric surface areas, good gas-solid contact, high accommodation capacity for high gas flow rates with low pressure drops, facile deposition of functional coatings, and good structural integrity maintenance after reaction cycles. These advantages are highly desirable not only for solar

Table 18
Porous ceramic suitable for application in hot-gas filters.

Materials	Pore forming method	Porosity (%)	Pore size (μm)	Collection target	Permeability (m^2)	Remarks	Refs
Al_2O_3	–	33	4.0	Organic aerosols: paraffin binder, carboxylic acids, and esters	–	Removal efficiency: 98.5 %	[262]
Al_2O_3	Sacrificial template	39–70	64–516	–	$k_1: 0.38 \times 10^{-10}$ - 9.15×10^{-10} $k_2: 0.33 \times 10^{-7}$ - 3.92×10^{-7}	Potentially useful in filtration	[235]
Mullite	Direct foaming	61.1–71.7	~5	–	–	Promising candidate for hot-gas filters	[254]
Mullite- Al_2O_3	Sacrificial template	43–71	$6.0 \pm 0.3\text{--}22.0 \pm 3.5$	–	$k_1: 2.5 \times 10^{-14}$	Potential use as hot-gas filters	[266]
BioSiC	Replica template	45–72	15.7–19.2 (radial)/ 47–58 (axial)	–	$k_1: 10^{-11}$ - 10^{-12} $k_2: 10^{-7}$ - 10^{-8}	Promising hot-gas filtration application	[68]
Cordierite-bonded porous SiC	Sacrificial template	$30.1 \pm 1.2\text{--}71.7 \pm 2.6$	6–50	Airborne nanoparticles with size varying from 7 to 300 nm	–	96.7–99.9 % at fluid superficial velocity of 0.1 m/s	[109]
MDF-bioSiC/ Sipo-bioSiC	Replica template	43–57/32–75	10–20/ >100	–	–	Exhibits feasibility	[261]
SiC	Sacrificial template	44.2	14.6 (average)	–	–	Potential practicability	[237]
SiC	Partial sintering	$36.26 \pm 1.58\text{--}45.97 \pm 2.08$	$14.19 \pm 1.24\text{--}22.07 \pm 0.73$	Particles larger than $1 \mu\text{m}$	–	–	[265]

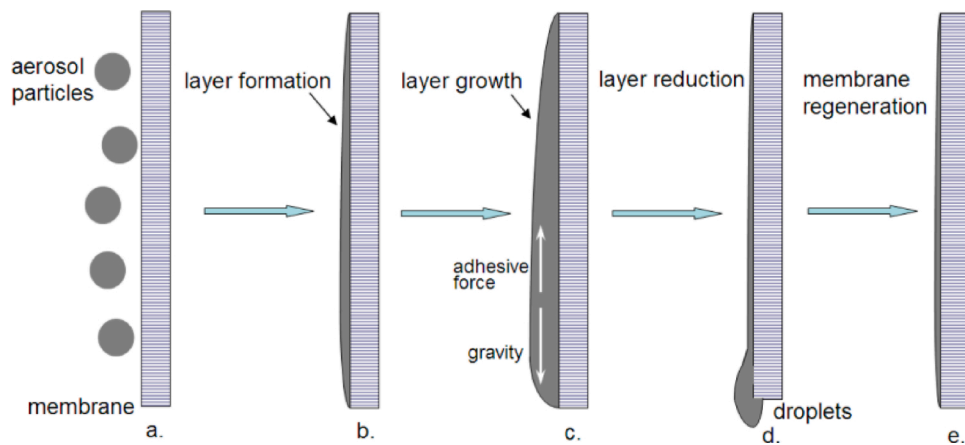


Fig. 54. Schematic of the self-regeneration process for furnace flue gas by ceramic filters. Reproduced with permission [262]. Copyright 2013, American Chemical Society.

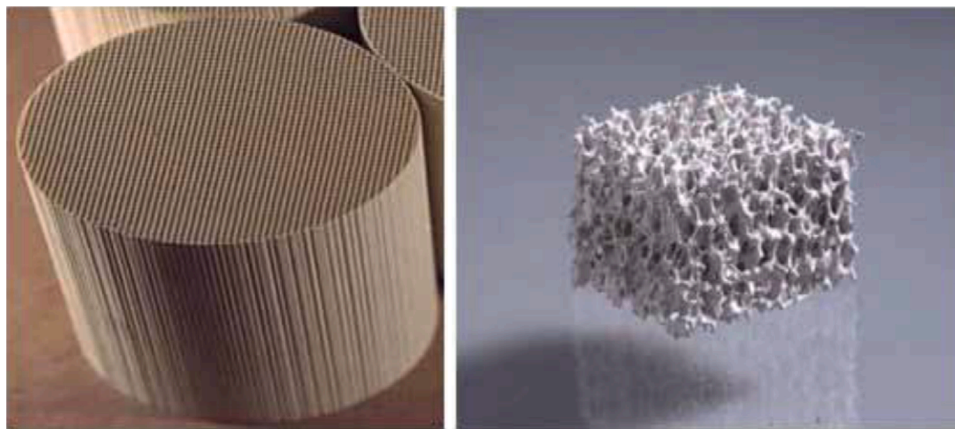


Fig. 55. Pictures of a honeycomb wall filter (left) against a foam like filter (right), used as the core element in diesel particulate filters. Reproduced with permission [268]. Copyright 2010, Hosokawa Powder Technology Foundation.

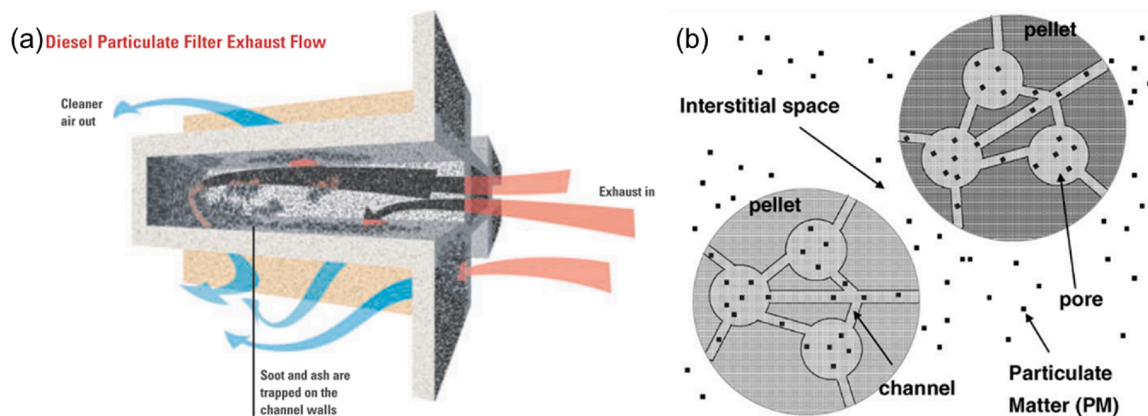


Fig. 56. (a) Schematic of wall flow particulate filter. Reproduced with permission [269]. Copyright 2011, The American Ceramic Society. (b) Mechanism of PM trapped by the pores and channels of porous pellet filters. Reproduced with permission [271]. Copyright 2007, Elsevier B.V.

irradiation receivers, but also for sensible/thermochemical heat storage media. Currently, on-going researches are focused on the manufacture of large-scale porous structures for real solar facility, as well as tailored geometric features and material properties for higher volumetric absorber efficiency [316].

4.3.2. Components in fuel cells and batteries

Fuel cells could convert chemical energy to electric energy with little pollution to the environment. According to the electrolyte used, they can be classified as polymer electrolyte fuel cell (PEFC), phosphate acid fuel cell (PAFC), melted carbonate fuel cell (MCFC) and solid oxide fuel cell (SOFC). The electrode in fuel cells is required to guide gases into and out



Fig. 57. Schematic of disc-shape porous ceramic filter containing Ag nanoparticles for point-of-use water treatment. Reproduced with permission [276]. Copyright 2013, American Chemical Society.

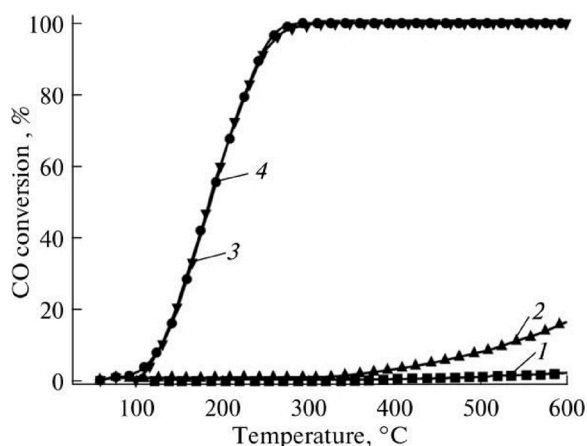


Fig. 58. Temperature dependence of the CO conversion on different ceramic membranes tested by Krivoschapkina et al. (1) Initial cordierite ceramic, (2) Initial kaolinite ceramic, (3) CuO-Co₃O₄-CeO₂/cordierite sample, and (4) CuO-Co₃O₄-CeO₂/kaolinite sample. Reproduced with permission [284]. Copyright 2015, Springer Nature Switzerland AG.

of the structure, provides large reactive surface area, and maintains strength during operation [317]. Typically, high operating temperature (over 900 °C) of a SOFC necessitates the processing of ceramic components [318]. They generally have porosities between 25–55% and continuous connection of pores on the order of 50–150 μm that are needed for the diffusion of reactants to the active reaction area. The pore characteristics should be optimised for tuneable control of the gas flow, mechanical properties, and electrochemical performance [167,319].

Larger amounts of added pores allow for more gas diffusion during the reaction at the active three-phase boundary (pore/electrode/electrolyte) regions (Fig. 68a,b). However, an increased porosity could not only lead to inferior in the mechanical properties, but also limit the reaction rate, due to excessive replacement of three-phase boundary. Therefore, an optimum amount of porosity should be used [319]. Freeze-casting exhibits great feasibilities for the fabrication of porous ceramic electrode for constructing SOFCs, as the straight and parallel pore configuration created by freeze-casting provides selective gas permeation and reduce the path length of gas phase diffusion (Fig. 68c), which is desirable for promoting the electrochemical reactions [166, 320].

Photomicrobial fuel cells are devices that transform light energy to electrical energy by using photosynthetic organisms (p-MFC) [321]. The suitability of carbon and metals as electrodes has been argued. Because carbon anode with comparatively low conductivity and inherent black colour hinders the light from getting to the microorganisms, whilst metal electrodes with low surface roughness and less well-defined pores limit the growth of biofilms. On the contrary, biocompatible porous

fluorine-doped tin oxide (FTO)-coated TiO₂ ceramic anodes with interconnected porous structure (millimetre-sized pores, as shown in Fig. 69) outperform the above-mentioned carbon or metal anodes for p-MFC uses, since the pores allow for light scattering inside and facilitate the biofilm growth. The maximum power output was improved to 24 mW m⁻², compared with 14 mW m⁻² that achieved by using carbon cloth electrode. Meanwhile, the biofilm anchored within the porous ceramics were much more stable, suggesting long-term benefits.

It has been recognised that unregulated, dendritic lithium electro-deposition during charge-discharge cycles has been the major drawback for lithium metal batteries (LMBs). To counter the dendrite formation, Tu et al. designed hybrid electrolytes by infusing conventional liquid electrolytes into nanoporous Al₂O₃ ceramic membranes (pore size: 20–300 nm) (Fig. 70a,b) [322], in an effort to stabilise the anode in a LMB. In following up tests, the rechargeable batteries with long-term stability even at high current density of 3 mAcm⁻² were obtained without any failure caused by the dendrite-induced short-circuiting. They even deduced that two fundamental benefits were originated from the use of nanoporous ceramic membranes: first, the dendrite nucleate size was constrained by the dimension of small nanosized channels; second, the nanochannels with charged walls could regulate fluid flow or rectify the ion transport, reducing the driving force for electro-convection and dendrite formation.

In these energy conversion storage applications discussed above, porous ceramics have been used as an essential component, where good mechanical stability, tuneable mass transport, and enhanced electrochemical performance are successfully obtained. However, there are fewer literatures reporting the evaluation of porous ceramics as components in energy storage and conversion applications, especially for fuel cells and batteries, compared with their applications as conventional catalyst supports. A more complete picture of potential benefits that the porous ceramics could bring into high performance fuel cells and batteries requires much effort to be fully understood.

4.4. Energy harvesting (MEMS) and sensing applications

Batteries are currently used to supply power for portable wireless electronics. However, their finite lifetime and high maintenance cost are frustrating both the manufacturers and consumers. For this reason, microelectromechanical systems (MEMS) that could scavenge energy from surrounding environment has been exploited as an alternative power source for small-scale electronic devices. Particularly, the effective piezoelectric and pyroelectric properties of ferroelectric lead-zirconia-titanate (PZT) and barium-titanate (BaTiO₃) endow them exceptional capability to harvest energy from mechanical vibrations and temperature fluctuations [323,324].

The following two Figures of Merit (FoM) can be used to assess the capability of materials for piezoelectric and pyroelectric energy harvesting, respectively:

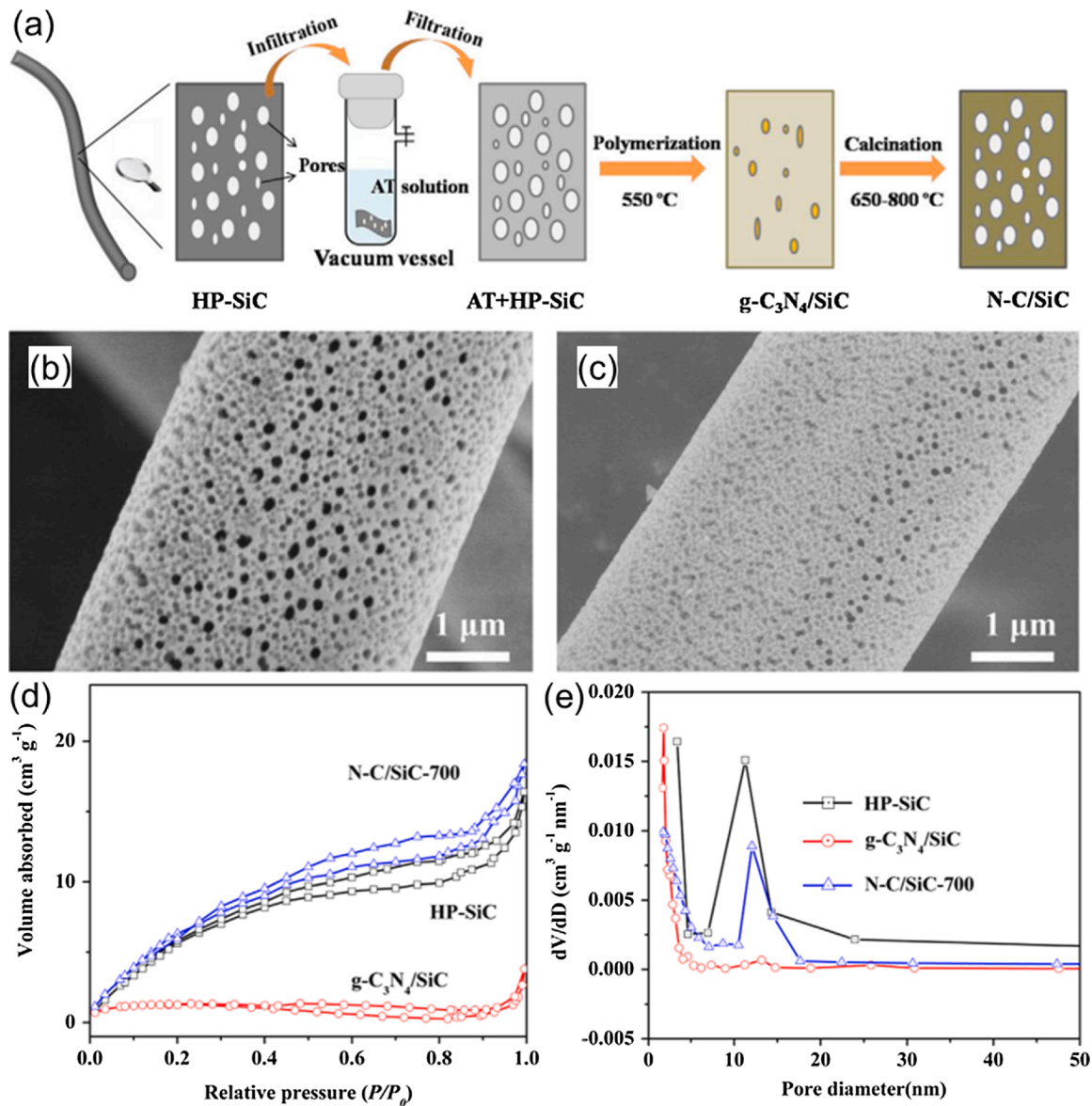


Fig. 59. (a) Schematic of the fabrication of $g\text{-C}_3\text{N}_4/\text{SiC}$ and N-C/SiC . SEM images of (b) the pristine hierarchical porous SiC (HP-SiC) fibre, and (c) the N-containing SiC (N-C/SiC) fibre. (d) Nitrogen adsorption/desorption isotherms and (e) pore-size distribution of HP-SiC, $g\text{-C}_3\text{N}_4/\text{SiC}$ and N-C/SiC-samples (N-C/SiC-700 indicates the calcination at 700°C), in which the decreases in both surface area and pore volume of $g\text{-C}_3\text{N}_4/\text{SiC}$ confirm the filling of mesopores during the impregnation. Reproduced with permission [295]. Copyright 2016, Elsevier B.V.

$$\text{FoM}_{ij} = \frac{d_{ij}^2}{\epsilon_0 \epsilon_{33}^T} \quad (17)$$

$$F'_E = \frac{p^2}{\epsilon_0 \epsilon_{33}^T \times C_E^2} \quad (18)$$

Where FoM_{ij} is a piezoelectric harvesting FoM, which demonstrates the electrical energy density under a mechanical stress, d_{ij} is the piezoelectric charge coefficient (where d_{33} and d_{31} represent the longitudinal and transverse piezoelectric charge coefficients, respectively), ϵ_{33}^T is the dielectric constant, ϵ_0 is the permittivity of free space; F'_E is the modified pyroelectric harvesting FoM that indicates the energy density under a thermal input, p is the pyroelectric coefficient, C_E is the volume specific heat capacity [139]. It can be deduced from above equations that enhanced energy harvesting capability can be achieved from materials with low relative permittivity, low specific heat capacity, high piezoelectric and pyroelectric coefficients [139]. To this end, pores are purposely incorporated into ferroelectric materials, since the entrapped air

can be considered as a low permittivity phase [325]. The introduction of a low permittivity pore in a high-permittivity ceramic matrix has been shown leading to a broadening of the electric field distribution in the ceramic component and a decrease in the electric field experienced by the ceramic due to a concentration of the electric field in the lower permittivity pore region [326].

To evaluate this concept, Roscow et al. fabricated a macro-porous BaTiO_3 via the sacrificial template process by using polyethylene glycol as a pore-forming agent, and obtained structures with 60 % porosity and pore diameter ranging between $100\text{--}400\ \mu\text{m}$ [324]. The piezoelectric energy harvesting FoM_{33} of the porous BaTiO_3 was remarkably improved to $2.85\ \text{pm}^2\text{N}^{-1}$, compared with $\sim 1.0\ \text{pm}^2\text{N}^{-1}$ for the dense BaTiO_3 . Due to the large reduction in permittivity, a three-fold increase in FoM_{33} was obtained. This research confirmed that the energy generated by porous ferroelectric ceramics under a certain applied stress could be considerably higher than their dense counterpart. The challenge is to design and manufacture appropriate pore configurations.

The microstructure of porous ferroelectrics is of great importance for

Table 19

Examples of porous ceramic catalyst supports with their fabrication strategies, pore features, loading materials, and potential applications.

Support Materials	Pore forming method	Pore features	Loading material	Remarks (Performance)	Refs
Al ₂ O ₃	Replica template (PU foam template)	Pore size: 10 ppi, 15 ppi Specific surface area: 0.35–0.45 m ² g ⁻¹	TiO ₂	Photocatalyst (phenol mineralisation)	[296]
Al ₂ O ₃	Sacrificial template (air drying ionotropic gelation)	Porosity: 60.4–79.5% Pore size: 180–315 μm	TiO ₂	Photocatalyst for water purification (photocatalytic activity up to 79.52 %)	[286]
Al ₂ O ₃	Replica template (PU foam template)	Porosity: 60.4–79.5% Pore size: 180–315 μm	TiO ₂	–	[293]
Cordierite	Sacrificial template (using starch as pore-forming agent)	Porosity: 24.63–38.12 Surface area: 0.36–7.70 m ² g ⁻¹ Pore size: 8.27–12.86 nm Pore volume: 0.0012–0.16 cm ³ g ⁻¹	MnOx/ TiO ₂	NO conversion (maximum 85.4 % at 200 °C)	[288]
Cordierite/ Kaolinite	Sacrificial template	open porosity: 25 %/ open porosity: 40 %	CuO- Co ₃ O ₄ - CeO ₂	carbon monoxide oxidation	[284]
Ceramic composite (40 % Al ₂ O ₃ , 55% SiO ₂)		Porosity: 71 % Pore size: 100–300 μm	Cu/ZnO; Pt	Methanol steam reforming (methanol conversion over 93 %), Combustion of Hydrogen (thermal efficiency 76.6 %)	[297]
SiC	Sacrificial template (by PS spheres)	Porosity: 74 % Pore size: 0.75/2.2/7.2 μm Surface area: 7.4 × 10 ⁷ /6.4 × 10 ⁶ /~10 ⁵ m ² g ⁻¹	Ru	Microreactor for H ₂ production (NH ₃ conversion >99.9% at temperatures above 700 °C)	[118]
SiC	Replica template (from fumed silica)	Pore size: 11–18 nm Specific surface area: 223–328 m ² g ⁻¹ Pore volume: 0.4–0.5 cm ³ g ⁻¹	Ni	Methane reforming rate up to 1.2 mmol g ⁻¹ s ⁻¹ (conversion of 22%)	[298]
SiC	Replica template	Porosity: 90 % Pore sizes: 40, 60, 80, 100 ppi	Pt	Hydrogen combustion for cooking stove (efficiencies up to 80 %)	[299]
SiO ₂	Sacrificial template (using egg white and glutinous rice flour as pore former)	Pore size: 200 μm/300 nm (Bimodal)	TiO ₂	Degradation of pollutants, environmental remediation (Degradation rate of MO under UV reached 92.07 %)	[285]
TiO ₂	Replica template	Pore size: 2 μm TiO ₂ nanorods (diameter 200–400 nm, length 10 μm)	Ti-Mn	Ozonation for water treatment	[300]
γ-Al ₂ O ₃	–	BET active surface area: 73 m ² g ⁻¹	Pd	Hydrogenation of nitrite (conversion rate up to 80 %)	[301]

maximising the electrical power generation. It is also believed that the connectivity of a porous ferroelectric ceramic determines its electrical, mechanical and thermal properties. To elucidate the principles of porous ferroelectric ceramics including electric field distribution [325,327], effect of pore structure on the poling behaviour and piezoelectric properties [326], experimental measurement was combined with finite element modelling approach. As shown in Fig. 71, the connectivity of a two-phase structure with respect to the dimensionality of the individual phases has been proposed and commonly used, where it is defined by two numbers, the first one refers to the connectivity of the piezo-active phase (strut) and the second one refers to the connectivity of the passive phase (pore) [323,324].

As illustrated in Fig. 72a, the longitudinal piezoelectric strain coefficient d_{33} of freeze-cast barium titanate (3–1 connectivity) is higher than that of uniform porous materials prepared by burning off polymer spheres (BURPS) (3–3 connectivity). Accordingly, the freeze-cast barium titanate demonstrates higher energy harvesting FoM, a

maximum of 3.79 pm²N⁻¹ being obtained for sample with 0.55 relative density (Fig. 72b,c), more than twice of its dense counterpart [328]. Additionally, the orientation of the pores has an impact, too. For freeze-cast 0.5Ba(Ca_{0.8}Zr_{0.2})O₃-0.5(Ba_{0.7}Ca_{0.3})TiO₃ (BCZT) and lead zirconate titanate (PZT), a depolarisation factor d_p of ~ 0.8 was obtained when pores were aligned in the electric field direction, whilst $d_p < 0.5$ when pores were aligned perpendicularly [326].

Porous PZT ceramics fabricated by freeze-casting achieved an improvement of compressive strength from 19 to 35 MPa, compared with other conventional manufacturing methods, in addition to the enhanced energy harvesting and sensing capability [150,323]. Freeze casting is therefore considered as one of the most promising techniques for manufacturing porous ferroceramics, since it not only creates a good alignment of porous phase which gives rise to an increased electromechanical coupling coefficient, but also could be tuned to achieve superb mechanical properties at the same time.

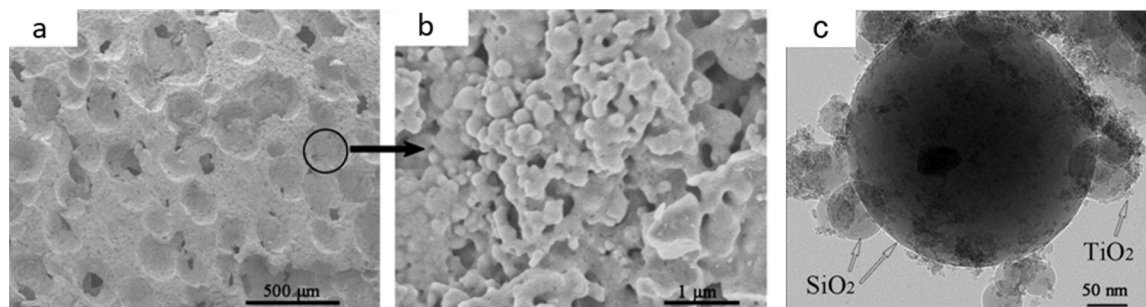


Fig. 60. SEM images (a, b) and TEM image (c) of the porous SiO₂-supported TiO₂ catalysts. Reproduced with permission [285]. Copyright 2015, Elsevier B.V.

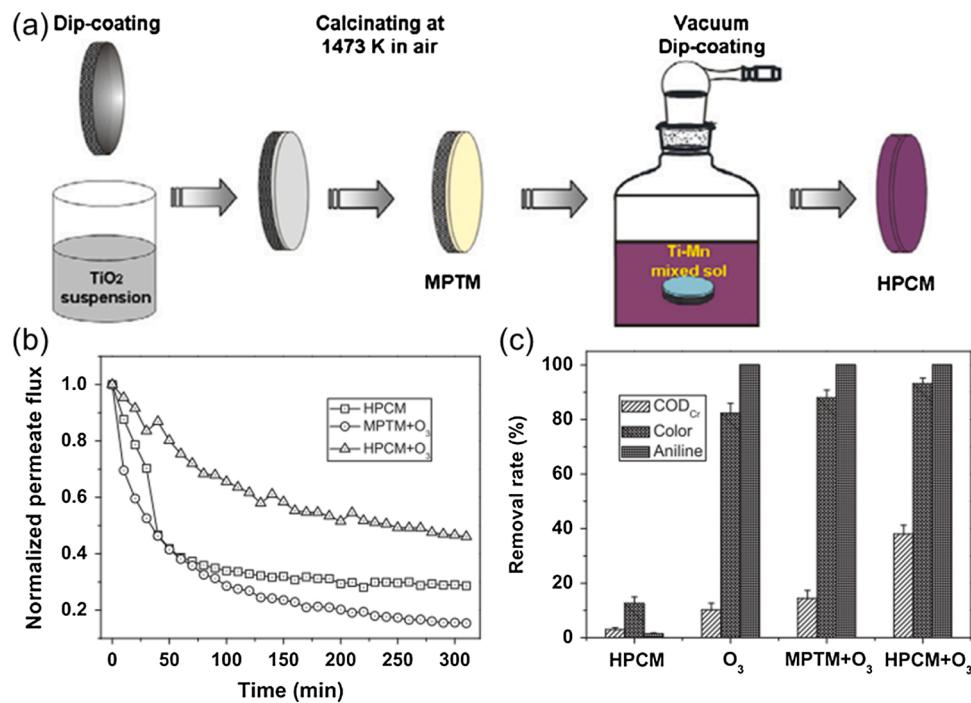


Fig. 61. (a) Fabrication process of MPTM and HPCM; A comparison of the MacroPorous TiO_2 -nanorods-assembled Membrane (MPTM) and Hierarchical Porous Catalytic Membrane (HPCM), (b) for the change of permeate flux, and (c) for contaminants removal rate. Reproduced with permission [300]. Copyright 2013, Elsevier B.V.

4.4.1. Piezoelectric energy harvesting

Piezoelectric materials that could generate an electrical field under an applied strain or vice versa are widely used in applications such as inkjet printers, sonars, heart monitors, actuators and sensors. Application as energy harvesters from vibration source which can be used to power small devices or recharge batteries has recently attracted immense research interests [329]. In this stress-driven system, selecting a low stiffness material, for example a porous piezoceramic, allows for more efficient transfer of mechanical energy into the material, which can outweigh the decrease in electromechanical coupling and transmission coefficients. The inclusion of porosity in dense piezoceramics is found to overcome impedance mismatching between them and the surrounding medium, since the reflected energy decreases with an increase of porosity [330,331]. Additionally, an increase in hydrostatic response, low dielectric loss $\tan \delta$, and low mechanical quality factors Q_m of porous piezoceramics made them promising candidates for piezoelectric-based devices with restricted force loadings such as

hydrophones, ultrasound scanners and transducers [323,332].

Roscow et al. reported the modelling, fabrication and characterisation of porous sandwich layered BaTiO_3 piezoelectric materials made of an inner porous layer and dense outer layers [325,333], as shown in Fig. 73a,b. An improved energy harvesting FoM of $3.74 \text{ pm}^2\text{N}^{-1}$ was obtained, which is larger than that of both the dense BaTiO_3 ($1.40 \text{ pm}^2\text{N}^{-1}$) and BaTiO_3 with 60 % volume fraction of randomly distributed porosity ($2.75 \text{ pm}^2\text{N}^{-1}$). Furthermore, Roscow et al. developed BaTiO_3 with 45 % porosity via freeze casting, and a maximum measured voltage of 234 mV was achieved, compared with 96 mV for the dense BaTiO_3 , representing a 2.4 fold improvement [328]. These significant improvements demonstrated the great potential of porous ferroelectric ceramics with optimised geography for high-performance energy harvesting and sensing applications.

4.4.2. Pyroelectric energy harvesting

Pyroelectric materials hold the potential to convert waste heat into

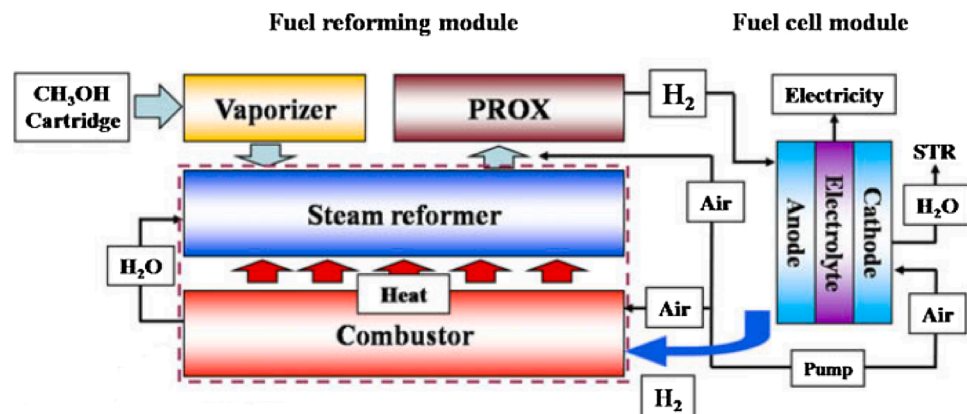


Fig. 62. Schematic of a fuel cell system integrated with a methanol reformer. The steam reformer is made of porous ceramics with Cu/ZnO loaded. Reproduced with permission [297]. Copyright 2009, Elsevier B.V.

electricity by alternatively heating and cooling a pyroelectric material. The capability for generating electric power from thermal fluctuations can be optimised by carefully engineering the morphology of porous ferroelectric materials, since the introduction of porosity reduces the volume specific heat capacity, which leads to increased pyroelectric FoMs [323].

Zhang et al. produced porous lead zirconate titanate (PZT) by freeze casting using water-based suspensions [150]. With the advance of porosity from 25 to 45 vol%, the lamellar oriented pore width decreased from 22–30 to 3–8 μm , while the lamellar thickness increased from 5–9 to 28–32 μm . For these porous ceramics, both types of pyroelectric harvesting FoM (F_E and F'_E) increased from 11.41 to 12.43 $\text{pJ m}^{-3}\text{k}^{-2}$ and 1.94 to 6.57 pm^3J^{-1} , respectively. They further investigated the orientation effect of PZT with aligned porosity fabricated through ice-templating and investigated the pyroelectric parameters parallel with and perpendicular to the freezing directions (Fig. 74a-c). They demonstrated these influence by charging a storage capacitor, and found that the fastest charging speed and maximum energy density were achieved by parallel-connected PZT with highest porosity of 60 vol% (Fig. 74d) [139], as a result, a pyroelectric energy density of 1653 $\mu\text{J cm}^{-3}$ was successfully obtained, which was 374 % higher than that of its dense counterpart (446 $\mu\text{J cm}^{-3}$). Srikanth et al. fabricated porous $\text{Ba}_{0.85}\text{Sr}_{0.15}\text{TiO}_3$ (BST) ceramics for pyroelectrics by using PMMA as the sacrificial template, and obtained porosities from 7.5 to 29.5% by varying the amounts of PMMA from 2 to 10 wt.% [334]. Compared with dense ceramics, the porosity in BST led to a reduction in the dielectric constant by up to over 78 % and a maximum improvement of FoM for energy harvesting F_e and F_e^* by 61 % and 98 %, respectively.

4.4.3. Electronic sensing applications

As well as the piezoelectric and pyroelectric energy harvesting devices, porous ferroelectrics have attracted attention in the field of electronic sensing applications. Ringgaard et al. developed porous piezoceramic transducer for acoustic pulse-echo measurements (Fig. 75a-c) [335]. Costa et al. built a self-powered and autonomous fringing field capacitive sensor to measure the soil water content [336], as shown in Fig. 75(d,e), by using an irrigation system based on a porous ceramic capacitive soil water sensor fabricated with printed circuit board (PCB) technology. The capacitance of the sensor increased up to 5% when the amount of water absorbed into the porous ceramic increased from 3% to 36 %. Blank et al. summarised the utilisation of

porous ceramics for micro-electromechanical resonant humidity sensor [337]. The working mechanism was based on the changes in their electro-mechanical behaviour due to water absorption on the ceramic surface. The performance of such humidity sensor was not only controlled by the surface reactivity with water, but also by microstructures of the porous ceramics. The sensitivity of porous ceramic sensor was superior to the non-porous ones, and the microstructural features were of great importance.

The use of porous piezoelectric ceramics with tuneable microstructural characteristics has shown great potential for mechanical and heat energy harvesting, compared with their dense counterparts. An insight into the possible effects of porosity, pore distribution and pore orientations on their performance has been provided by both experimental and modelling approaches. Sacrificial template method (which is commonly called BURPS) has been the major manufacturing approach, for its low cost, good control of the porosity, and scalability. However, higher piezoelectric and pyroelectric harvesting FoMs are achieved by porous freeze-cast ferroelectric ceramics with highly aligned porosity. Additionally, it has been acknowledged that a crack from the manufacturing stage could deter their performance considerably from proposed ones. Effort should be paid to the development of crack-free materials.

It is worth noting that intensive studies have been focusing on the design and selection of piezoelectric materials from the point of view of the materials engineer, incorporating of porous ferroelectrics into an energy harvesting system has yet to be discovered. The applications of porous ceramic-based energy harvesting system, including sensing and low-force actuators, deserve much focused studies, since ceramics provide the capability of surviving from the harsh operating conditions, which can be hardly obtained by metal or polymers. Meanwhile, the magnitude of power that generated by the energy harvesting equipment should be increased to pave the way for a wide range of applications [327].

4.5. Insulation applications

As discussed in Section 3.2 that porous ceramics possess excellent thermal insulation effect, simultaneously, superb Electromagnetic (EM) wave shielding performance and sound absorption capability are expected, due to their potential for achieving complex pore configurations.

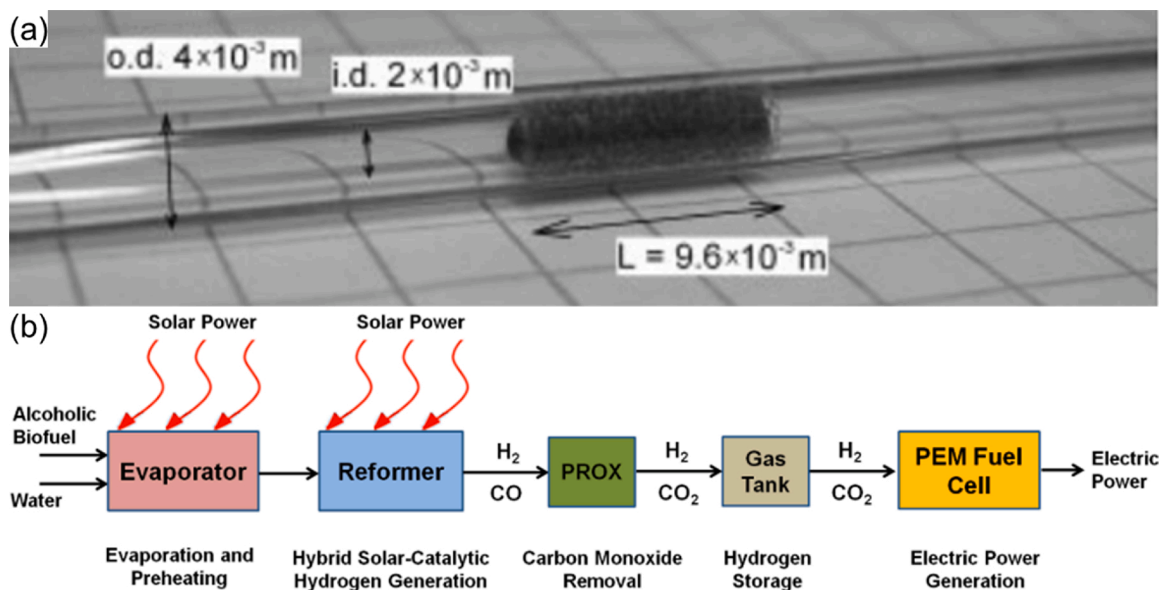


Fig. 63. (a) Digital photo of the foam-like $\text{ZrO}_2/\text{Ce}_{0.5}\text{Zr}_{0.5}\text{O}_2$ ceramic reactor in a quartz glass tube. (b) Schematic of a catalytic renewable energy conversion system. Reproduced with permission [306]. Copyright 2012, AIP Publishing LLC.

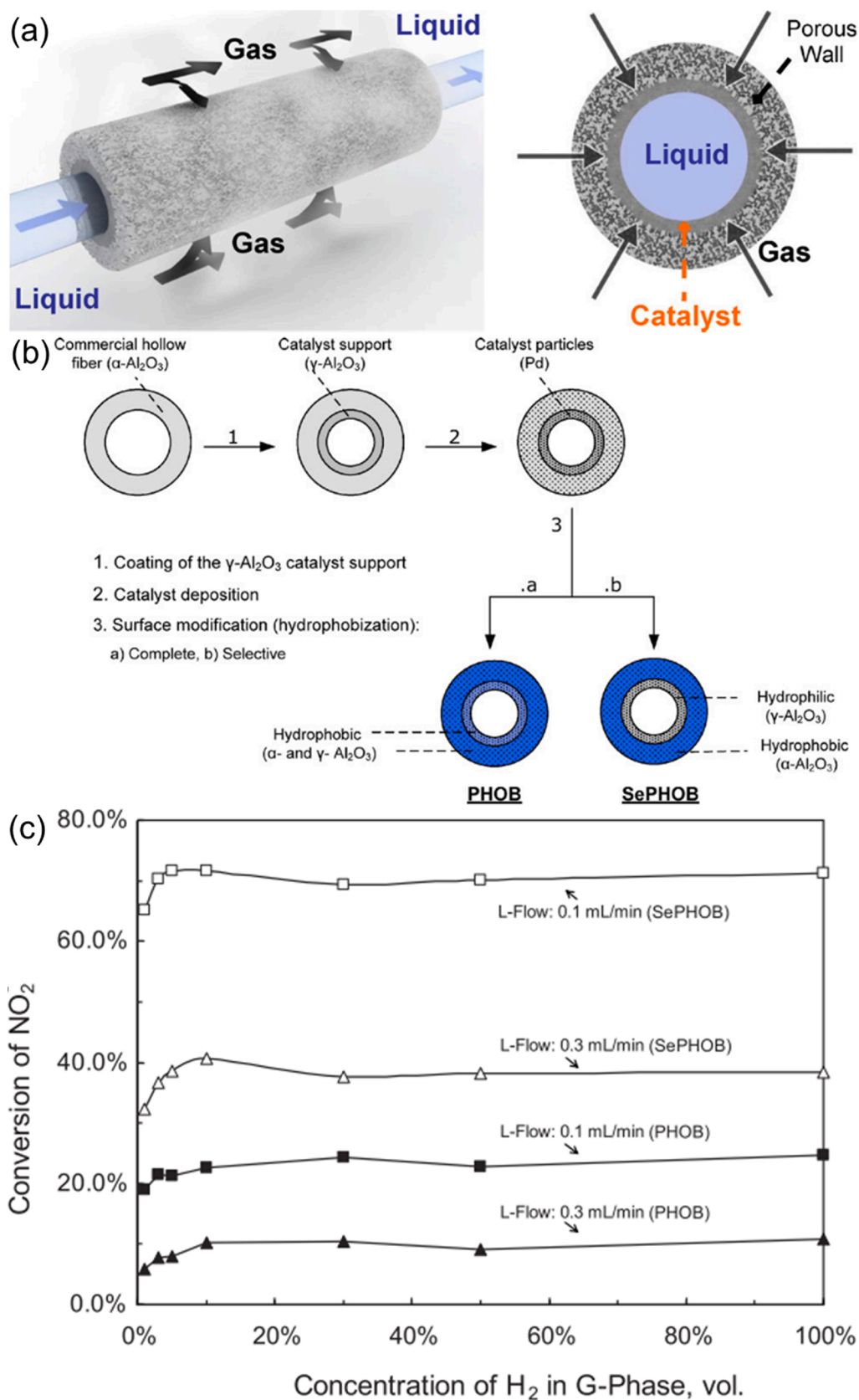


Fig. 64. (a) Schematic of a porous ceramic mesoreactor for the G-L-S reaction system. (b) Summary of the preparation steps of PHOB and SePHOB porous Al₂O₃ membranes. (c) The effect of H₂ concentration on the reactor performance. Reproduced with permission [301]. Copyright 2011, Elsevier B.V.

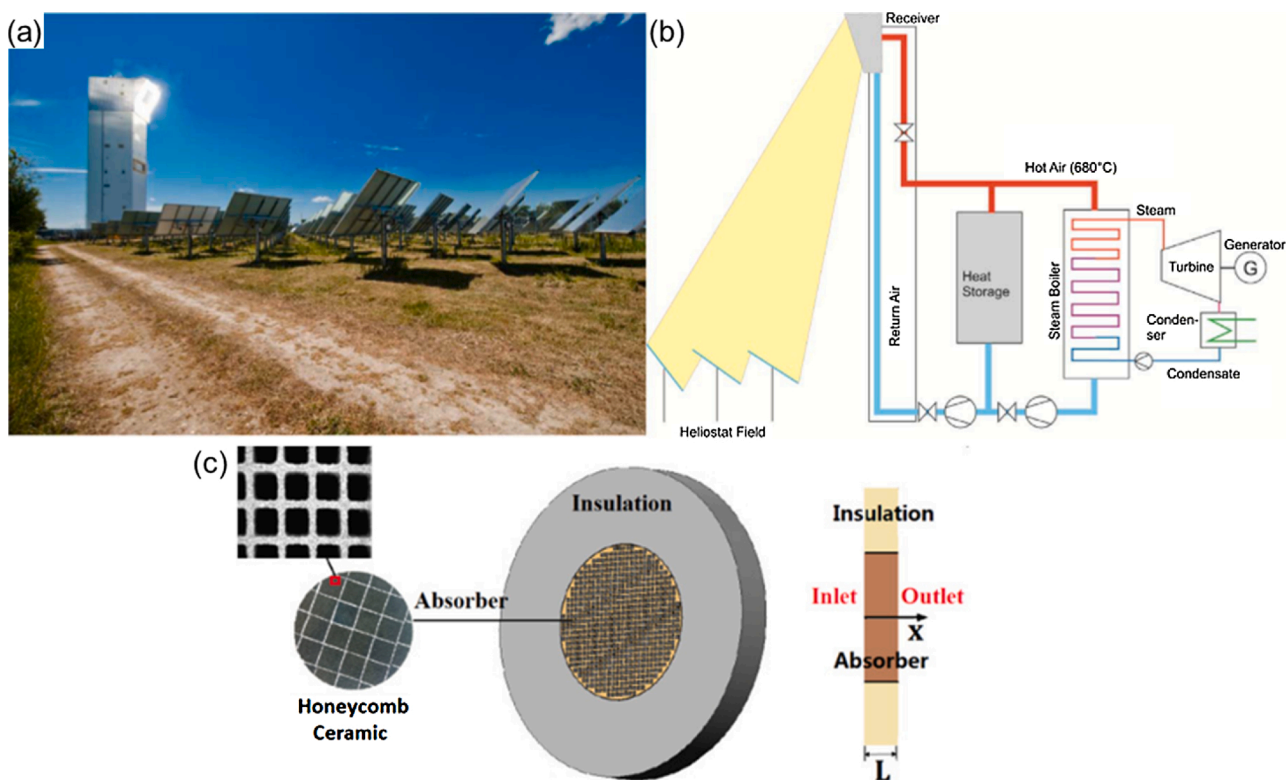


Fig. 65. The solar tower Julich (a) and its working principles (b). Reproduced with permission [309]. Copyright 2018, Elsevier B.V. (c) Schematic of a honeycomb ceramic air receiver model. Reproduced with permission [310]. Copyright 2017, AIP Publishing LLC.

4.5.1. Electromagnetic wave shielding

Electromagnetic (EM) wave with wavelength in the range of 2.4×10^{-2} to 3.7×10^{-2} m are widely used in electronic equipment, for uses in wireless communication, medical facilities, aerospace, and next-generation flexible electronic devices. Electromagnetic interference (EMI) shielding materials that can reflect and absorb EM waves (Fig. 76), with a target frequency range of 8.2–12.4 GHz, are required to protect both the instruments and human body [338]. Metal-based EMI shielding materials are limited by their high mass density and poor corrosion resistance. Lightweight materials with excellent EM reflection and absorption capabilities are therefore in high demand. However, polymer-based EMI shielding materials suffer from low strength and limited operation temperature, only stable up to 400 °C. In this regard, porous ceramics exhibits unique advantages [13].

The total EMI shielding effectiveness (SE_T), which can be expressed in decibels (dB) is a sum of reflection from the surface of shielding materials (SE_R), absorption energy of EM waves (SE_A), and multiple reflection (SE_M):

$$SE_T = SE_R + SE_A + SE_M \quad (19)$$

A SE of 20 dB indicates the block of 99 % of the incident signal, which is demanded for commercial applications [338].

Liang et al. investigated the EMI shielding performance by using porous SiC foams synthesised by a combination of direct foaming and freeze-drying techniques [13]. As shown in Fig. 77b, the sample with 72.8 % porosity exhibited an EMI shielding effectiveness higher than 20 dB. Surprisingly, the EMI shielding effectiveness increased with the rising of temperature, and a specific EMI shielding effectiveness over $24.8 \text{ dB cm}^{-3} \text{ g}^{-1}$ at a frequency of 11 GHz was obtained at 600 °C (Fig. 77c), which was 3 times higher than its dense counterpart (Fig. 77a). This excellent EMI shielding performance can be ascribed to the enhanced impedance match, the multiple internal reflection-absorption mechanisms generated from the porous structure, and the trapped incident waves interacting with ceramic grains, which would be reflected for numerous times on the cell walls before being

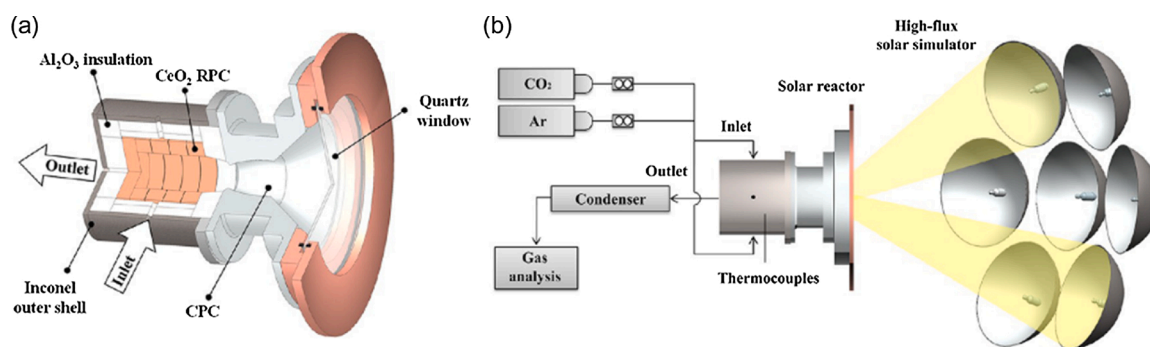


Fig. 66. (a) Schematic of the solar reactor configuration, and (b) experimental setup at RTH's High-Flux Solar Simulator. Reproduced with permission [313]. Copyright 2012, American Chemical Society.

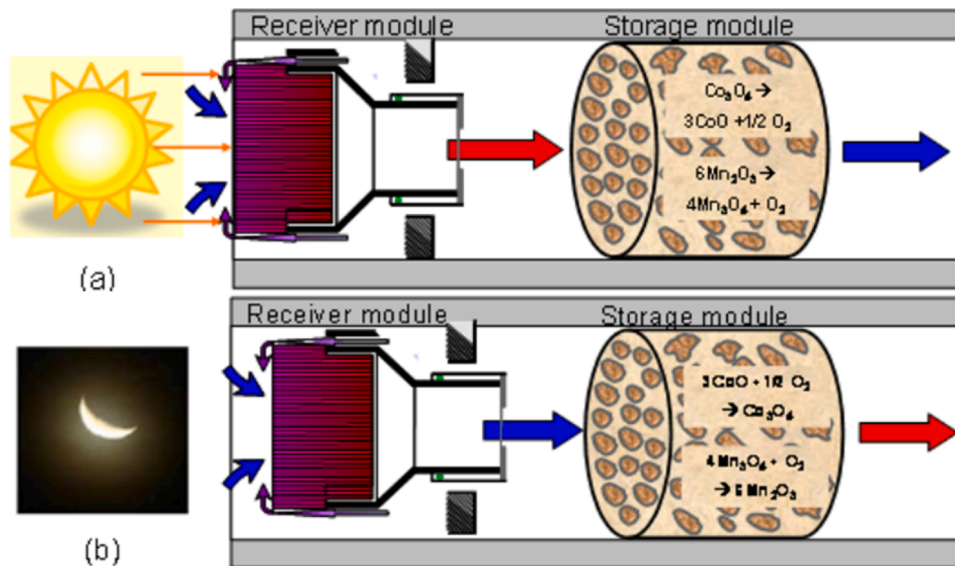


Fig. 67. Schematic of solar receiver storage during (a) on-sun, and (b) off-sun operation, respectively (add the reaction because cannot see clearly). Reproduced with permission [315]. Copyright 2016, AIP Publishing LLC.

absorbed or transferred to other energy completely (Fig. 77d) [13].

Ceramic composites containing conductive second phase are attractive for EMI shielding materials [338], multi-dielectric polarisation effects and tuneable EMI shielding performance can be obtained in the multi-components [339]. Zhou et al. used ordered mesoporous SiO₂ as the template, and filled it with carbon, followed by hot-pressing for densification of mesoporous C/SiO₂ composites [340]. Owing to the multi-reflection and scattering (Fig. 78a,b), the total EMI SE up to 35 dB was obtained by the composites with a thickness of 2.0 mm. Furthermore, graphene aerogel [341], and CNT [342], with higher permittivity

could form EMI shielding composites with very low volume fraction. Kuang et al. developed three-dimensional CNT/SiC nanowire (SiCnw) composite network for high-efficiency EM wave absorption. In their study, highly conductive CNT and semiconducting SiCnw were mixed with insulating paraffin wax at a weight ratio of 1:29:70 to form the EMI shielding material. The composites obtained a reflection loss over 10 dB in the frequency range of 8.5–11.9 GHz, with maximum reflection loss of 33.77 dB at 10.01 GHz. The high-performance EM wave absorbing effect can be accredited to two factors: firstly, CNT/SiCnw can construct a complex conduction network, enhancing the conduction loss; secondly,

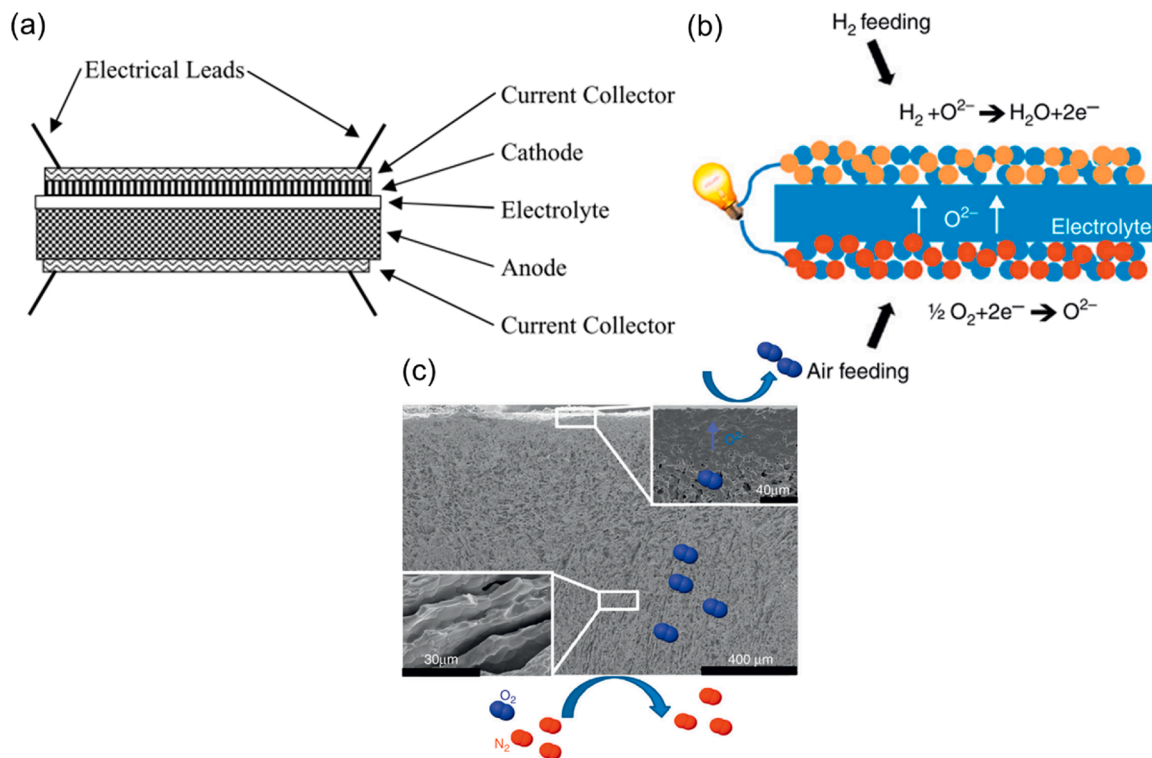


Fig. 68. (a) Schematic of a fuel cell configuration. Reproduced with permission [319]. Copyright 2003, Journal of the American Ceramic Society. (b) Schematic of a SOFC using porous ceramics as the electrode materials. (c) SEM image of a freeze-cast support for oxygen permeation. Reproduced with permission [166]. Copyright 2016, Elsevier B.V.

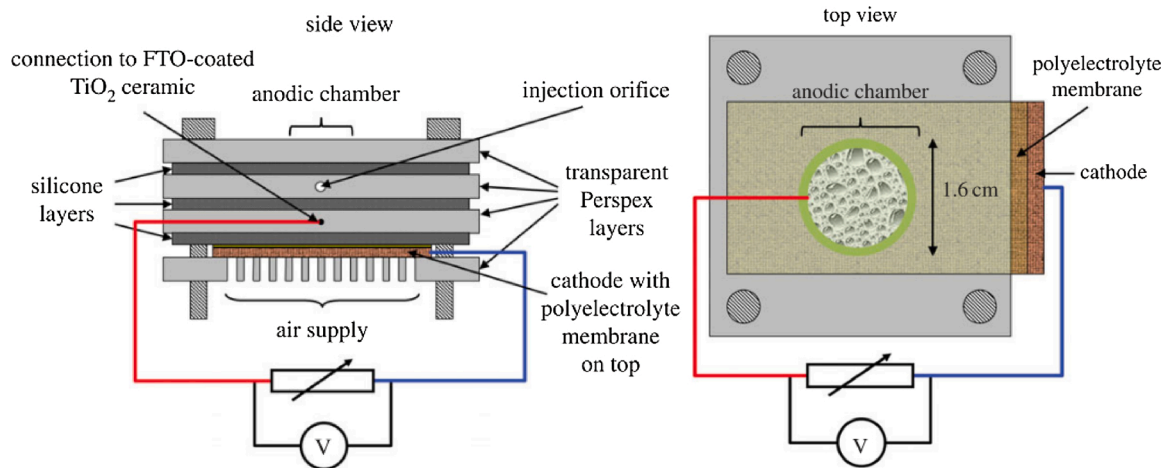


Fig. 69. Schematic of the p-MFC with fluorine-doped tin oxide (FTO)-coated TiO_2 ceramic as the anode coupled with a range of air cathodes. Reproduced with permission [321]. Copyright 2016, The Royal Society.

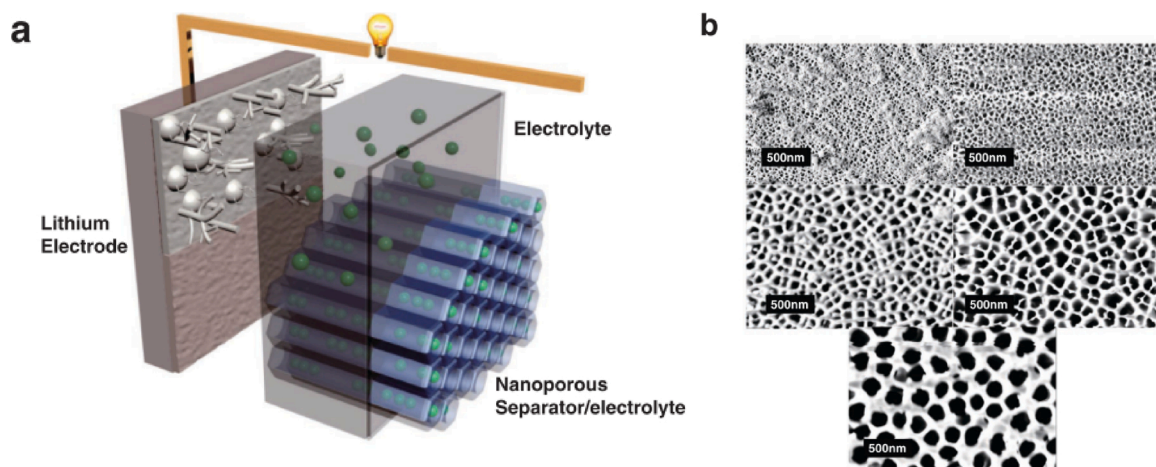


Fig. 70. (a) Illustration of an LMB made from nanoporous Al_2O_3 membranes containing the electrolyte. (b) FESEM images of Al_2O_3 membranes with different channel sizes in the range of 20–200 nm. Reproduced with permission [322]. Copyright 2017, Wiley-VCH Verlag GmbH & Co.

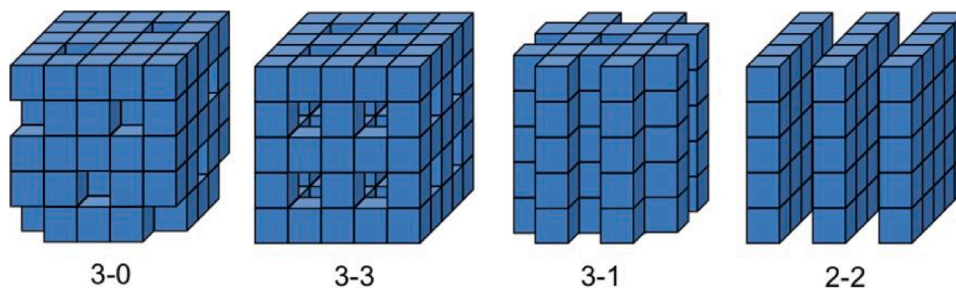


Fig. 71. Example of different model connectivity in biphasic composites. The two digits range from 0 (isolated particles) to 3 (full interconnection in all directions). The microstructure of porous BaTiO_3 was found to change from 3-0 configuration to 3-3 configuration when the level of porosity was increased. Reproduced with permission [323]. Copyright 2015, Springer Nature Switzerland AG.

by controlling the ratio of CNT and SiCnw, the electrical conductivity of the composites can be regulated to optimise the impedance matching [343].

4.5.2. Sound-proof applications

With the development of technological advances in many engineering areas, noise pollution that has harmful effects on human beings is now increasingly becoming a serious problem for the society. Sound absorption materials that are widely used for combustion chambers and

outside constructions are required to have the capacity of operating under harsh conditions, e. g. high temperatures and corrosive environments. Ceramic materials with specifically regulated porous microstructures are an excellent choice. The loss of sound has two mechanisms, the first is due to the flexural vibrations in the specimen, and the second is the porosity effect, where the acoustic energy is dissipated by multiple reflections of sound waves within the voids in the structure, which is the major sound absorption mechanism in porous ceramics. The sound absorption performance is defined by the sound

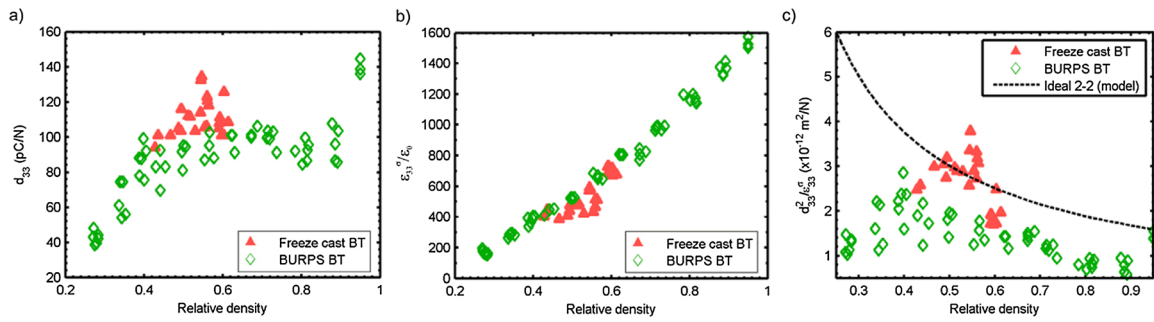


Fig. 72. Comparison of freeze-cast and uniform porous (by burning off polymer spheres) bariums titanate in terms of (a) longitudinal piezoelectric strain coefficient, d_{33} , (b) relative permittivity $\epsilon_{33}^{\sigma}/\epsilon_0$, and (c) energy harvesting FoM ($d_{33}^2/\epsilon_{33}^{\sigma}$) as a function of relative density. Reproduced with permission [328]. Copyright 2018, IOP Publishing Ltd.

absorption coefficient (α), which is the ratio of the unreflected sound intensity at the surface to the incident sound intensity, and the sound absorption coefficient (α) can be calculated using the following equation:

$$\alpha = 1 - \left(\frac{n-1}{n+1} \right)^2 \quad (20)$$

$$n = \frac{P_{MAX}}{P_{MIN}} \quad (21)$$

Where n represents the standing wave ratio, and P_{MAX} and P_{MIN} are the maximum and minimum sound pressures in the impedance tube [344, 345].

Airflow resistance is one of the most important parameters to evaluate the sound absorbing properties, high airflow resistance could increase the reflection of sound wave, whilst a low airflow resistance may lead to the transmission of the sound waves. To obtain promising sound absorbing performance, a controlled airflow resistance in the range of 1–200 kPa sm^{-2} and highly interconnected open porosity are necessary to maximise the friction and vibration between the sound waves and the pore walls, so that sound can thus be transformed to thermal energy [346]. Carlesso et al. investigated the sound absorbing performance of porous alumina/mullite-based porous ceramics fabricated via a combination of freeze casting with sacrificial polystyrene template [346]. As shown in Fig. 79 (a,b), an optimum airflow resistance was obtained simply by adjusting the porosity through changing the sacrificial polystyrene particle contents or slurry solid content. The samples with 13.50 and 13.75 g of polystyrene particles in the precursors presented extremely high sound absorption coefficients of 0.99 at 400 and 430 Hz, respectively. Meanwhile, samples produced from solid contents between 50 and 60 vol% exhibited sound absorption coefficient values in the range of 0.96 – 0.99, which agrees with their similar airflow resistance (Fig. 79c,d). It is noteworthy that by creating bimodal microstructure with connections between large and small pores, high sound absorption

coefficient values at different frequencies were obtained. This result shows that ceramics are very promising for sound absorbing applications, which is an area of understudied.

5. Concluding remarks

In this article, a comprehensive review of porous ceramics with their updated fabrication method, properties, and energy- and environmental-related applications has been presented: (1) Partial sintering as a simple and cost-effective method has gained better control of microstructure and enhanced mechanical strength via hot press and SPS technique. The inherent limitation of low porosity (< 50 %) can be overcome through the combination of in-situ chemical reaction; (2) Replica template as an effective way of creating reticulated open cell porous ceramics, provides an easy control of the pore geometries and pore size by selecting a suitable original template. Synthetic polymeric templates (e.g. PU foam) better off natural resources in terms of the reliability and structural integrity. However, new techniques based on sustainable templates for specific applications is still of interests for future research. On the other hand, an optimum rheological behavior of the coating slurries that dictated by the solid content and additives is the key to minimise the defects and cracking of porous bodies created during thermal decomposition of the polymeric sponge. Furthermore, additional infiltration process could give rise to enhanced mechanical strength; (3) Sacrificial template is a method that can create a negative replica of original pore features, by controlling the type, content, and dimension of the incorporated pore formers, a high degree of flexibility for controlling both the porosity and the pore size, shape, and morphologies can be obtained. Freeze-casting technique, which is categorised as liquid based-sacrificial template generates a unique vertically aligned hierarchical porous structure, a precision control over the ordered anisotropic microstructure can be achieved through the manipulation of the solvent type, solid loading of pre-ceramic slurries, freezing conditions, and additives. The freeze-cast porous ceramics with

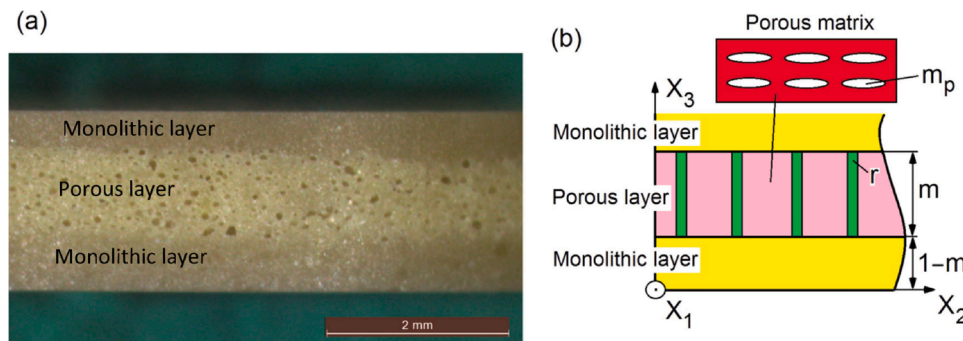


Fig. 73. Image (a) and schematic (b) of the sandwich layered BaTiO₃ structures. Reproduced with permission [333]. Copyright 2017, IOP Publishing Ltd.

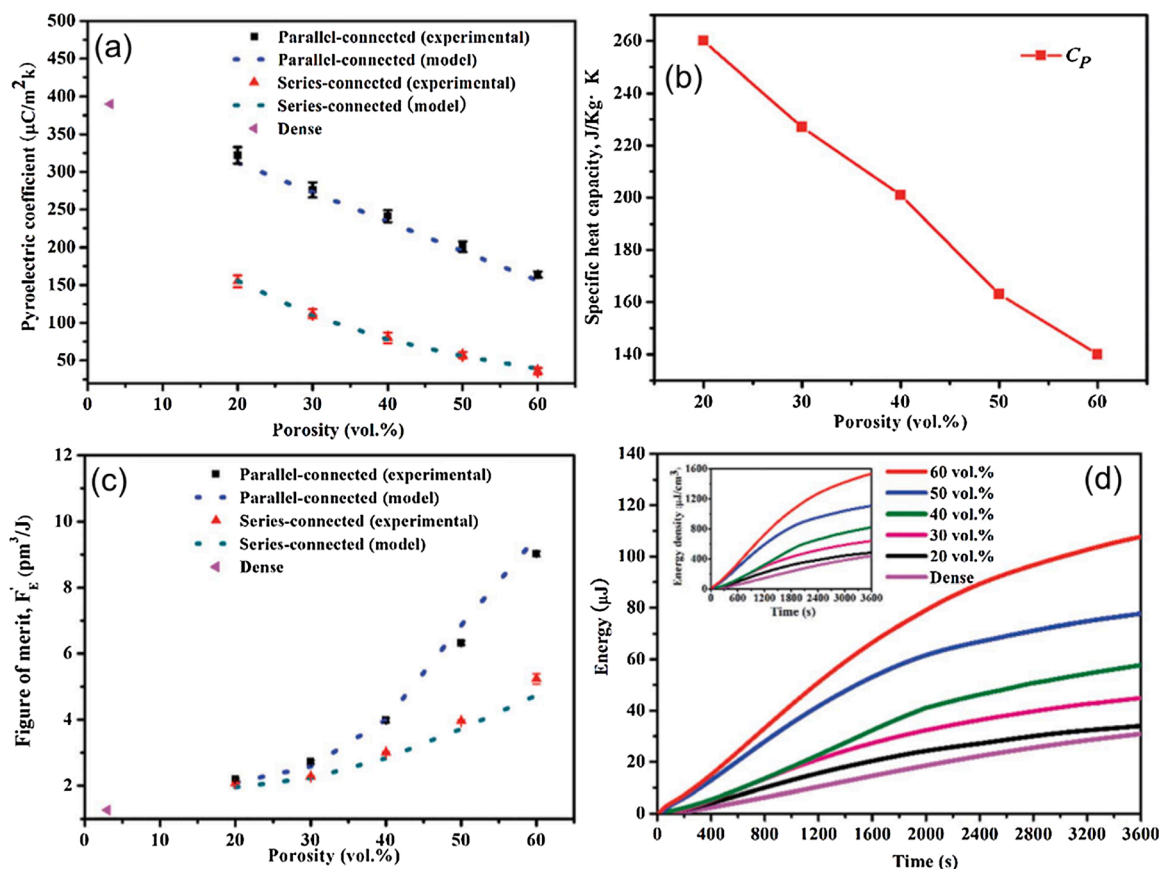


Fig. 74. (a) Pyroelectric coefficients, (b) specific heat capacity, and (c) pyroelectric FoM, of freeze-cast porous PZT with both modelling and experimental results. (d) Charging energy of the capacitor, the inset showing the charging energy density. Reproduced with permission [139]. Copyright 2017, The Royal Society of Chemistry.

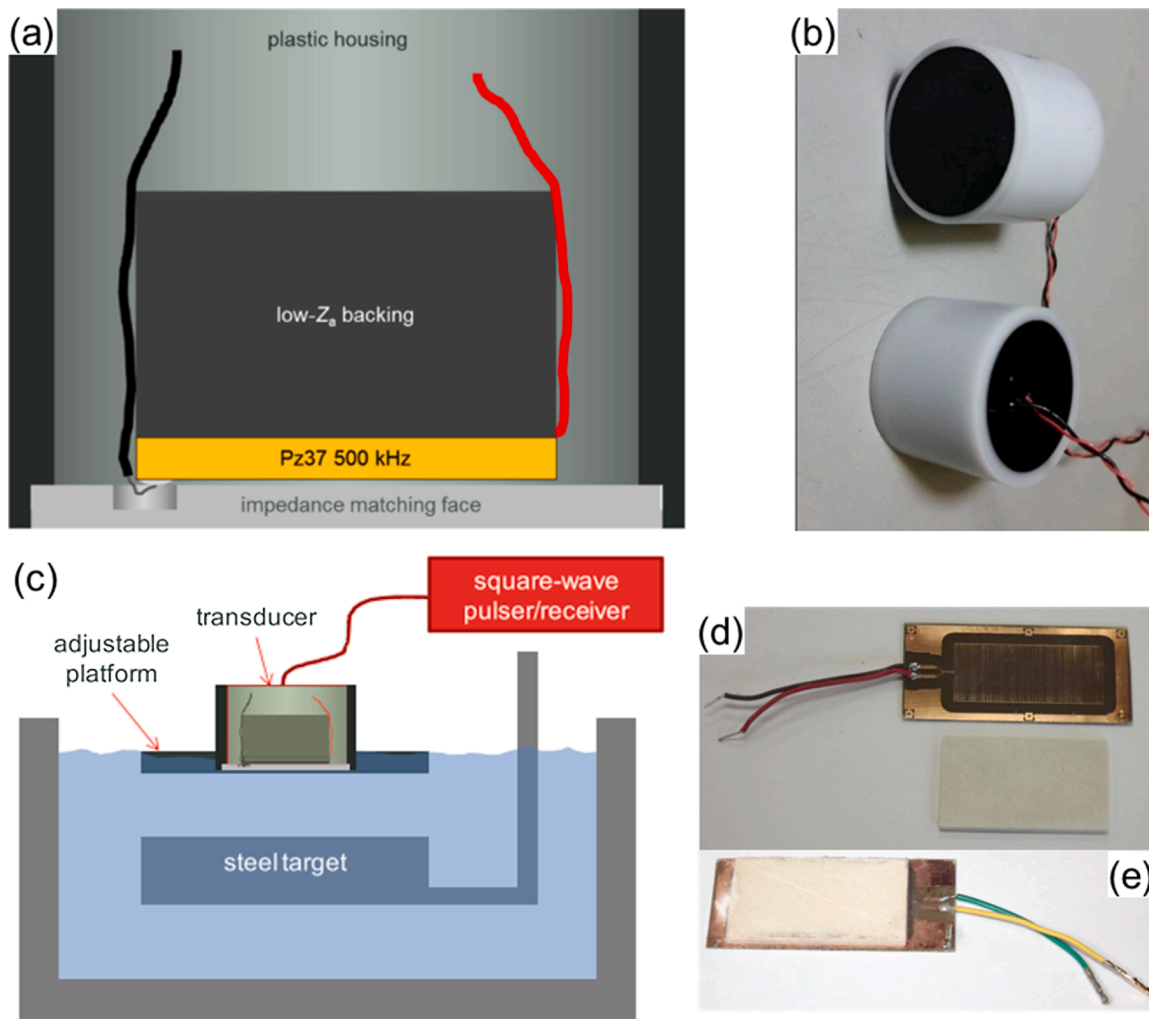


Fig. 75. (a) Schematic of a transducer design; (b) Assembled transducers made from PZT with porosity of $\sim 25\%$; and (c) Measurement set-up for pulse-echo measurement. Reproduced with permission [335]. Copyright 2015, MDPI. (d) Photograph of a PCB with interdigitated electrodes (top) and a porous ceramic plate (bottom). (e) Photograph of the fabricated sensor. Reproduced with permission [336]. Copyright 2017, MDPI.

closed pores are widely used as energy harvesting and insulation applications; (4) Direct foaming is a template-free approach for fabrication of macroporous ceramics, in which the pores are generated via mechanical frothing or chemical blowing the surfactant containing pre-ceramic suspension. This easy, cheap, and fast processing method holds the possibility of mass production at industrial level. With the progress made on the fabrication of porous ceramics, the porosity and pore size distribution of each traditional approach have been expanded; (5) Attention has also been paid to the additive manufacturing as the emerging technology, which shows strong feasibility and unique

advantages for producing porous ceramics. Owing to the rapid layer-by-layer process according to a computer aided design, precisely customised architectures with full control of the geometrical parameters, such as porosity, pore size, and pore interconnectivity can be obtained by additive manufactured porous ceramics. However, the limited material selection and high cost should be addressed in future. This review aims to provide a guidance for manufacturing of porous ceramics, the details of fabrication processes are therefore collectively summarised, the advantages and shortcomings, together with the innovations and potentials of these fabrication strategies are critically discussed.

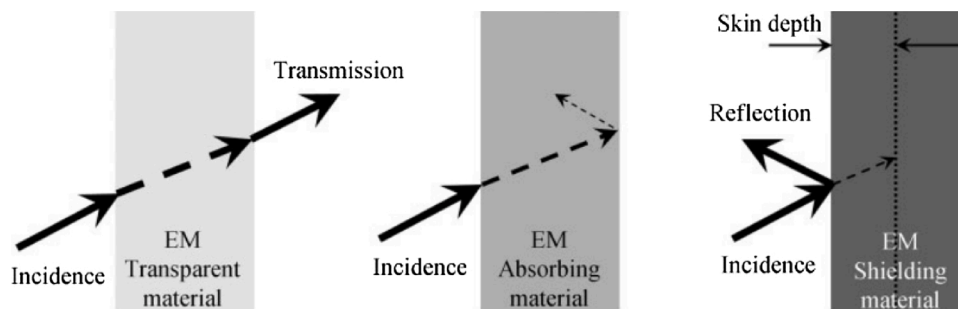


Fig. 76. Schematic of three processes the incident electronic EM wave interacting with materials. Reproduced with permission [338]. Copyright 2014, Informa UK Limited.

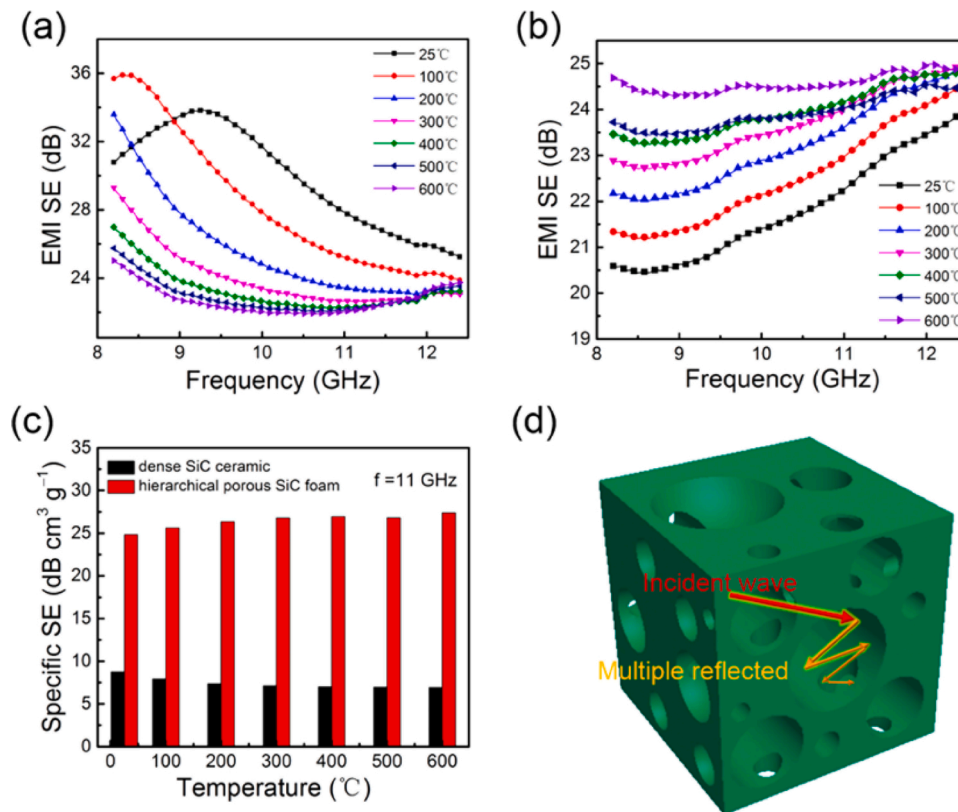


Fig. 77. EMI shielding efficiencies of (a) dense SiC ceramic, and (b) hierarchical porous SiC foam; (c) The specific EMI SE of both dense SiC and porous SiC foam at 11 GHz. (d) Schematic of the EMI shielding mechanism in the porous SiC foam. Reproduced with permission [13]. Copyright 2017, American Chemical Society.

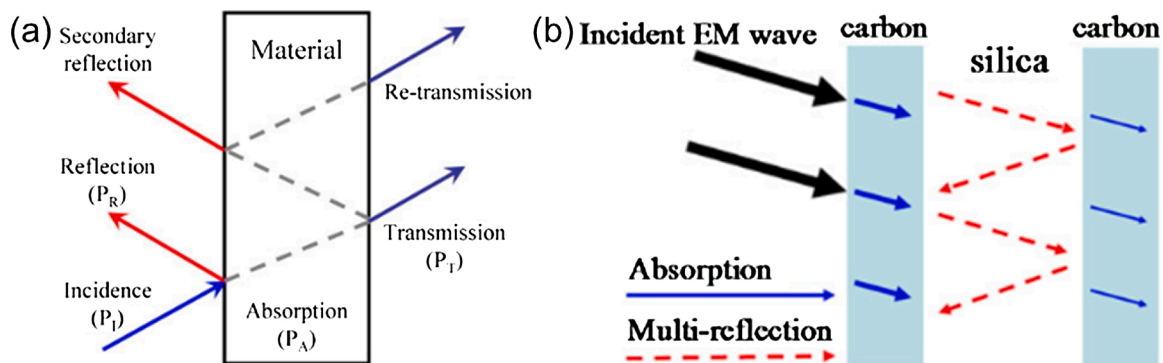


Fig. 78. (a) Schematic of incident electromagnetic wave traveling through a solid material. The incident EM wave experiencing three processes: reflection, absorption, and transmission. Reproduced with permission [338]. Copyright 2014, Informa UK Limited. (b) Schematic of a multi-reflection pathway of the incident EM wave in ordered C/SiO₂ composites. Reproduced with Permission [340]. Copyright 2012, Elsevier B.V.

Introducing pores into ceramics is believed to be detrimental to the mechanical strength of structural materials, as a result, the improvement of desired specific performance always comes at an expense of their mechanical properties. However, a good offset the loss of mechanical strength can be provided by a well-controlled size, shape, and orientation of pores and grains. Meanwhile, enhanced damage tolerance, thermal shock resistance as a result of crack-pore interactions, as well as the thermal insulation capability are exceptional merits of porous ceramics, as compared with their dense counterparts, making them ideal materials for service under harsh conditions. By selecting the appropriate materials and processing approach, the conflicting demands of low thermal conductivity and high mechanical strength can be met. Additionally, a second phase can always be incorporated into the porous structures to form a composite so that to modify these properties.

Benefiting from chemical inertness, high temperature stability, low

thermal conductivity, thermal shock resistance, and good durability, porous ceramics has created a variety of applications. In this review, special emphasis has been placed on energy- and environment-related typical examples, which is believed the driving force for future research of porous ceramics. The material selection, processing approaches, and microstructural features are taken into consideration. (1) Porous ceramics with uniform porosity, pore sizes, adequate permeability, and competent structural strength can be utilised in filtration applications including hot-gas filters, diesel particulate filters, and water filtration system. The microstructural features of filters should be optimised for a trade-off between ideal filtration performance and mechanical robustness; (2) Porous ceramics with high permeability have been most frequently used as support to immobilise catalyst for environmental remediation and hydrogenation process. Efforts have been made to optimise the structure of the catalyst support, which is

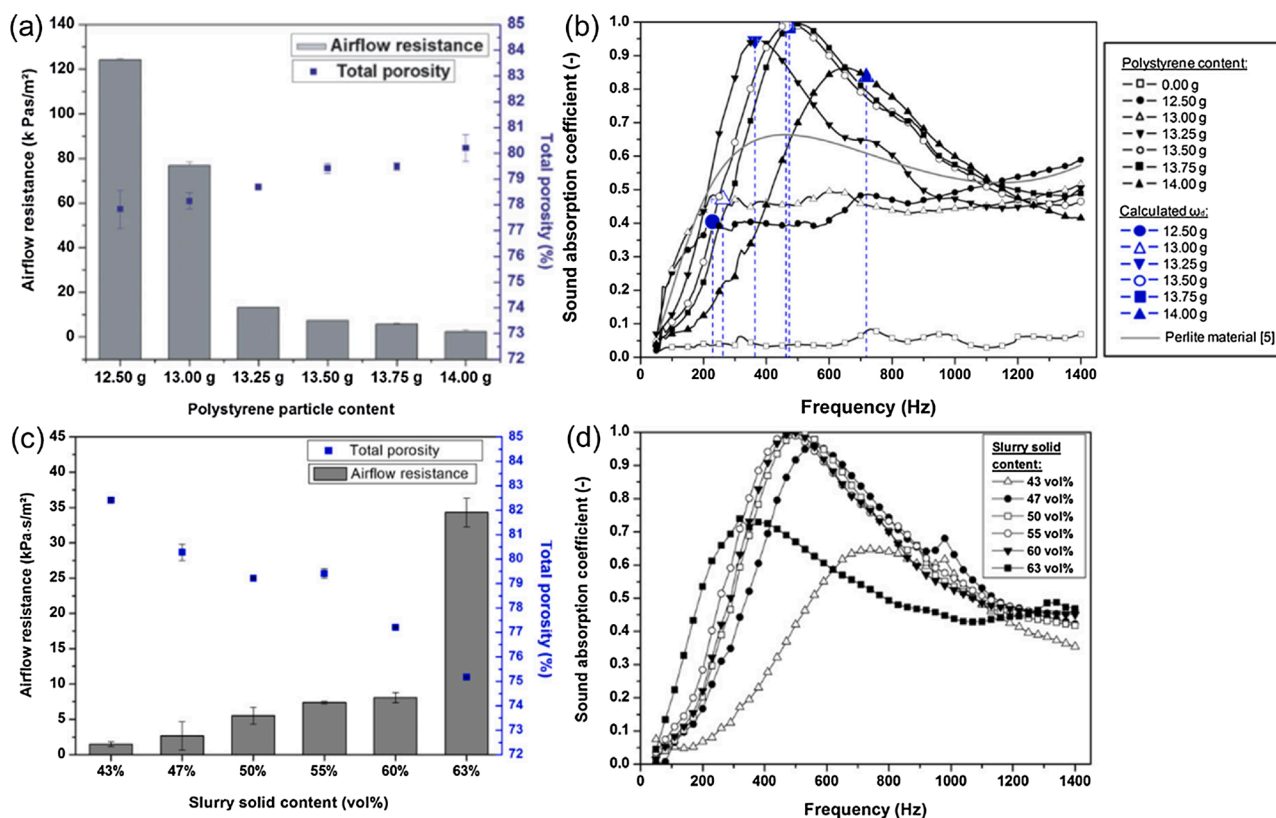


Fig. 79. (a) The airflow resistance and total porosity as a function of the sacrificial template - polystyrene particle contents, (b) Sound absorption coefficient as a function of frequency for samples prepared using different sacrificial template - polystyrene particle contents, (c) The airflow resistance and total porosity as a function of the slurry solid contents, (d) Sound absorption coefficient as a function of frequency for samples prepared using different slurry solid contents. Reproduced with permission [346]. Copyright 2013, The American Ceramic Society.

considered as more important factors than purely increase the intrinsic activity of catalysts; (3) Porous ceramics has been adopted as essential components in energy storage and conversion applications such as concentrated solar power, fuel cell, and batteries. However, very limited literatures have reported the porous ceramics as components for these applications, much effort is required to fully understand the value of porous ceramics; (4) Porous lead PZT and BaTiO₃ ferroelectric ceramics have been well-established as microelectromechanical systems (MEMS) to harvest energy from surrounding environment for powering small-scale electronic devices. Based on both the experimental and modelling study of porous ceramic-based MEMS, advanced sensor and low-force actuator with high sensitivity deserve much forced studies; (5) Owing to the complex pore configurations, porous ceramics are natural insulators. Superb electromagnetic wave shielding and soundproof capabilities are exploited as well.

We have tried to outline the basic selection criteria for choosing the right process and materials for specific applications. In each application, advantages of porous ceramics over metals and polymers are highlighted. In future, efforts are envisaged to be made for engineering affordable, efficient, and long-term reliable porous ceramics with optimised pore characteristics are of great interests. Particularly, we are bold to foresee that two objectives in the future research will be prioritised. One is related to the sustainability. Natural resources such as wood, bamboo, cellulose will be the new inspiration for material selection, because they can be utilised as both the starting materials and templates. Adequate pre-treatments, such as carbonisation and freeze-drying, will allow for their further exploration. The other is about the precise control of the microstructure and pore configuration. Utilising commercially and naturally available porous structures (e.g. PU foam, melamine foam, even MOF) with complex pore structures as the template will pave the way for engineering porous ceramics with desired

and ultrafine porosity.

CRediT authorship contribution statement

Yu Chen: Data curation, Writing - original draft. **Nannan Wang:** Data curation, Validation, Writing - review & editing. **Oluwafunmilola Ola:** Writing - review & editing, Visualization, Investigation. **Yongde Xia:** Writing - review & editing, Supervision. **Yanqiu Zhu:** Supervision, Writing - review & editing.

Declaration of Competing Interest

The authors report no declarations of interest.

Acknowledgements

The present work was supported by the National Natural Science Foundation of China (Grant No 51972068) and Key Laboratory of New Processing Technology for Nonferrous Metals and Materials (Guangxi University).

References

- [1] T. Ohji, M. Fukushima, *Int. Mater. Rev.* 57 (2012) 115–131.
- [2] A.R. Studart, U.T. Gonzenbach, E. Tervoort, L.J. Gauckler, *J. Am. Ceram. Soc.* 89 (2006) 1771–1789.
- [3] P. Colombo, C. Vakifahmetoglu, S. Costacurta, *J. Mater. Sci.* 45 (2010) 5425–5455.
- [4] C. Galassi, *J. Eur. Ceram. Soc.* 26 (2006) 2951–2958.
- [5] E.C. Hammel, O.L.R. Ighodaro, O.I. Okoli, *Ceram. Int.* 40 (2014) 15351–15370.
- [6] M.V. Twigg, J.T. Richardson, *Ind. Eng. Chem. Res.* 46 (2007) 4166–4177.
- [7] J.-H. Eom, Y.-W. Kim, S. Raju, *Integr. Med. Res.* 1 (2013) 220–242.
- [8] A.M.Z. Zimar, M.H. Nowsath, M.N. Muhammad, S.R. Herath, in: 2nd Int. Moratuwa Eng. Res. Conf. (MERCon), IEEE 2016, 2016, pp. 349–354.

- [9] X. He, B. Su, Z. Tang, B. Zhao, X. Wang, G. Yang, H. Qiu, H. Zhang, J. Yang, *J. Porous Mater.* 19 (2012) 761–766.
- [10] L. Dou, X. Zhang, X. Cheng, Z. Ma, X. Wang, Y. Si, J. Yu, B. Ding, *ACS Appl. Mater. Interfaces* 11 (2019) 29056–29064.
- [11] Z. Zakaria, Z. Awang Mat, S.H. Abu Hassan, Y. Boon Kar, *Int. J. Energy Res.* 44 (2020) 594–611.
- [12] I. Patel, *InTech China* (2011) 133–150.
- [13] C. Liang, Z. Wang, L. Wu, X. Zhang, H. Wang, Z. Wang, *ACS Appl. Mater. Interfaces* 9 (2017) 29950–29957.
- [14] E. Gregorová, W. Pabst, Z. Sofer, O. Jankovský, J. Matějček, *J. Phys. Conf. Ser.* 395 (2012), 012022.
- [15] D. Hardy, D.J. Green, *J. Eur. Ceram. Soc.* 15 (1995) 769–775.
- [16] A. Diaz, S. Hampshire, J.F. Yang, T. Ohji, S. Kanzaki, *J. Am. Ceram. Soc.* 88 (2005) 698–706.
- [17] L. Fan, M. Zhou, H. Wang, Z. Shi, X. Lu, C. Wang, *J. Am. Ceram. Soc.* 97 (2014) 1371–1374.
- [18] M. Fukushima, *J. Ceram. Soc. Japan* 121 (2013) 162–168.
- [19] M. Ghoranneviss, A.S. Elahi, *Mater. Manuf. Process.* 30 (2015) 1348–1353.
- [20] Q. Guo, H. Xiang, X. Sun, X. Wang, Y. Zhou, *J. Eur. Ceram. Soc.* 35 (2015) 3411–3418.
- [21] X.-F. Wang, H.-M. Xiang, X. Sun, J.-C. Liu, F. Hou, Y.-C. Zhou, *J. Am. Ceram. Soc.* 98 (2015) 2234–2239.
- [22] A. Kocjan, Z. Shen, *J. Eur. Ceram. Soc.* 33 (2013) 3165–3176.
- [23] Z.-Y. Deng, J.-F. Yang, Y. Beppu, M. Ando, T. Ohji, *J. Am. Ceram. Soc.* 85 (2002) 1961–1965.
- [24] T. Ohji, *Mater. Sci. Eng. A* 498 (2008) 5–11.
- [25] X. Jin, X. Zhang, J. Han, P. Hu, R. He, *Mater. Sci. Eng. A* 588 (2013) 175–180.
- [26] X. Jin, L. Dong, H. Xu, L. Liu, N. Li, X. Zhang, J. Han, *Ceram. Int.* 42 (2016) 9051–9057.
- [27] F. Akhtar, P.O. Vasiliu, L. Bergström, *J. Am. Ceram. Soc.* 92 (2009) 338–343.
- [28] Y. Yang, Y. Wang, W. Tian, Z. Wang, C.-G. Li, Y. Zhao, H.-M. Bian, *Scr. Mater.* 60 (2009) 578–581.
- [29] G. Jean, V. Sciamanna, M. Demuyneck, F. Cambier, M. Gonon, *Ceram. Int.* 40 (2014) 10197–10203.
- [30] D. Chakravarty, H. Ramesh, T.N. Rao, *J. Eur. Ceram. Soc.* 29 (2009) 1361–1369.
- [31] H. Ning, G.D. Mastroiello, S. Grasso, B. Du, T. Mori, C. Hu, Y. Xu, K. Simpson, G. Maizza, M. Reece, *J. Mater. Chem. A* (2015) 17426–17432.
- [32] M. Hotta, H. Kita, H. Matsuura, N. Enomoto, J. Hojo, *J. Ceram. Soc. Japan* 120 (2012) 243–247.
- [33] H. Yuan, J. Li, Q. Shen, L. Zhang, *Int. J. Refract. Met. Hard Mater.* 36 (2013) 225–231.
- [34] G. Xu, T. Olorunoyemi, Y. Carmel, I. Lloy, O. Wilson, *J. Am. Ceram. Soc.* 86 (2003) 2082–2086.
- [35] X. Yao, S. Tan, X. Zhang, Z. Huang, D. Jiang, *J. Mater. Sci.* 42 (2007) 4960–4966.
- [36] Y.W. Kim, Y.J. Jin, J.H. Eom, I.H. Song, H.D. Kim, *J. Mater. Sci.* 45 (2010) 2808–2815.
- [37] A. Kalemtas, G. Topates, H. Özcohan, H. Mandal, F. Kara, R. Janssen, *J. Eur. Ceram. Soc.* 33 (2013) 1507–1515.
- [38] A. Kishimoto, *J. Ceram. Soc. Japan* 121 (2013) 527–533.
- [39] M. Wang, D. Zhang, S. Wang, Z. Zhao, *J. Inorg. Organomet. Polym. Mater.* 22 (2011) 17–20.
- [40] C. Balázi, Z. Shen, Z. Kónya, Z. Kasztovszky, F. Wéber, Z. Vértesy, L.P. Biró, I. Kiricsi, P. Arató, *Compos. Sci. Technol.* 65 (2005) 727–733.
- [41] S.T. Oh, K.I. Tajima, M. Ando, T. Ohji, *J. Am. Ceram. Soc.* 83 (2000) 1314–1316.
- [42] S. Honda, S. Hashimoto, S. Iwata, Y. Iwamoto, *Ceram. Int.* 42 (2016) 1453–1458.
- [43] C. Ferraro, E. Garcia-Tunon, S. Barg, M. Miranda, N. Ni, R. Bell, E. Saiz, *J. Eur. Ceram. Soc.* 38 (2017) 823–835.
- [44] W. Pabst, E. Gregorová, I. Sedlářová, M. Černý, *J. Eur. Ceram. Soc.* 31 (2011) 2721–2731.
- [45] C. Yuan, L.J. Vandeperre, R.J. Stearn, W.J. Clegg, *J. Mater. Sci.* 43 (2008) 4099–4106.
- [46] R. Ahmad, M.S. Anwar, J. Kim, I.H. Song, S.Z. Abbas, S.A. Ali, F. Ali, J. Ahmad, H. Bin Awais, M. Mehmood, *Ceram. Int.* 42 (2016) 18711–18717.
- [47] M. Kim, R.A. Franco, B.T. Lee, *J. Eur. Ceram. Soc.* 31 (2011) 1541–1548.
- [48] I. Himoto, S. Yamashita, H. Kita, *Adv. Powder Technol.* 27 (2015) 948–958.
- [49] S.Y. Gómez, O.A. Alvarez, J.A. Escobar, J.B. Rodrigues Neto, C.R. Rambo, D. Hotza, *Adv. Mater. Sci. Eng.* 2012 (2012) 1–9.
- [50] E.C. Bucharsky, K.G. Schell, R. Oberacker, M.J. Hoffmann, *J. Am. Ceram. Soc.* 93 (2010) 111–114.
- [51] F. Baido, S. Caddeo, G. Novajra, C. Vitale-Brovarone, *J. Eur. Ceram. Soc.* 36 (2015) 2175–2182.
- [52] V. Medri, M. Mazzocchi, A. Bellosi, *Int. J. Appl. Ceram. Technol.* 8 (2011) 815–823.
- [53] F. Sarhadi, M. Shafiee Afarani, D. Mohebbi-Kalhari, M. Shayesteh, *Appl. Phys. A* 122 (2016) 390.
- [54] Z. Sun, Y. Liang, M. Li, Y. Zhou, *J. Am. Ceram. Soc.* 93 (2010) 2591–2597.
- [55] S.C. Santos, C. Yamagata, L.L. Campos, S.R.H. Mello-Castanho, *Mater. Chem. Phys.* 177 (2016) 505–511.
- [56] D. Desimone, W. Li, J.A. Roether, D.W. Schubert, M.C. Crovace, A.C. M. Rodrigues, E.D. Zanotto, A.R. Boccaccini, *Sci. Technol. Adv. Mater.* 14 (2013), 045008.
- [57] K. Bodišová, M. Kašiarová, M. Domanická, M. Hnatko, Z. Lenčák, Z.V. Nováková, J. Vojtašák, S. Gromošová, P. Šajgalík, *Ceram. Int.* 39 (2013) 8355–8362.
- [58] J.H. Sung, K.H. Shin, Y.W. Moon, Y.H. Koh, W.Y. Choi, H.E. Kim, *Int. Ceram. Soc.* 35 (2012) 93–97.
- [59] S.K. Swain, S. Bhattacharyya, D. Sarkar, *Mater. Sci. Eng. C* 31 (2011) 1240–1244.
- [60] C. Duong-viet, H. Ba, Z. El-berrichi, J. Nhut, *New J. Chem.* 40 (2016) 4285–4299.
- [61] S.A. Alekseev, D.M. Korytko, S.V. Gryn, V. Iablokov, O.A. Khainakova, S. Garcia-Granda, N. Kruse, *J. Phys. Chem. C* 118 (2014) 23745–23750.
- [62] S. Akpınar, I.A. Altun, K. Onel, *J. Eur. Ceram. Soc.* 30 (2010) 2727–2734.
- [63] X. Liang, Y. Li, J. Liu, S. Sang, Y. Chen, B. Li, C.G. Aneziris, *Ceram. Int.* 42 (2016) 13091–13097.
- [64] R. Faure, F. Rossignol, T. Chartier, C. Bonhomme, A. Maître, G. Etchegoyen, P. Del Gallo, D. Gary, *J. Eur. Ceram. Soc.* 31 (2011) 303–312.
- [65] D. Loca, I. Narkevica, J. Ozolins, *Mater. Lett.* 159 (2015) 309–312.
- [66] M. Dressler, S. Reinsch, R. Schadrack, S. Benemann, *J. Eur. Ceram. Soc.* 29 (2009) 3333–3339.
- [67] M. Zahed, M. Shafiee Afarani, D. Mohebbi-Kalhari, *Appl. Phys. A Mater. Sci. Process.* (2015) 215–220.
- [68] A. Gomez-Martin, M.P. Orihuela, J.A. Becerra, J. Martinez-Fernandez, J. Ramirez-Rico, *Mater. Des.* 107 (2016) 450–460.
- [69] I. Narkevica, L. Stipnice, E. Jakobsons, I. Cakstina, J. Ozolins, *J. Eur. Ceram. Soc.* 37 (2016) 833–840.
- [70] A. Hadi, R. Emadi, S. Baghshahi, S.H. Naghavi, *Ceramics-Silikaty* 59 (2015) 90–95.
- [71] P. Balasubramanian, A. Grünwald, R. Detsch, A.R. Boccaccini, L. Hupa, B. Jokic, F. Tallia, A.K. Solanki, J.R. Jones, *Int. J. Appl. Glas. Sci.* 215 (2016) 206–215.
- [72] O.M. Goudouri, E. Theodosoglou, E. Kontonasaki, J. Will, K. Chrissafis, P. Koidis, K.M. Paraskevopoulos, A.R. Boccaccini, *Mater. Res. Bull.* 49 (2014) 399–404.
- [73] O.-M. Goudouri, C. Vogel, A. Grünwald, R. Detsch, E. Kontonasaki, A. R. Boccaccini, *J. Biomater. Appl.* 30 (2016) 740–749.
- [74] F. Çalişkan, A. Demir, Z. Tatli, *J. Porous Mater.* 20 (2013) 1501–1507.
- [75] F. Chen, Y. Yang, Q. Shen, L. Zhang, *Ceram. Int.* 38 (2012) 5223–5229.
- [76] J. Mesquita-Guimarães, M.A. Leite, J.C.M. Souza, B. Henriques, F.S. Silva, D. Hotza, A.R. Boccaccini, M.C. Fredel, *J. Biomed. Mater. Res. - Part A* (2016) 590–600.
- [77] U.F. Vogt, M. Gorbar, P. Dimopoulos-Eggenschwiler, A. Broenstrup, G. Wagner, P. Colombo, *J. Eur. Ceram. Soc.* 30 (2010) 3005–3011.
- [78] B. Ma, Y. Li, G. Liu, Z. Li, *Refract. Ind. Ceram.* 55 (2015) 573–580.
- [79] F. Scalera, F. Gervaso, K.P. Sanosh, A. Sannino, A. Licciulli, *Ceram. Int.* 39 (2013) 4839–4846.
- [80] L. Luo, X. Chen, Y. Wang, J. Yue, Z. Du, X. Huang, X.Z. Tang, *Ceram. Int.* 44 (2018) 12021–12029.
- [81] E. Boccardi, A. Philippart, V. Melli, L. Altomare, L. De Nardo, G. Novajra, C. Vitale-Brovarone, T. Fey, A.R. Boccaccini, *Ann. Biomed. Eng.* 44 (2016) 1881–1893.
- [82] C. Hoffmann, B. Reinhardt, D. Enke, S. Kaskel, *Microporous Mesoporous Mater.* 184 (2014) 1–6.
- [83] R. Dhimian, V. Petrunin, K. Rana, P. Morgen, *Ceram. Int.* 37 (2011) 3281–3289.
- [84] G. Amaral-Labat, C. Zollfrank, A. Ortona, S. Pusterla, A. Pizzi, V. Fierro, A. Celzard, *Ceram. Int.* 39 (2013) 1841–1851.
- [85] S.C. Santos, W. Acchar, C. Yamagata, S. Mello-Castanho, *J. Eur. Ceram. Soc.* 34 (2014) 2509–2517.
- [86] E. Boccardi, A. Philippart, J.A. Juhasz-Bortuzzo, G. Novajra, C. Vitale-Brovarone, A.R. Boccaccini, *Adv. Appl. Ceram.* 114 (2015) S56–S62.
- [87] K. Okada, T. Isoke, K. Katsumata, Y. Kameshima, A. Nakajima, K.J.D. MacKenzie, *Sci. Technol. Adv. Mater.* 12 (2011), 064701.
- [88] C. Voigt, C.G. Aneziris, J. Hubálková, *J. Am. Ceram. Soc.* 98 (2015) 1460–1463.
- [89] U.F. Vogt, L. Györfy, A. Herzog, T. Graule, G. Plesch, *J. Phys. Chem. Solids* 67 (2006) 1234–1238.
- [90] X. Liang, Y. Li, Q. Wang, S. Sang, Y. Xu, Y. Chen, B. Li, C.G. Aneziris, *Ceram. Int.* 43 (2017) 11197–11203.
- [91] X. Zhu, D. Jiang, S. Tan, *Mater. Sci. Eng. A* 323 (2002) 232–238.
- [92] X. Yao, Y. Yang, X. Liu, Z. Huang, *J. Eur. Ceram. Soc.* 33 (2013) 2909–2914.
- [93] S.L. McNamara, J. Rnjak-Kovacina, D.F. Schmidt, T.J. Lo, D.L. Kaplan, *Biomaterials* 35 (2014) 6941–6953.
- [94] A.B. Kousaalya, R. Kumar, B.T.N. Sridhar, *Ceram. Int.* 41 (2015) 1163–1170.
- [95] C. Petit, S. Meille, E. Maire, S. Tadier, J. Adrien, *J. Eur. Ceram. Soc.* 36 (2016) 3225–3233.
- [96] B. Yuan, G. Wang, H. Li, L. Liu, Y. Liu, Z. Shen, *Ceram. Int.* 42 (2016) 12613–12616.
- [97] L. Andersson, L. Bergström, *J. Eur. Ceram. Soc.* 28 (2008) 2815–2821.
- [98] L. Yin, X. Zhou, J. Yu, H. Wang, *Mater. Des.* 89 (2016) 620–625.
- [99] S. Sun, P. Wu, *ACS Appl. Mater. Interfaces* 5 (2013) 3481–3486.
- [100] N. Ordás, A. Bereciartu, C. García-Rosales, A. Morono, M. Malo, E.R. Hodgson, J. Abellá, S. Colominas, L. Sedano, *Fusion Eng. Des.* 89 (2014) 1274–1279.
- [101] T. Waschki, R. Oberacker, M.J. Hoffmann, *J. Am. Ceram. Soc.* 92 (2009) 79–84.
- [102] D.F. Souza, E.H.M. Nunes, D.S. Pimenta, D.C.L. Vasconcelos, J.F. Nascimento, W. Grava, M. Houmar, W.L. Vasconcelos, *Mater. Charact.* 96 (2014) 183–195.
- [103] H. Wang, I. Sung, X. Li, D. Kim, *J. Porous Mater.* 11 (2004) 265–271.
- [104] T. Konegger, L.F. Williams, R.K. Bordia, *J. Am. Ceram. Soc.* 98 (2015) 3047–3053.
- [105] L. Zhang, Z. Mao, J.D. Thomason, S. Wang, K. Huang, *J. Am. Ceram. Soc.* 95 (2012) 1832–1837.
- [106] Z. Živcová, E. Gregorová, W. Pabst, D.S. Smith, A. Michot, C. Poulhier, *J. Eur. Ceram. Soc.* 29 (2009) 347–353.
- [107] R. Stanculescu, C.E. Ciomaga, L. Padurariu, P. Galizia, N. Horchidan, C. Capiiani, C. Galassi, L. Mitoseriu, *J. Alloys. Compd.* 643 (2015) 79–87.
- [108] D.-H. Jang, Y.-W. Kim, H.-D. Kim, *J. Ceram. Soc. Japan* 115 (2007) 52–58.
- [109] A. Dey, N. Kayal, O. Chakrabarti, R.F. Caldato, C.M. André, M.D.M. Innocentini, *Ind. Eng. Chem. Res.* 52 (2013) 18362–18372.

- [110] S. Corradetti, L. Bisetto, M.D.M. Innocentini, S. Carturan, P. Colombo, A. Andrighetto, *Ceram. Int.* 42 (2016) 17764–17772.
- [111] L. Bisetto, M.D.M. Innocentini, W.S. Chacon, S. Corradetti, S. Carturan, P. Colombo, A. Andrighetto, *J. Nucl. Mater.* 440 (2013) 70–80.
- [112] G. Taillades, P. Batocchi, A. Essoumhi, M. Taillades, D.J. Jones, J. Rozire, *Microporous Mesoporous Mater.* 145 (2011) 26–31.
- [113] J.C. Han, Y.B. Sun, Y.M. Zhang, *Mater. Sci. Technol.* 26 (2010) 996–1000.
- [114] D. Jang, Y. Kim, I. Song, H. Kim, C.B. Park, *J. Ceram. Soc. Japan* 114 (2006) 549–553.
- [115] J. Eom, Y. Kim, K.J. Kim, *J. Ceram. Soc. Japan* 118 (2010) 102–106.
- [116] P. Wan, J. Wang, *J. Eur. Ceram. Soc.* 38 (2018) 463–467.
- [117] H. Wang, X. Li, F.C. Yu, D.P. Kim, *Sci. China, Ser. E Technol. Sci.* 49 (2006) 1–9.
- [118] Christian, M. Mitchell, D.P. Kim, P.J.A. Kenis, *J. Catal.* 241 (2006) 235–242.
- [119] J.H. Eom, Y.W. Kim, I.H. Song, H.D. Kim, *J. Eur. Ceram. Soc.* 28 (2008) 1029–1035.
- [120] Y.W. Kim, S.H. Kim, I.H. Song, H.D. Kim, C.B. Park, *J. Am. Ceram. Soc.* 88 (2005) 2949–2951.
- [121] H. Wang, X. Li, J. Yu, D. Kim, *J. Mater. Chem.* 14 (2004) 1383–1386.
- [122] V.G. Resmi, J.P. Deepa, V. Lakshmi, T.P.D. Rajan, C. Pavithran, B.C. Pai, *Int. J. Appl. Ceram. Technol.* 12 (2015) 967–975.
- [123] S.-H. Chae, Y.-W. Kim, I.-H. Song, H.-D. Kim, M. Narisawa, *J. Eur. Ceram. Soc.* 29 (2009) 2867–2872.
- [124] F. Wang, J. Yin, D. Yao, Y. Xia, K. Zuo, J. Xu, Y. Zeng, *Mater. Sci. Eng. A* 654 (2016) 292–297.
- [125] T. Konegger, T. Prochaska, R. Obmann, *J. Ceram. Soc. Japan* 124 (2016) 1030–1034.
- [126] H. Wang, S.Y. Zheng, X.D. Li, D.P. Kim, *Microporous Mesoporous Mater.* 80 (2005) 357–362.
- [127] L. Meng, X. Zhang, Y. Tang, K. Su, J. Kong, *Sci. Rep.* 5 (2015) 7910.
- [128] X. Yan, T.T. Tsotsis, M. Sahimi, *Microporous Mesoporous Mater.* 190 (2014) 267–274.
- [129] L. Hu, R. Benitez, S. Basu, I. Karaman, M. Radovic, *Acta Mater.* 60 (2012) 6266–6277.
- [130] Y. Dong, C.A. Wang, J. Zhou, Z. Hong, *J. Eur. Ceram. Soc.* 32 (2012) 2213–2218.
- [131] N.A. Badarulzaman, A. Hamidon, M.A.A.M. Nor, *AIP Conference Proceedings* 1660, 2015, 070106.
- [132] M. Kotani, K. Nishiyabu, S. Matsuzaki, S. Tanaka, *J. Ceram. Soc. Japan* 119 (2011) 563–569.
- [133] X. Yan, T.T. Tsotsis, M. Sahimi, *Microporous Mesoporous Mater.* 210 (2015) 77–85.
- [134] M. Naviroj, S.M. Miller, P. Colombo, K.T. Faber, *J. Eur. Ceram. Soc.* 35 (2015) 2225–2232.
- [135] S. Vijayan, R. Narasimman, K. Prabhakaran, *J. Eur. Ceram. Soc.* 34 (2014) 4347–4354.
- [136] M. Fukushima, Y.I. Yoshizawa, *J. Eur. Ceram. Soc.* 36 (2016) 2947–2953.
- [137] H. Yang, F. Ye, Q. Liu, S. Liu, Y. Gao, L. Liu, *Mater. Lett.* 138 (2015) 135–138.
- [138] E. Sani, E. Landi, D. Sciti, V. Medri, *Sol. Energy Mater. Sol. Cells* 144 (2016) 608–615.
- [139] Y. Zhang, M. Xie, J. Roscow, Y. Bao, K. Zhou, D. Zhang, C.R. Bowen, *J. Mater. Chem. A* 5 (2017) 6569–6580.
- [140] X. Liu, W. Xue, C. Shi, J. Sun, *Ceram. Int.* 41 (2015) 11922–11926.
- [141] Y. Zhang, K. Zhou, J. Zeng, D. Zhang, *Adv. Appl. Ceram.* 112 (2013) 405–411.
- [142] Y. Tang, S. Qiu, Q. Miao, C. Wu, *J. Eur. Ceram. Soc.* 36 (2016) 1233–1240.
- [143] A.A. Al-Attar, M. Asle Zaeem, S.A. Ajeel, N.E.A. Latiff, *J. Eur. Ceram. Soc.* 37 (2016) 1635–1642.
- [144] G. Liu, D. Zhang, C. Meggs, T.W. Button, *Scr. Mater.* 62 (2010) 466–468.
- [145] G. Liu, T.W. Button, D. Zhang, *J. Eur. Ceram. Soc.* 34 (2014) 4083–4088.
- [146] T. Xu, C.A. Wang, *J. Eur. Ceram. Soc.* 36 (2016) 2647–2652.
- [147] F. He, Y. Yang, J. Ye, *Ceram. Int.* 42 (2016) 14679–14684.
- [148] S. Sadeghpour, A. Amirjani, M. Hafezi, A. Zamanian, *Ceram. Int.* 40 (2014) 16107–16114.
- [149] B. Zhang, F. Ye, Q. Liu, H. Zhang, Y. Gao, C. Yang, *J. Mater. Sci. Mater. Electron.* 27 (2016) 11986–11994.
- [150] Y. Zhang, Y. Bao, D. Zhang, C.R. Bowen, *J. Am. Ceram. Soc.* 98 (2015) 2980–2983.
- [151] R. Zhang, D. Fang, Y. Pei, L. Zhou, *Ceram. Int.* 38 (2012) 4373–4377.
- [152] F. Wang, D. Yao, Y. Xia, K. Zuo, J. Xu, Y. Zeng, *Ceram. Int.* 42 (2015) 4526–4531.
- [153] C. Ferraro, E. Garcia-Tuñon, V.G. Rocha, S. Barg, M.D. Fariñas, T.E.G. Alvarez-Arenas, G. Sernicola, F. Giuliani, E. Saiz, *Adv. Funct. Mater.* 26 (2016) 1636–1645.
- [154] Y. Wu, J. Zhao, Y. Li, K. Lu, *Ceram. Int.* 42 (2016) 15597–15602.
- [155] R. Zhang, B. Han, D. Fang, Y. Wang, *Ceram. Int.* 41 (2015) 11517–11522.
- [156] R. Zhang, D. Fang, X. Chen, Y. Pei, Z. Wang, Y. Wang, *Mater. Des.* 46 (2013) 746–750.
- [157] R. Zhang, B. Han, D. Fang, *Ceram. Int.* 42 (2016) 6046–6053.
- [158] B. Han, R. Zhang, D. Fang, *J. Porous Mater.* 23 (2016) 563–568.
- [159] R. Chen, C.A. Wang, Y. Huang, L. Ma, W. Lin, *J. Am. Ceram. Soc.* 90 (2007) 3478–3484.
- [160] M. Fukushima, T. Fujiwara, T. Fey, K. Kakimoto, *J. Am. Ceram. Soc.* 100 (2017) 5400–5408.
- [161] T. Xu, C.A. Wang, *Mater. Des.* 91 (2016) 242–247.
- [162] R. Guo, C.A. Wang, A. Yang, *J. Am. Ceram. Soc.* 94 (2011) 1794–1799.
- [163] S. Dong, W. Zhu, X. Gao, Z. Wang, L. Wang, X. Wang, C. Gao, *Chem. Eng. J.* 295 (2016) 530–541.
- [164] S. Deville, *Adv. Eng. Mater.* 10 (2008) 155–169.
- [165] V. Naglieri, B. Gludovatz, A.P. Tomsia, R.O. Ritchie, *Acta Mater.* 98 (2015) 141–151.
- [166] C. Lauthillere, J.M. Serra, *Bol. La Soc. Esp. Ceram. y Vidr.* 55 (2016) 45–54.
- [167] A. Guidinger, D. Roussel, D. Jauffrès, C.L. Martin, R.K. Bordia, *J. Am. Ceram. Soc.* 99 (2016) 979–987.
- [168] G. Liu, T.W. Button, *Ceram. Int.* 39 (2013) 8507–8512.
- [169] M.S. Cilla, J. de Melo Cartaxo, R.R. Menezes, L.N. deLima Santana, G. de Araujo Neves, *Ceram. Int.* 42 (2015) 9278–9282.
- [170] A. Shaga, P. Shen, R.F. Guo, Q.C. Jiang, *Ceram. Int.* 42 (2015) 9653–9659.
- [171] S. Zavareh, A. Hilger, K. Hirslandt, O. Goerke, I. Manke, J. Banhart, A. Gurlor, *J. Ceram. Soc. Japan* 124 (2016) 1067–1071.
- [172] E. Munch, E. Saiz, A.P. Tomsia, S. Deville, *J. Am. Ceram. Soc.* 92 (2009) 1534–1539.
- [173] L.Y. Zhang, D.L. Zhou, Y. Chen, B. Liang, J.B. Zhou, *J. Eur. Ceram. Soc.* 34 (2014) 2443–2452.
- [174] A. Pokhrel, D.N. Seo, S.T. Lee, I.J. Kim, *J. Korean Ceram. Soc.* 50 (2013) 93–102.
- [175] A. Shimamura, M. Fukushima, M. Hotta, T. Ohji, N. Kondo, *J. Ceram. Soc. Japan* 2 (2017) 7–11.
- [176] S. Barg, C. Soltmann, M. Andrade, D. Koch, G. Grathwohl, *J. Am. Ceram. Soc.* 91 (2008) 2823–2829.
- [177] N. Sarkar, J.G. Park, S. Mazumder, A. Pokhrel, C.G. Aneziris, I.J. Kim, *Ceram. Int.* 41 (2015) 6306–6311.
- [178] R. Ahmad, J.H. Ha, I.H. Song, *J. Eur. Ceram. Soc.* 33 (2013) 2559–2564.
- [179] R. Ahmad, J.-H. Ha, I.-H. Song, *J. Ceram. Soc. Japan* 123 (2015) 383–388.
- [180] R. Ahmad, J.H. Ha, I.H. Song, *Mater. Lett.* 139 (2015) 252–254.
- [181] U.T. Gonzenbach, A.R. Studart, E. Tervoort, L.J. Gauckler, *Langmuir* 23 (2007) 1025–1032.
- [182] Y.W. Lo, W.C.J. Wei, C.H. Hsueh, *Mater. Chem. Phys.* 129 (2011) 326–330.
- [183] U.T. Gonzenbach, A.R. Studart, D. Steinlin, E. Tervoort, L.J. Gauckler, *J. Am. Ceram. Soc.* 90 (2007) 3407–3414.
- [184] V. Sciamanna, B. Nait-Ali, M. Gonon, *Ceram. Int.* 41 (2015) 2599–2606.
- [185] J.G. Park, A. Pokhrel, S.D. Nam, W. Zhao, S.M. Park, I.J. Kim, *J. Ceram. Process. Res.* 14 (2013) 508–512.
- [186] N. Sarkar, K.S. Lee, J.G. Park, S. Mazumder, C.G. Aneziris, I.J. Kim, *Ceram. Int.* 42 (2015) 3548–3555.
- [187] N. Sarkar, J.G. Park, S. Mazumder, C.G. Aneziris, I.J. Kim, *J. Eur. Ceram. Soc.* 35 (2015) 3969–3976.
- [188] D. Staedler, C. Scaletta, L.A. Applegate, H. Comas, L.J. Gauckler, S. Gerberlemaire, L. Juillerat-jeanneret, U.T. Gonzenbach, *Bioconjug. Chem.* 23 (2012) 2278–2290.
- [189] Y. Li, W. Cao, L. Gong, R. Zhang, X. Cheng, *Ceram. - Silikaty* 60 (2016) 91–98.
- [190] L. Han, F. Li, X. Deng, J. Wang, H. Zhang, S. Zhang, *J. Eur. Ceram. Soc.* 37 (2017) 2717–2725.
- [191] H. Guo, W. Li, F. Ye, *Ceram. Int.* 42 (2016) 17332–17338.
- [192] D.C. Jana, G. Sundararajan, K. Chattopadhyay, *J. Am. Ceram. Soc.* 100 (2017) 312–322.
- [193] B. Dong, B. Yuan, G. Wang, K. Chen, J. Han, H. Li, *J. Eur. Ceram. Soc.* 36 (2016) 3889–3893.
- [194] S. Bhaskar, G.H. Cho, J.G. Park, S.W. Kim, H.T. Kim, I.J. Kim, *J. Ceram. Soc. Japan* 123 (2015) 378–382.
- [195] A. Natoli, A. Cabeza, Á.G. De La Torre, M.A.G. Aranda, I. Santacruz, *J. Am. Ceram. Soc.* 95 (2012) 502–508.
- [196] Z. Wu, L. Sun, J. Wang, *Ceram. Int.* 42 (2016) 14894–14902.
- [197] Z. Wu, L. Sun, J. Wang, *J. Mater. Sci. Technol.* 31 (2015) 1237–1243.
- [198] R. Ahmad, J.H. Ha, I.H. Song, *J. Eur. Ceram. Soc.* 34 (2014) 1303–1310.
- [199] W.L. Huo, X.Y. Zhang, Y.G. Chen, Y.J. Lu, W.T. Liu, X.Q. Xi, Y.L. Wang, J. Xu, J. L. Yang, *J. Am. Ceram. Soc.* 99 (2016) 3512–3515.
- [200] S. Bhaskar, J.G. Park, K.S. Lee, S.Y. Kim, I.J. Kim, *Ceram. Int.* 42 (2016) 14395–14402.
- [201] V.R. Salvini, P.R.O. Lasso, A.P. Luz, V.C. Pandolfelli, *Int. J. Appl. Ceram. Technol.* 13 (2016) 522–531.
- [202] S. Barg, D. Koch, G. Grathwohl, *J. Am. Ceram. Soc.* 92 (2009) 2854–2860.
- [203] E. Soh, E. Kolos, A.J. Ruys, *Ceram. Int.* 41 (2015) 1031–1047.
- [204] J.P. Ball, B.A. Mound, J.C. Nino, J.B. Allen, *J. Biomed. Mater. Res. - Part A* 102 (2014) 2089–2095.
- [205] S. Vijayan, P. Wilson, R. Sreeja, K. Prabhakaran, *J. Am. Ceram. Soc.* 99 (2016) 3866–3873.
- [206] S. Vijayan, P. Wilson, R. Sreeja, K. Prabhakaran, *Mater. Lett.* 194 (2017) 126–129.
- [207] M. Zhu, R. Ji, Z. Li, H. Wang, L.L. Liu, Z. Zhang, *Constr. Build. Mater.* 112 (2016) 398–405.
- [208] F. Li, M. Liang, X.F. Ma, X. Huang, G.J. Zhang, *J. Porous Mater.* 22 (2015) 493–500.
- [209] F. Li, Z. Kang, X. Huang, X.G. Wang, G.J. Zhang, *J. Eur. Ceram. Soc.* 34 (2014) 3513–3520.
- [210] A. Butscher, M. Bohner, S. Hofmann, L. Gauckler, R. Müller, *Acta Biomater.* 7 (2011) 907–920.
- [211] S. Bose, S. Vahabzadeh, A. Bandyopadhyay, *Mater. Today* 16 (2013) 496–504.
- [212] R. Galante, C.G. Figueiredo-Pina, A.P. Serro, *Dent. Mater.* 35 (2019) 825–846.
- [213] E.C.E. Costa, J.P. Duarte, P. Bártolo, *Rapid Prototyp. J.* 23 (2017) 954–963.
- [214] J.Y. Lee, J. An, C.K. Chua, *Appl. Mater. Today* 7 (2017) 120–133.
- [215] N.A. Chartrain, C.B. Williams, A.R. Whittington, *Acta Biomater.* 74 (2018) 90–111.
- [216] G. Manogharan, M. Kioko, C. Linkous, *Jom* 67 (2015) 660–667.
- [217] J. Norman, R.D. Madurawe, C.M.V. Moore, M.A. Khan, A. Khairuzzaman, *Adv. Drug Deliv. Rev.* 108 (2017) 39–50.

- [218] S.L. Sing, W.Y. Yeong, F.E. Wiria, B.Y. Tay, Z. Zhao, L. Zhao, Z. Tian, S. Yang, *Rapid Prototyp. J.* 23 (2017) 611–623.
- [219] D. Klosterman, R. Chartoff, G. Graves, N. Osborne, B. Priore, *Compos. Part A Appl. Sci. Manuf.* 29 (1998) 1165–1174.
- [220] H. Dommatti, S.S. Ray, J.C. Wang, S.S. Chen, *RSC Adv.* 9 (2019) 16869–16883.
- [221] J.C. Wang, H. Dommatti, S.J. Hsieh, *Int. J. Adv. Manuf. Technol.* 103 (2019) 2627–2647.
- [222] M.J. Zafar, D. Zhu, Z. Zhang, *Materials* 12 (2019) 3361.
- [223] A. Kumar, S. Mandal, S. Barui, R. Vasireddi, U. Gbureck, M. Gelinsky, B. Basu, *Mater. Sci. Eng. R Rep.* 103 (2016) 1–39.
- [224] N. Travitzky, A. Bonet, B. Dermeik, T. Fey, I. Filbert-Demut, L. Schlier, T. Schlördt, P. Greil, *Adv. Eng. Mater.* 16 (2014) 729–754.
- [225] M.M. Methani, M. Revilla-León, A. Zandinejad, *J. Esthet. Restor. Dent.* 32 (2019) 182–192.
- [226] A. Kumar, A.R. Akkineni, B. Basu, M. Gelinsky, *J. Biomater. Appl.* 30 (2016) 1168–1181.
- [227] C. Polzin, D. Gunther, H. Seitz, *J. Ceram. Sci. Technol.* 6 (2015) 141–145.
- [228] T. Kumaresan, R. Gandhinathan, M. Ramu, M. Ananthasubramanian, K. B. Pradheepa, *J. Mech. Sci. Technol.* 30 (2016) 5305–5312.
- [229] K.C.R. Kolan, M.C. Leu, G.E. Hilmas, R.F. Brown, M. Velez, *Biofabrication* 3 (2011), 025004.
- [230] S. Tarafder, N.M. Davies, A. Bandyopadhyay, S. Bose, *Biomater. Sci.* 1 (2013) 1250.
- [231] A. Farzadi, M. Solati-Hashjin, M. Asadi-Eydivand, N.A.A. Osman, *PLoS One* 9 (2014) 1–14.
- [232] L. Podshivalov, C.M. Gomes, A. Zocca, J. Guenster, P. Bar-Yoseph, A. Fischer, *Procedia CIRP* 5 (2013) 247–252.
- [233] S.C. Cox, J.A. Thornby, G.J. Gibbons, M.A. Williams, K.K. Mallick, *Mater. Sci. Eng. C* 47 (2015) 237–247.
- [234] J.A. Choren, S.M. Heinrich, M.B. Silver-Thorn, *J. Mater. Sci.* 48 (2013) 5103–5112.
- [235] A. Kumar, K. Mohanta, D. Kumar, O. Parkash, *Microporous Mesoporous Mater.* 213 (2015) 48–58.
- [236] F. Han, Z. Zhong, Y. Yang, W. Wei, F. Zhang, W. Xing, Y. Fan, *J. Eur. Ceram. Soc.* 36 (2016) 3909–3917.
- [237] F. Han, Z. Zhong, F. Zhang, W. Xing, Y. Fan, *Ind. Eng. Chem. Res.* 54 (2015) 226–232.
- [238] I. Zake-Tiluga, V. Svinka, R. Svinka, L. Grase, *Ceram. Int.* 3 (2015) 1–6.
- [239] X. Jin, L. Dong, Q. Li, H. Tang, N. Li, Q. Qu, *Ceram. Int.* 42 (2016) 13309–13313.
- [240] M. Chen, H. Wang, H. Jin, X. Pan, Z. Jin, *Ceram. Int.* 42 (2016) 3130–3137.
- [241] S. Zhu, S. Ding, H. Xi, Q. Li, R. Wang, *Ceram. Int.* 33 (2007) 115–118.
- [242] J. She, T. Ohji, Z.-Y. Deng, *J. Am. Ceram. Soc.* 85 (2002) 2125–2127.
- [243] X. Lu, Y. Wei, H. Wang, J. Wen, J. Zhou, J. Fan, *J. Mater. Sci. Technol.* 30 (2014) 1217–1222.
- [244] J. Wu, G. Leng, X. Xu, K. Li, X. Lao, C. Zhou, *Sol. Energy Mater. Sol. Cells* 108 (2013) 9–16.
- [245] X. Xu, Z. Rao, J. Wu, Y. Zhou, D. He, Y. Liu, *J. Wuhan Univ. Technol. Mater. Sci. Ed.* 30 (2015) 27–32.
- [246] K.W. Schlichting, N.P. Pature, P.G. Klemens, *J. Mater. Sci.* 36 (2001) 3003–3010.
- [247] P. Wan, Z. Wu, H. Zhang, L. Gao, J. Wang, *Mater. Res. Lett.* 4 (2016) 104–111.
- [248] L. Hu, C.A. Wang, Y. Huang, *J. Mater. Sci.* 45 (2010) 3242–3246.
- [249] B. Nait-Ali, K. Haberkro, H. Vesteghem, J. Absi, D.S. Smith, *J. Eur. Ceram. Soc.* 26 (2006) 3567–3574.
- [250] X. Du, L. Zhao, X. He, X. Wang, W. Qu, H. Chen, H. Chen, J. Wang, Z. Lei, *J. Porous Mater.* 23 (2016) 381–388.
- [251] S. Gu, T.J. Lu, D.D. Hass, H.N.G. Wadley, *Acta Mater.* 49 (2001) 2539–2547.
- [252] X. Dong, M. Wang, A. Guo, Y. Zhang, S. Ren, G. Sui, H. Du, *J. Alloys. Compd.* 694 (2017) 1045–1053.
- [253] J. Bourret, A. Michot, N. Tessier-Doyen, B. Naït-Ali, F. Penneac, A. Alzina, J. Vicente, C.S. Peyratout, D.S. Smith, *J. Am. Ceram. Soc.* 97 (2014) 938–944.
- [254] L. Yuan, B. Ma, Q. Zhu, X. Zhang, H. Zhang, J. Yu, *Ceram. Int.* 43 (2017) 5478–5483.
- [255] S. Li, C.A. Wang, L. Hu, *J. Am. Ceram. Soc.* 96 (2013) 3223–3227.
- [256] M. Arai, H. Ochiai, T. Suidzu, *Surf. Coatings Technol.* 285 (2016) 120–127.
- [257] R. Zhang, S. Li, C. Ye, *J. Alloys. Compd.* 712 (2017) 445–450.
- [258] C.Q. Hong, J.C. Han, X.H. Zhang, J.C. Du, *Scr. Mater.* 68 (2013) 599–602.
- [259] Y. Wang, D. Su, H. Ji, X. Li, Z. Zhao, H. Tang, *J. Alloys. Compd.* 703 (2017) 437–447.
- [260] H.Q. Jin, X.L. Yao, L.W. Fan, X. Xu, Z.T. Yu, *Int. J. Heat Mass Transf.* 92 (2016) 589–602.
- [261] M.A. Bautista, J.Q. Cancapa, J.M. Fernandez, M.A. Rodríguez, M. Singh, *J. Eur. Ceram. Soc.* 31 (2011) 1325–1332.
- [262] Z. Zhong, W. Xing, X. Li, F. Zhang, *Ind. Eng. Chem. Res.* 52 (2013) 5455–5461.
- [263] Y. Suzuki, M. Morimoto, *J. Ceram. Soc. Japan* 118 (2010) 1212–1216.
- [264] R.A. Vasques, M.D.M. Innocentini, O.B.G. Assis, *Rev. Fisica. Apl. E. Instrumenta. Cao.* 14 (1999) 120.
- [265] H.J. Choi, J.U. Kim, H.S. Kim, S.H. Kim, M.H. Lee, *Ceram. Int.* 41 (2015) 10030–10037.
- [266] B.A. Latella, L. Henkel, E.G. Mehrrens, *J. Mater. Sci.* 41 (2006) 423–430.
- [267] S. Heidenreich, *Fuel* 104 (2013) 83–94.
- [268] J. Luyten, S. Mullens, I. Thijs, *Synthesis (Stuttg.)* 28 (2010) 131–142.
- [269] M.J. Dejneka, C.L. Chapman, S.T. Mixture, *J. Am. Ceram. Soc.* 94 (2011) 2249–2261.
- [270] M.P. Orihuela, A. Gómez-Martín, J.A. Becerra, R. Chacartegui, J. Ramírez-Rico, *J. Environ. Manage.* 203 (2017) 907–919.
- [271] J.K. Park, J.H. Park, J.W. Park, H.S. Kim, Y.I. Jeong, *Sep. Purif. Technol.* 55 (2007) 321–326.
- [272] J.J. Simonis, A.K. Basson, *Phys. Chem. Earth* 36 (2011) 1129–1134.
- [273] Y. Lv, H. Liu, Z. Wang, S. Liu, L. Hao, Y. Sang, D. Liu, J. Wang, R.I. Boughton, *J. Memb. Sci.* 331 (2009) 50–56.
- [274] K. Nunnelle, J.A. Smith, M.Y. Smith, A. Samie, *World Environmental and Water Resources Congress 2016*, 2016, pp. 292–298.
- [275] L.S. Abebe, Y.H. Su, R.L. Guerrant, N.S. Swami, J.A. Smith, *Environ. Sci. Technol.* 49 (2015) 12958–12967.
- [276] D. Ren, J.A. Smith, *Environ. Sci. Technol.* 47 (2013) 3825–3832.
- [277] A.M. Mittelman, D.S. Lantagne, J. Rayner, K.D. Pennell, *Environ. Sci. Technol.* 49 (2015) 8515–8522.
- [278] H. Zhang, V. Oyanedel-Craver, *J. Hazard. Mater.* 260 (2013) 272–277.
- [279] L.S. Abebe, X. Chen, M.D. Sobsey, *Int. J. Environ. Res. Public Health* 13 (2016) 269.
- [280] F. Patel, M.A. Baig, T. Laoui, *Desalin. Water Treat.* 35 (2011) 33–38.
- [281] Y. Zhang, F. He, S. Xia, L. Kong, D. Xu, Z. Wu, *Ecol. Eng.* 64 (2014) 186–192.
- [282] Y. Zhang, F. He, S. Xia, Q. Zhou, Z. Wu, *Environ. Pollut.* 206 (2015) 705–711.
- [283] M. Zhang, C. Yuan, Y. Yan, W. Shi, Y. Zhu, in: 2015 International Conference on Materials, Environmental and Biological Engineering, Atlantis Press, 2015.
- [284] E.F. Krivoshapkina, A.A. Vedyagin, P.V. Krivoshapkin, I.V. Desyatkyh, *Pet. Chem.* 55 (2015) 901–908.
- [285] W. Wan, J. Yang, Y. Feng, T. Qiu, *Mater. Lett.* 160 (2015) 120–123.
- [286] L. Du, W. Liu, S. Hu, Y. Wang, J. Yang, *J. Eur. Ceram. Soc.* 34 (2014) 731–738.
- [287] E. Vanhaecke, S. Ivanova, A. Deneuve, O. Ersen, D. Edouard, G. Winé, P. Nguyen, C. Pham, C. Pham-Huu, *J. Mater. Chem.* 18 (2008) 4654.
- [288] Z. Fu, J. Xie, F. He, D. Fang, *Russ. J. Appl. Chem.* 87 (2014) 1749–1754.
- [289] M. Klotz, I. Amirouche, C. Guizard, C. Viazzi, S. Deville, *Adv. Eng. Mater.* 14 (2012) 1123–1127.
- [290] F.C. Patcas, G.I. Garrido, B. Kraushaar-Czarnetzki, *Chem. Eng. Sci.* 62 (2007) 3984–3990.
- [291] J. Van Noyen, A. De Wilde, M. Schroeven, S. Mullens, J. Luyten, *Int. J. Appl. Ceram. Technol.* 9 (2012) 902–910.
- [292] N.M.D. Vitorino, A.V. Kovalevsky, M.C. Ferro, J.C.C. Abrantes, J.R. Frade, *Mater. Des.* 117 (2017) 332–337.
- [293] G. Plesch, M. Gorbár, U.F. Vogt, K. Jesenák, M. Vargová, *Mater. Lett.* 63 (2009) 461–463.
- [294] Y. Kim, C. Kim, J. Yi, *Mater. Res. Bull.* 39 (2004) 2103–2112.
- [295] C. Han, Y. Wang, Y. Lei, B. Wang, *Ceram. Int.* 42 (2016) 5368–5374.
- [296] M. Vargová, G. Plesch, U.F. Vogt, M. Zahoran, M. Gorbár, K. Jesenák, *Appl. Surf. Sci.* 257 (2011) 4678–4684.
- [297] T. Kim, *Int. J. Hydrogen Energy* 34 (2009) 6790–6798.
- [298] C. Hoffmann, P. Plate, A. Steinbrück, S. Kaskel, *Catal. Sci. Technol.* 5 (2015) 4174–4183.
- [299] B. Fumeys, S. Stoller, R. Fricker, R. Weber, V. Dorer, U.F. Vogt, *Int. J. Hydrogen Energy* 41 (2016) 7494–7499.
- [300] Y. Zhu, S. Chen, X. Quan, Y. Zhang, C. Gao, Y. Feng, *J. Memb. Sci.* 431 (2013) 197–204.
- [301] H.C. Aran, J.K. Chinthaginjala, R. Groote, T. Roelofs, L. Lefferts, M. Wessling, R.G. H. Lammertink, *Chem. Eng. J.* 169 (2011) 239–246.
- [302] X. Chen, S.S. Mao, *Chem. Rev.* 107 (2007) 2891–2959.
- [303] P. Nguyen, C. Pham, *Appl. Catal. A Gen.* 391 (2011) 443–454.
- [304] I.K. Sung, Christian, M. Mitchell, D.P. Kim, P.J.A. Kenis, *Adv. Funct. Mater.* 15 (2005) 1336–1342.
- [305] Y. Peng, J.T. Richardson, *Appl. Catal. A Gen.* 266 (2004) 235–244.
- [306] N. Hatz, *AIP Conference Proceedings*, 1453, 2012, pp. 57–62.
- [307] F. Zaversky, L. Aldaz, M. Sánchez, A.L. Ávila-Marín, M.I. Roldán, J. Fernández-Reche, A. Füssel, W. Beckert, J. Adler, *Appl. Energy* 210 (2018) 351–375.
- [308] Z. Wu, C. Caliot, G. Flamant, Z. Wang, *Sol. Energy* 85 (2011) 2374–2385.
- [309] O. Smirnova, T. Fend, R. Capuano, G. Feckler, P. Schwarzbözl, F. Sutter, *Sol. Energy Mater. Sol. Cells* 176 (2018) 196–203.
- [310] Q. Li, Z. Wang, F. Bai, S. Chu, B. Yang, *AIP Conf. Proc.*, 1850, 2017, 160016.
- [311] F. Bai, *Int. J. Therm. Sci.* 49 (2010) 2400–2404.
- [312] A. Kribus, Y. Gray, M. Grijnevich, G. Mittelman, S. Mey-Cloutier, C. Caliot, *Sol. Energy* 110 (2014) 463–481.
- [313] P. Furler, J. Scheffe, M. Gorbár, L. Moes, U. Vogt, A. Steinfeld, *Energy Fuels* 26 (2012) 7051–7059.
- [314] P. Furler, A. Steinfeld, *Chem. Eng. Sci.* 137 (2015) 373–383.
- [315] C. Agrafiotis, L. De Oliveira, M. Roeb, C. Sattler, *AIP Conf. Proc.*, 1734, 2016, 050001.
- [316] C. Agrafiotis, M. Roeb, C. Sattler, *Energy Procedia* 69 (2015) 706–715.
- [317] Q. Yin, B. Zhu, H. Zeng, *Microstructure, Property and Processing of Functional Ceramics*, Springer Science & Business Media, 2009.
- [318] K. Bae, D.Y. Jang, H.J. Choi, D. Kim, J. Hong, B.-K. Kim, J.-H. Lee, J.-W. Son, J. H. Shim, *Nat. Commun.* 8 (2017) 14553.
- [319] J.J. Haslam, A.Q. Pham, B.W. Chung, J.F. DiCarlo, R.S. Glass, *J. Am. Ceram. Soc.* 88 (2005) 513–518.
- [320] R. Liu, T. Xu, C. Wang, *Ceram. Int.* 42 (2015) 2907–2925.
- [321] K. Schneider, R.J. Thorne, P.J. Cameron, *Philos. Trans. A* 374 (2016), 20150080.
- [322] Z. Tu, M.J. Zachman, S. Choudhury, S. Wei, L. Ma, Y. Yang, L.F. Kourkoutsis, L. A. Archer, *Adv. Energy Mater.* 7 (2017), 1602367.
- [323] J. Roscow, Y. Zhang, J. Taylor, C.R. Bowen, *Eur. Phys. J. Spec. Top.* 224 (2015) 2949–2966.
- [324] J.I. Roscow, J. Taylor, C.R. Bowen, *Ferroelectrics* 498 (2016) 40–46.
- [325] J.I. Roscow, R.W.C. Lewis, J. Taylor, C.R. Bowen, *Acta Mater.* 128 (2017) 207–217.

- [326] Y. Zhang, J. Roscow, R. Lewis, H. Khanbareh, V.Y. Topolov, M. Xie, C.R. Bowen, *Acta Mater.* 154 (2018) 100–112.
- [327] G. Martínez-Ayuso, M.I. Friswell, H. Haddad Khodaparast, J.I. Roscow, C. R. Bowen, *Acta Mater.* 173 (2019) 332–341.
- [328] J.I. Roscow, Y. Zhang, M.J. Krašny, R.W.C. Lewis, J. Taylor, C.R. Bowen, *J. Phys. D Appl. Phys.* 51 (2018), 225301.
- [329] G. Martínez-Ayuso, M.I. Friswell, S. Adhikari, H.H. Khodaparast, C. A. Featherston, in: 27th International Conference on Noise and Vibration Engineering, Leuven, 2016.
- [330] A.K. Vashishth, V. Gupta, *Smart Mater. Struct.* 21 (2012), 125002.
- [331] J.I. Roscow, H. Pearce, H. Khanbareh, S. Kar-Narayan, C.R. Bowen, *Eur. Phys. J. Spec. Top.* 228 (2019) 1537–1554.
- [332] A.N. Rybyanets, A.A. Naumenko, M.A. Lugovaya, N.A. Shvetsova, *Ferroelectrics* 484 (2015) 95–100.
- [333] J.I. Roscow, V.Y. Topolov, J.T. Taylor, C.R. Bowen, *Smart Mater. Struct.* 26 (2017), 105006.
- [334] K.S. Srikanth, V.P. Singh, R. Vaish, *Int. J. Appl. Ceram. Technol.* 15 (2018) 140–147.
- [335] E. Ringgaard, F. Lautzenhiser, L.M. Bierregaard, T. Zawada, E. Molz, *Materials (Basel)*. 8 (2015) 8877–8889.
- [336] E.F. da Costa, N.E. de Oliveira, F.J.O. Morais, P. Carvalhaes-Dias, L.F.C. Duarte, A. Cabot, J.A.S. Dias, *Sensors (Switzerland)* 17 (2017) 1–16.
- [337] T.A. Blank, L.P. Eksperiandova, K.N. Belikov, *Sensors Actuators, B Chem.* 228 (2016) 416–442.
- [338] X. Yin, L. Kong, L. Zhang, L. Cheng, N. Travitzky, P. Greil, *Int. Mater. Rev.* 59 (2014) 326–355.
- [339] R. Wu, K. Zhou, C.Y. Yue, J. Wei, Y. Pan, *Prog. Mater. Sci.* 72 (2015) 1–60.
- [340] H. Zhou, J. Zhuang, Q. Yan, Q. Liu, *Mater. Lett.* 85 (2012) 117–119.
- [341] Y. Cheng, M. Tan, P. Hu, X. Zhang, B. Sun, L. Yan, S. Zhou, W. Han, *Appl. Surf. Sci.* 448 (2018) 138–144.
- [342] K. Yang, H. Mei, D. Han, L. Cheng, *Ceram. Int.* 44 (2018) 20187–20191.
- [343] J. Kuang, X. Hou, T. Xiao, Y. Li, Q. Wang, P. Jiang, W. Cao, *Ceram. Int.* 45 (2018) 6263–6267.
- [344] F.-Z. Zhang, T. Kato, M. Fujii, M. Takahashi, *J. Eur. Ceram. Soc.* 26 (2006) 667–671.
- [345] M. Carlesso, R. Giacomelli, T. Krause, A. Molotnikov, D. Koch, S. Kroll, K. Tushtev, Y. Estrin, K. Rezwani, *J. Eur. Ceram. Soc.* 33 (2013) 2549–2558.
- [346] M. Carlesso, R. Giacomelli, S. Günther, D. Koch, S. Kroll, S. Odenbach, K. Rezwani, *J. Am. Ceram. Soc.* 96 (2013) 710–718.



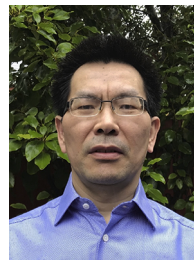
Yu Chen is a PhD student in Materials Engineering under the supervision of Professor Yanqiu Zhu at University of Exeter. He received B.Eng. (2015) in Functional Materials from Huazhong University of Science and Technology (HUST) and M.Sc. (2016) in Advanced Engineering Materials from the University of Manchester. His research focuses on porous SiC nanowire structure for thermal insulation, catalyst support, and electro-mechanical strain sensor applications.



Dr. Nannan Wang received his PhD from University of Exeter in Advanced Functional Materials in 2018. He had about one-year postdoctoral experience for a Joint-Supervision project between Guangxi and Tsinghua University. He now works at the University of Guangxi as an Assistant Professor at the School of Resource, Environment and Materials. His main researches cover experimental synthesis and characterization of materials for energy generation and storage applications.



Dr. Oluwafunmilola Ola is a Leverhulme Early Career and Nottingham Research Fellow at The University of Nottingham. She received her PhD degree in Chemical Engineering from Heriot-Watt University in 2014, for which she was awarded the RSC Energy Sector PhD Thesis Prize. Her research interests span the fundamentals and applications of functionalised porous nanocomposites for gas sensing, energy conversion and storage.



Dr. Yongde Xia earned his PhD from Fudan University in 1999. After two years of postdoctoral research at Korea Advanced Institute of Science and Technology and another two years at the University of Paris-Sud of France, he then worked as a Research Fellow at The University of Nottingham. He took on a Lecturer post in 2010, and is currently a Senior Lecturer in Functional Materials at the College of Engineering, Mathematics and Physics Sciences at University of Exeter. His research interests include the synthesis, characterisation and applications of various novel porous materials in energy storage and conversion.



Prof. Yanqiu Zhu, RSIF, FRSC, FIMMM, received his PhD title from Tsinghua University in 1996 and following a short spell at NIMS (Tsukuba) as a COE Fellow, he then joined the Sussex Fullerene Centre at the University of Sussex, with the support of the Royal Society. After about 7 years at Sussex as a Research Fellow, he moved to The University of Nottingham in 2003, as an EPSRC Advanced Research Fellow and then became a Reader in Nanomaterials in 2008. Since 2010, he has been a Chair of Functional Materials at the University of Exeter, heading the Functional Materials Laboratory, working on a wide range of nanomaterials.